UTS UNIVERSITY OF TECHNOLOGY SYDNEY

Investigation of Smouldering Wildfires: Combustion Thresholds, Particle Emissions, and Public Health Impacts

by Yunzhu Qin

Thesis submitted in fulfilment of the requirements for the degree of

Doctor of Philosophy

under the supervision of Dr Yuhan Huang

Dr Xinyan Huang

Prof John Zhou

University of Technology Sydney

Faculty of Engineering and Information Technology

August 2025

Certificate of Original Authorship

I, Yunzhu Qin, declare that this thesis is submitted in fulfilment of the requirements for the award of Doctor of Philosophy, in the School of Civil and Environmental Engineering/Faculty of Engineering and Information Technology at the University of Technology Sydney.

This thesis is wholly my own work unless otherwise referenced or acknowledged. In addition, I certify that all information sources and literature used are indicated in the thesis.

I certify that the work in this thesis has not previously been submitted for a degree nor has it been submitted as part of the requirements for a degree at any other academic institution except as fully acknowledged within the text. This thesis is the result of a Collaborative Doctoral Research Degree program with the Hong Kong Polytechnic University.

This research is supported by the Australian Government Research Training Program.

Signature: Production Note:
Signature removed prior to publication.

Date: 13/8/2025

Acknowledgements

It has been a wonderful journey during my PhD study. I am deeply thankful to my mentors, friends, and family for all the support, encouragement, and inspiration they have provided me during this period.

First, I want to express my heartfelt gratitude to my principal supervisor at UTS, Dr Yuhan Huang. Your insightful advice and constructive feedback have been invaluable in refining my research, and your encouragement has given me the confidence to push forward through challenges. I truly appreciate your mentorship and the opportunities you have provided me throughout this journey.

I am equally grateful to my supervisor at HK PolyU, Dr Xinyan Huang, for your invaluable mentorship, unwavering support, and constant encouragement throughout my PhD study. Learning from your expertise has been a privilege.

I want to thank the mentors during these years: Dr. Mohd Zahirasri Mohd Tohir (UPM), Dr. Dejian Wu (Umicore), Dr. Zeyang Song (Xi'an University of Science and Technology), Dr. Jian Gao (Shenzhen Technology University). Thank you for helping me grow, I will always learn from each of you.

For this thesis, thank you all the co-authors, Dr. Shaorun Lin (Chapter 4, 5, 6, assistance in experiments and formal analysis), Dr. Dayang Nur Musa (Chapter 4, assistance in experiments), Dr. Yuying Chen (Chapter 5, 6, assistance in formal analysis), and Mr. Yichao Zhang (Chapter 6, assistance in experiments), Miss Siyan Wang and Dr. Michael Gollner (Chapter 7, assistance in modelling). I wish to thank Dr. Wei Wei (UTS) and Dr. Qiang Fu (UTS) for reviewing my work and assessing my candidature at UTS.

I am grateful to my friends who inspired me: Lehan, Qingyun, Chao, Yihao, Jingping, Jibin (UTS), Shaorun, Tao, and Shiyu (PolyU), Xiuqi (WPI), Cong Gao and Aoran (HKU), Enzo (CityU), Wenyuan (UNSW), Weidong (USTC), Siyan (UC Berkeley), Peng Zhao (Otto von Guericke University Magdeburg), Iffah and Michael (UPM), Dayang (UMS), Picha (Tokyo University of Science), Afi (Imperial College) for the beautiful memories in Hong Kong, Sydney, Canberra, Kuala Lumpur, Milan, Magdeburg, and

Coimbra. I would like to express my special thanks to my old friends, Xiongtian, Shijie, Sicheng, and Tengxiang for your time and encouragement.

I want to acknowledge the financial support from National Natural Science Foundation of China (NSFC Grant No. 52322610 and 51876183), General Research Fund Scheme of Hong Kong Research Grants Council (RGC-GRF Grant No. 15221523), and Inner Mongolia Science and Technology Department (No. 2021CG0002), as well as scholarships from University of Technology Sydney and The Hong Kong Polytechnic University.

Finally, and most importantly, a BIG thank you to my family for your love, patience, and unconditional support. I could not have accomplished this without your constant belief in me. Thank you to my sister for always being a guiding light in my life. Lastly, my heartfelt gratitude goes to my beloved partner, Qing Yu. I deeply appreciate our shared efforts and mutual support during these years, which have made the entire journey feel passionate and hopeful.

Yunzhu Qin

Sydney, Australia

August 2025

List of Publications

Publications included in this thesis

1. **Y. Qin**, D. Musa, S. Lin* and X. Huang* (2022). Deep Peat Fire Persistently Smouldering for Weeks: A Laboratory Demonstration. ***International Journal of Wildland Fire***, 32, 86-98. (Chapter 4)
2. **Y. Qin**, Y. Chen, S. Lin* and X. Huang* (2022). Limiting Oxygen Concentration and Supply Rate of Smouldering Propagation. ***Combustion and Flame***, 245, 112380. (Chapter 5)
3. **Y. Qin**, Y. Chen, Y. Zhang, S. Lin* and X. Huang* (2024). Modeling Smothering Limit of Smouldering Combustion: Oxygen Supply, Fuel Density, and Moisture Content. ***Combustion and Flame***, 269, 113683. (Chapter 6)
4. **Y. Qin**, Y. Huang*, X. Huang*. Global Wildland fire Emissions and Health Impacts. *Ready for submission* (Chapter 2)
5. S. Wang[#], **Y. Qin**[#], Y. Huang, X. Huang, M. Gollner*. Machine Learning-based Prediction of Wildland-urban Interface Fire Emissions. *Under preparation* (Chapter 7)
6. **Y. Qin**, Y. Huang*, X. Huang*. Estimating Public Health Impact from 2014-2015 South-east Asia Smouldering Wildfires. *Under preparation* (Chapter 8)

Other publications during candidature

1. **Y. Qin**[#], Y. Zhang[#], Y. Chen, S. Lin*, Y. Shu*, Y. Huang, X. Huang* and M. Zhou (2025). Impact of Snow on Underground Smouldering Wildfire in Arctic-Boreal Peatlands. ***Environmental Science & Technology***, 59, 8, 3915-3924. (***selected as the supplemental journal cover***)
2. **Y. Qin**, Y. Zhang, Y. Chen, S. Lin* and X. Huang* (2024). Minimum oxygen supply rate for smouldering propagation: Effect of fuel bulk density and particle size. ***Combustion and Flame***, 261, 113292.
3. Y. Zhang, Y. Shu, **Y. Qin**, Y. Chen, S. Lin*, X. Huang*, M. Zhou (2024). Resurfacing of underground peat fire: smouldering transition to flaming wildfire on litter surface. ***International Journal of Wildland Fire***. 33(2).

4. S. Lin, **Y. Qin**, X. Huang* and M. Gollner (2023). Use of pre-charred surfaces to improve fire performance of wood. ***Fire Safety Journal***, 136, 103745.
5. Y. Chen, S. Lin, **Y. Qin**, N.C. Surawski* and X. Huang* (2023). Carbon distribution and multi-criteria decision analysis of flexible waste biomass smouldering processing technologies. ***Waste Management***, 167. 183-193.
6. Y. Chen, Z. Wang*, S. Lin, **Y. Qin** and X. Huang* (2023) A review on biomass thermal-oxidative decomposition data and machine learning prediction of thermal analysis. ***Cleaner Materials***, 100206.

[#] *indicates equal contribution; * indicates corresponding author.*

Table of Contents

List of Tables

List of Figures

Nomenclature

Symbols

A	condensed phase species A (reactant)
B	condensed phase species B (product)
c	specific heat capacity (J/kg·K)
D	diffusivity (m^2/s) /pore size (m)
d_p	characteristic pore size (m)
E	activation energy (J)
F	fuel (-)
ΔH	heat of reaction (MJ/kg)
h	specific enthalpy (J/kg)
h_c	convective coefficient ($W/m^2 \cdot K$)
h_r	radiative coefficient ($W/m^2 \cdot K$)
K	permeability (m^2)
k	thermal conductivity (W/m·K)
L	fuel length (-)
M	molar mass (g/mol)
m	mass (g)
$\dot{m}''$	mass flux ($g/m^2 \cdot s$)
Nu	Nusselt number (-)
n_k	reaction order (-)
p	pressure (Pa)
$\dot{q}''$	heat flux (kW/m^2)
S	spread/surface area (m^2)

T	temperature (^{o}C)
t	time (s)
U	flow velocity (mm/s)
X	volume fraction (-)
Y	mass fraction (-)
Z	pre-exponential factor (s^{-1})
ΔZ	cell size (m)

Greeks

α	thermal diffusivity (m^2/s)
β	local fire spread probability
γ	radiative conductivity coefficient (m)
ε	emissivity (-)
μ	local fire extinction probability
v	viscosity/stochiometric factor (Pa·s/-)
ρ	density (kg/m^3)
σ	Stefan–Boltzmann constant ($kg/s^3 \cdot K^4$)
ψ	porosity (-)
$\dot{\omega}''$	volumetric reaction rate ($kg/m^3 \cdot s$)

Subscripts

cond	conduction
conv	convection
cp	cellulose pyrolysis
d	destruction

dr	drying process
e	environmental
ev	evaporation
f	formation
g	gas
hp	hemicellulose pyrolysis
i	species number
k	reaction number
min	minimum
lp	lignin pyrolysis
o	original/bulk
O_2	oxygen
ox	oxidation or oxidizer
r	radiation
s	solid
sm	smouldering
lp	lignin pyrolysis
∞	ambient

Abbreviations

AI	Artificial Intelligence
ANN	Artificial Neural Network
AUST	Australia and New Zealand
BC	Black Carbon
BOAS	Boreal Asia

BONA	Boreal North America
CA	Cellular Automata
CEAM	Central America
CEAS	Central Asia
COD	Cause of Death
COPD	Chronic obstructive pulmonary disease
CRF	Concentration-response Functions
CTM	Chemical Transport Model
DSC	Differential Scanning Calorimetry
EA	Elementary Analysis
EC	Elemental Carbon
ECMWF	European Centre for Medium-Range Weather Forecasts
EF	Emission Factors
EQAS	Equatorial Asia
ER	Excess Risk
EURO	Europe
ESR	Electron Spin Resonance
FiTCH	Global fire emission dataset using the three-corner hat method
FPA	Fire Propagation Apparatus
FRP	Fire Radiative Power
FTIR	Fourier-transform Infrared Spectroscopy
FWI	Fire Weather Index
GBD	Global Burden of Disease
GEMM	Global Exposure Mortality Model
GEOS-Chem	Goddard Earth Observing System - Chemistry

GFAS	Global Fire Assimilation System
GFED	Global Fire Emission Database
GHG	Greenhouse Gases
Gpyro	Generalized pyrolysis model for combustible solids
IHD	Ischemic heart disease
LiDAR	Light Detection and Ranging
LOC	Limiting oxygen concentration
LRI	Lower respiratory infections
MC	Moisture content
MCE	Modified Combustion Efficiency
MERRA	Modern-Era Retrospective analysis for Research and Applications
ML	Machine learning
MOC	Minimum oxygen concentration
MODIS	Moderate Resolution Imaging Spectroradiometer
OC	Organic Carbon / Organic Content
PAH	Polycyclic Aromatic Hydrocarbons
PM	Particulate matter
PMMA	Polymethyl methacrylate
RMSE	Root Mean Square Error
RR	Relative Risk
SEAS	Southeast Asia
SHAF	Southern Hemisphere Africa
SHSA	Southern Hemisphere South America
TC	Thermocouple
THC	Total Hydrocarbon

TENA	Temperate North America
TGA	Thermogravimetric analysis
TPM	Total Particulate Matter
VOC	Volatile Organic Compound
WUI	Wildland-urban-interface

Abstract

Smouldering is a slow, low-temperature, and flameless form of combustion, which is governed by the competition between system heat losses and oxygen supply. Wide-spreading and long-lasting smouldering wildfires in natural fuels are one of the largest and most persistent combustion phenomena on Earth. However, our understanding of the smouldering combustion mechanism, oxygen thresholds, emissions and associated public health impacts are still limited. This thesis presents a comprehensive multi-scale study on smouldering wildfires to address these knowledge gaps. First, experimental and numerical studies were performed to explore near-limit oxygen thresholds for smouldering combustion. Results revealed that smouldering can sustain at extremely low oxygen condition of 2%. Second, machine learning models were deployed to predict emission factors of CO, CO_2, and particulate matters of typical natural fuels. Third, fire-associated premature deaths were assessed by using burned area dataset, GEOS-Chem chemical transport model, and Global Exposure Mortality Model. The analysis suggests that approximately 200,000 premature deaths were attributable to fire smoke exposure during the 2014–2015 peat fires in Southeast Asia. In summary, the insights gained from this thesis deepen our fundamental understanding of smouldering combustion and highlight the significant health and environmental impacts of smouldering wildfires.

Keywords: Fire limits; Lab experiment; Machine learning; Atmospheric transport modelling; Health impacts.

CHAPTER 1 Introduction

1.1 Research background

From the perspective of combustion, wildfires can be divided into two types: flaming and smouldering (Rein and Huang 2021). Smouldering is a slow, low-temperature, and flameless phenomenon that occurs in charring porous fuels such as peat, coal, wood, and forest litter. It is primarily sustained by exothermic oxidations when oxygen molecules directly attack the hot surface of condensed-phase reactive media. As a typical incomplete combustion, its reaction temperature (~450–700 °C), fire spread rate (~1 mm/min), and combustion heat (~6–15 MJ/kg) are lower than those of flaming combustion that occurs in gas phase. The smouldering process involves complex chemical reactions and intricate heat and mass transfer mechanisms. To summarize these processes, smouldering is often simplified into two steps: pyrolysis and char oxidation, as shown in **Fig. 1-1a**.

Pyrolysis is a prerequisite for the occurrence of smouldering reactions:

$$\text{Solid fuel} + \text{Heat} \rightarrow \text{Pyrolysis gases} + \text{Char} \tag{1.1}$$

In this process, charring solid fuels undergo endothermic decomposition (even in the absence of oxygen), producing pyrolysis gases, particulate matter (PM), and char. The pyrolysis temperature is influenced by fuel properties. Thermogravimetric analysis (TGA) shows that the lowest pyrolysis temperature (the threshold temperature at which pyrolysis reactions begin) of common fuels (such as wood products and peat) is about 200 °C, while the peak pyrolysis temperature (the threshold temperature causing the maximum rate of mass loss) is about 320 °C (Chen et al. 2023c).

The products of pyrolysis in both gas (pyrolysis gases) and solid (char) phases can undergo further oxidation. Flaming occurs when the exothermic reactions are dominated by homogeneous reactions between pyrolysis gases and oxygen:

$$\text{Pyrolysis gases} + \text{Oxygen} \rightarrow \text{Gaseous products} + \text{Heat} \quad \text{(Flaming)} \tag{1.2a}$$

The occurrence of flaming requires sufficient concentrations of pyrolysis gases and oxygen, as well as adequate heat and temperature to initiate flaming combustion (Quintiere 2016). By contrast, smouldering occurs when the oxidation of solid-phase char dominates the process:

$$\text{Char} + \text{Oxygen} \rightarrow \text{Gaseous products} + \text{Ash} + \text{Heat} \quad \text{(Smouldering)} \qquad (1.2b)$$

The characteristic temperatures of char oxidation are slightly higher than those of pyrolysis. The lowest oxidation temperature (the threshold temperature at which oxidation reactions begin) is about 300–350 °C, and the peak oxidation temperature (the threshold temperature causing the maximum rate of mass loss due to char oxidation) is about 440 °C (Chen et al. 2023c). Notably, metal and minerals contained in the char can catalyse oxidation reactions (Rein et al. 2016), and the inorganic contents (IC) which cannot be oxidized become ash as combustion residues. Throughout the smouldering process, the heat released by oxidation reactions is used to balance system heat losses, evaporate fuel moisture, maintain and preheat fuel temperature, and sustain the endothermic pyrolysis reactions.

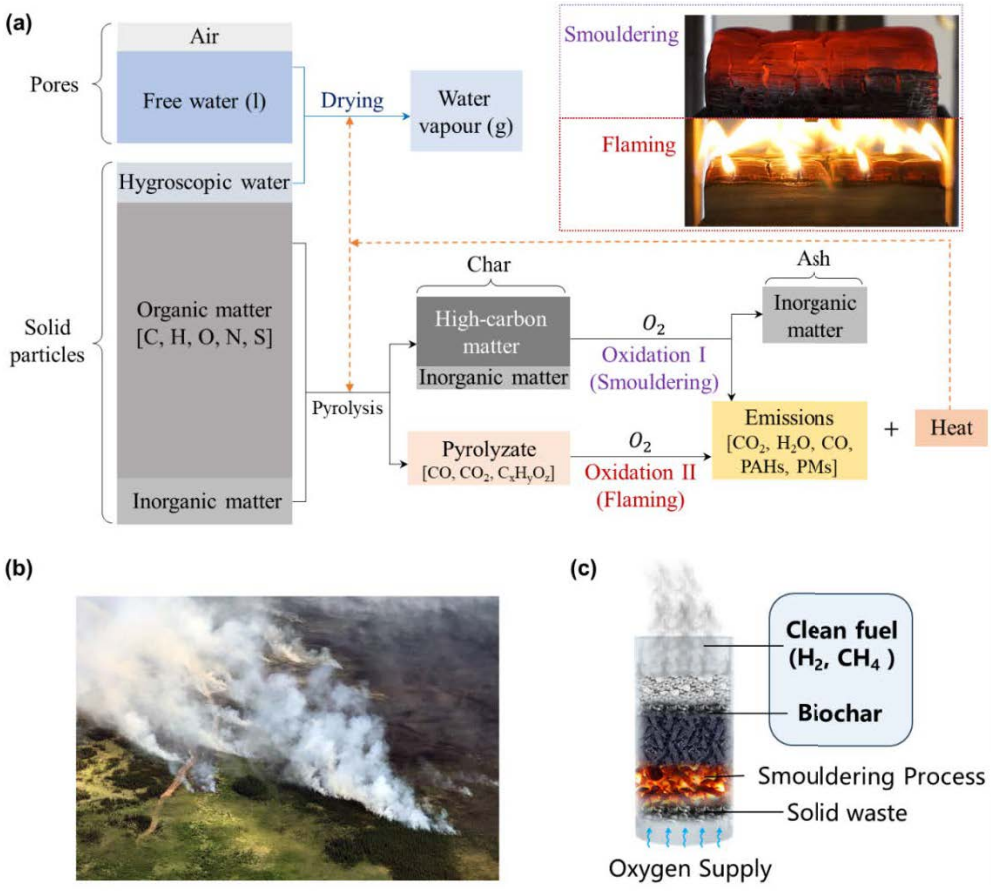

Fig. 1-1 Chemical pathways of flaming and smouldering in charring solid fuels, with examples of smouldering and flaming in wood (**a**); smouldering peatland fire around the Swan Lake in Alaska in 2019 (photo by Kale Casey, Alaska Division) (**b**); and clean biomass removal technology based on smouldering combustion (**c**).

Smouldering fires can be sustained under extreme conditions of high moisture content (MC >100%, dry basis) and can burn at very low oxygen concentrations. Therefore, smouldering can be uncontrolled wildfires (**Fig. 1-1b**) and clean biomass removal technologies (**Fig. 1-1c**). Some experiments have measured its critical oxygen concentration to be less than 10% (Richter *et al.* 2021). In contrast, sustaining flaming combustion usually requires at least 14–16% oxygen concentration, and flame-retardant materials need environments with oxygen concentrations higher than atmospheric levels (21%) to maintain combustion (Quintiere 2016). Even if the oxygen concentration is high, flames are difficult to sustain without sufficient airflow, such as in microgravity environments (Fujita 2015; Wu *et al.* 2020). Smouldering peat fires and underground coal fires are among the largest and longest-lasting fire phenomena on Earth (Rein 2013). For example, influenced by climate change, Southeast Asia has frequent smouldering peat fires since 1991, with the most severe incidents occurring in 1997, 2006, 2009, 2013, and 2015 (Koplitz *et al.* 2016). During the 1997 El Niño event alone, massive peat fires in Indonesia triggered a notorious transboundary haze event that lasted over half a year, resulting in severe air pollution in densely populated areas and significantly affecting public health (Heil and Goldammer 2001; Page *et al.* 2002). Smouldering peat fires also occur in northern and boreal regions such as Siberia and North America (**Fig. 1-1b**). In recent years, increasing remote sensing monitoring (McCarty *et al.* 2020; Scholten *et al.* 2021; Xu *et al.* 2022) and experimental evidence (Qin *et al.* 2022a; Zhang *et al.* 2024) have confirmed the existence of "overwintering fires": smouldering fires in cold regions can hibernate underground in low temperature environment and re-emerge to the surface when temperatures rise and fuels dry out in the following year, and even igniting surface flaming fires (Zhang *et al.* 2024). Even during underground propagation, smouldering fires continuously emit large amounts of greenhouse gases (GHGs) like CO_2 and CH_4 into the atmosphere, exacerbating climate change and the greenhouse effect in the Arctic region, leading to global issues such as glacier melting and permafrost thawing (Webb *et al.* 2021; Hermesdorf *et al.* 2022). Although smouldering fires on a global scale have attracted some attention, our current understanding of them is still limited. **Therefore, an in-depth investigation of the critical oxygen conditions, emission characteristics, and public health impacts for smouldering fires is of great significance for understanding and controlling large-scale natural disasters.**

1.2 Aims and objectives

This project aimed to perform a comprehensive investigation on smouldering fires, focusing on the combustion limits, emission prediction and public health impacts. Specifically, the thesis was accomplished by addressing the following objectives:

- The fire behaviour and oxygen supply thresholds were investigated to help understand persistent smouldering fires under deep peat layers.
- A machine learning model was developed to predict the emission factors (EFs) of various wildland-urban interface (WUI) fuels.
- The public health impacts of typical smouldering wildfires in South-east Asia were assessed using satellite data, chemical transport model (CTM), and epidemiological model.

1.3 Research significance

Smouldering fires pose significant risks to the environment and public health due to their prolonged burning and massive emissions. However, the fundamental understanding of their combustion dynamics, emission characteristics, and health impacts remains limited. This study addresses these knowledge gaps through a comprehensive investigation of smouldering fires.

First, this research advances the understanding of behaviours of underground smouldering fires, particularly their persistence, propagation, and emissions from deep peat layers. In addition, this thesis conducts both experimental and numerical studies to examine the oxygen threshold for smouldering, including the limiting oxygen concentration (LOC), minimum oxygen supply rate ($\dot{m}''_{ox,min}$), and their influencing factors. It contributes critical insights into the fundamental mechanisms of smouldering combustion.

Second, by employing machine learning algorithms, this study develops an emission

prediction model for different WUI fuels, facilitating more accurate fire emission estimates and providing essential data for assessing the associated public health impacts.

Third, this research extends its impact on public health by assessing the health risks of smouldering wildfires in Southeast Asia, a highly dense region with significant peat fires. By integrating burned area data, emission factors, and epidemiological models, the study quantifies the health burden of smouldering fire emissions, providing essential evidence for policymakers and fire management authorities.

Overall, this study contributes to combustion and fire science, atmospheric research, and public health by offering new methodologies and predictive tools for understanding smouldering combustion and evaluating its societal impacts.

1.4 Thesis outline

This thesis comprises three peer-reviewed publications and two ongoing studies conducted during my PhD. It is structured in a manuscript-style format:

Chapter 1 introduces the research background (Chapter 1.1), aims (Chapter 1.2), and significance (Chapter 1.3).

Chapter 2 presents the literature review on three aspects that mirror the three objectives of this thesis, namely the oxygen thresholds of smouldering combustion (Chapter 2.1), wildfire emissions and chemical transport models (Chapter 2.2), and health effects of wildfire emissions (Chapter 2.3).

Chapter 3 describes the methodology of this thesis, including lab experiments (Chapter 3.1), numerical simulations (Chapter 3.2), machine learning (Chapter 3.3), earth-scale chemical transport modelling (Chapter 3.4), and epidemiological model (Chapter 3.5).

Chapter 4 performs large-scale laboratory experiments (1 meter in height) to demonstrate persistent smouldering phenomena and observe fire behaviour under oxygen-limited conditions. It is based on peer-reviewed paper: **Y. Qin**, D. Musa, S. Lin* and X. Huang* (2022). Deep Peat Fire Persistently Smouldering for Weeks: A Laboratory

Demonstration. ***International Journal of Wildland Fire***, 32, 86-98.

Chapter 5 presents the design of a novel reactor that allows precise control and measurement of the oxidizer flow entering the smouldering reaction zone. This enables the definition of the oxygen threshold, including both the limiting oxygen concentration and flow rate, for a representative porous fuel. It is based on peer-reviewed paper: **Y. Qin**, Y. Chen, S. Lin* and X. Huang* (2022). Limiting Oxygen Concentration and Supply Rate of Smouldering Propagation. ***Combustion and Flame***, 245, 112380.

Chapter 6 develops a computational model and validates it using previous experimental data. This enables the prediction of the influence of additional fuel properties and environmental temperatures on smouldering oxygen thresholds. It is based on peer-reviewed paper: **Y. Qin**, Y. Chen, Y. Zhang, S. Lin* and X. Huang* (2024). Modeling Smothering Limit of Smouldering Combustion: Oxygen Supply, Fuel Density, and Moisture Content. ***Combustion and Flame***, 269, 113683.

Chapter 7 establishes a novel machine learning model for predicting CO_2, CO, and total particulate matter (TPM) emissions from WUI fires. Emission factor dataset was compiled from available literature and used for training an Artificial Neural Network model. This chapter is based on an unpublished on-going work.

Chapter 8 evaluates public health impacts from smouldering fires. Taking the large-scale smouldering peat fires in Southeast Asia in 2014-2016 as a case study, this chapter utilizes two global fire datasets, GFED4 (Global Fire Emission Database, version 4.1) and GFAS (Global Fire Assimilation Systems, version 1.2), which provide fire burned area and fire radiative power data. The GEOS-Chem (Goddard Earth Observing System - Chemistry) atmospheric chemistry model is employed to estimate the transport of $PM_{2.5}$ emissions in the atmosphere. Finally, the GEMM (Global Exposure Mortality Model) is used to assess premature deaths associated with the smouldering fire event. This chapter is based on an unpublished on-going work.

Chapter 9 highlights the key conclusions of this thesis and outlines potential future research directions.

CHAPTER 2 Literature review

2.1 Oxygen thresholds of smouldering combustion

Smouldering is a heterogeneous process driven by direct oxygen interaction with the hot solid surface. Fundamentally, as a combustion process, oxygen supply is a key mechanism that controls smouldering reactions.

2.1.1 Smouldering oxygen supply modes

Oxygen supply modes in smouldering are typically divided into two categories: natural oxygen supply (**Fig. 2-1a**) and forced oxygen supply (**Fig. 2-1 b-d**). In the case of natural diffusion oxygen supply, air (oxygen) can be transported from the external environment to the smouldering reaction zone driven by natural/free convection and diffusion. For example, natural convection due to buoyancy plays a dominant role in oxygen supply for surface smouldering fires where the environmental wind is neglected. In contrast, in underground fires that spread in deeper layers, the concentration gradient formed after the consumption of limited oxygen makes oxygen diffusion the dominant form of oxygen supply (Palmer 1957; Rein *et al.* 2016). In the one-dimensional (1-D) deep underground smouldering scenario,

$$\dot{m}''_{ox}(y) = -\bar{\psi} D \frac{\partial Y_{O_2}}{\partial y} \qquad (Diffusion) \qquad (2.1)$$

where y represents the distance between the smouldering front and the free surface. The term $\dot{m}''_{ox}(y)$ denotes the diffusive oxygen supply flux driven by the concentration gradient at different depths (in g/m^2·s). $\bar{\psi}$ is the average porosity within the porous medium. D is the diffusion coefficient of oxygen in the porous fuel, influenced by factors such as temperature and the porosity of the porous material. The expression $\frac{\partial Y_{O_2}}{\partial y}$ represents the oxygen concentration gradient at depth y.

Forced oxygen supply includes **(1) forced external flow**: convection where airflow passes over (**Fig. 2-1b**) or toward the fuel surface (**Fig. 2-1c**), such as in surface smouldering fires under the influence of environmental wind, and **(2) forced internal flow**: directly introducing air into the porous fuels (e.g., controlling oxygen supply variables in laboratory smouldering experiments or airflow introduced in smouldering solid waste treatment devices). In the scenarios of forced external flow on the fuel surface (**Fig. 2-1c**),

the actual oxygen flux at depth y, denoted as $\dot{m}''_{ox}(y)$ can be estimated using Darcy's law:

$$\dot{m}''_{ox}(y) = \frac{K\Delta p}{\mu y} \cdot Y_{O_2} \qquad (Forced\ external\ \ flow) \qquad (2.2a)$$

where $\dot{m}''_{ox}(y)$ is the oxygen flux at depth y. K is the permeability of the porous fuel, which is related to properties such as material porosity and pore shape. μ is the dynamic viscosity of the gas, influenced by factors like gas temperature, concentration, and composition. Y_{O_2} is the mass fraction of oxygen in the gas. Δp is the pressure difference between depth y and the fuel surface caused by the external forced flow. In the scenarios of forced internal flow (**Fig. 2-1d**), the oxygen supply obtained by the smouldering reaction is directly controlled by the gas flow rate:

$$\dot{m}''_{ox} = \psi \rho_g Y_{O_2} U \qquad (Forced\ internal\ flow) \qquad (2.2b)$$

where $\dot{m}''_{ox}$ is the oxygen flux within the pores. ψ is the porosity of the porous fuel. ρ_g is the density of the incoming gas. U is the gas flow velocity.

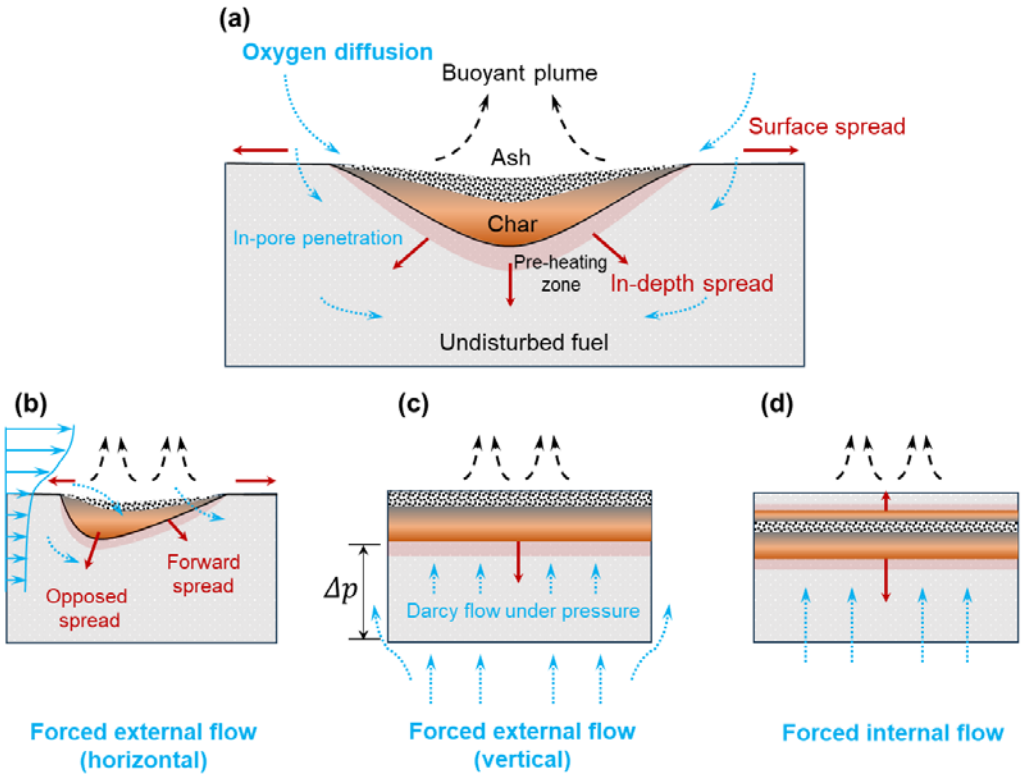

Fig. 2-1 Two different oxygen supply scenarios of smouldering combustion: natural diffusion **(a)**; forced horizontal external flow **(b)**; forced vertical external flow **(c)**; and forced internal flow **(d)**.

Based on the fundamental smouldering oxygen supply models discussed above, several existing experiments and numerical simulations at different scales have explored the oxygen supply limits of smouldering. In the following section, current research methods and results will be reviewed respectively.

2.1.2 Current methodology

Currently, experiments are the primary approaches for exploring the oxygen supply characteristics of smouldering combustion, which can be categorised into micro- and small-scale studies based on the experimental scale. However, to date, no studies have investigated the effects of critical oxygen conditions for smouldering through field combustion experiments. This is because such experiments require strict control of oxygen supply conditions, and it's challenging to avoid the influence of environmental wind during on-site field tests.

Micro-scale experiments primarily include methods based on TGA, electron spin resonance (ESR), and their couples with Fourier-transform infrared spectroscopy (FTIR) to explore the kinetics mechanisms of pyrolysis and smouldering. TGA analysis is an important approach for studying pyrolysis chemistry in combustion and fire (Christensen *et al.* 2019). In these experiments, milligram-level samples are placed in a controlled oxygen concentration environment, and a controlled temperature ramp is provided (**Fig. 2-2**) to obtain the fuel mass loss curve at different temperatures. This is often coupled with FTIR to analyse gas emissions (Anca-Couce *et al.* 2012; Cancellieri *et al.* 2012). In TGA analysis, mass loss curves under air and inert atmospheres are typically compared to infer the oxidation reaction rates at different oxygen concentrations, thereby determining whether smouldering reactions occur. The ESR method is used for reaction analysis at the molecular scale. By measuring the area of the spin resonance spectrum, it indirectly quantifies the concentration of free radicals in the fuel under specific oxygen environments, thus inferring the likelihood of combustion reactions occurring (Zhou *et al.* 2021).

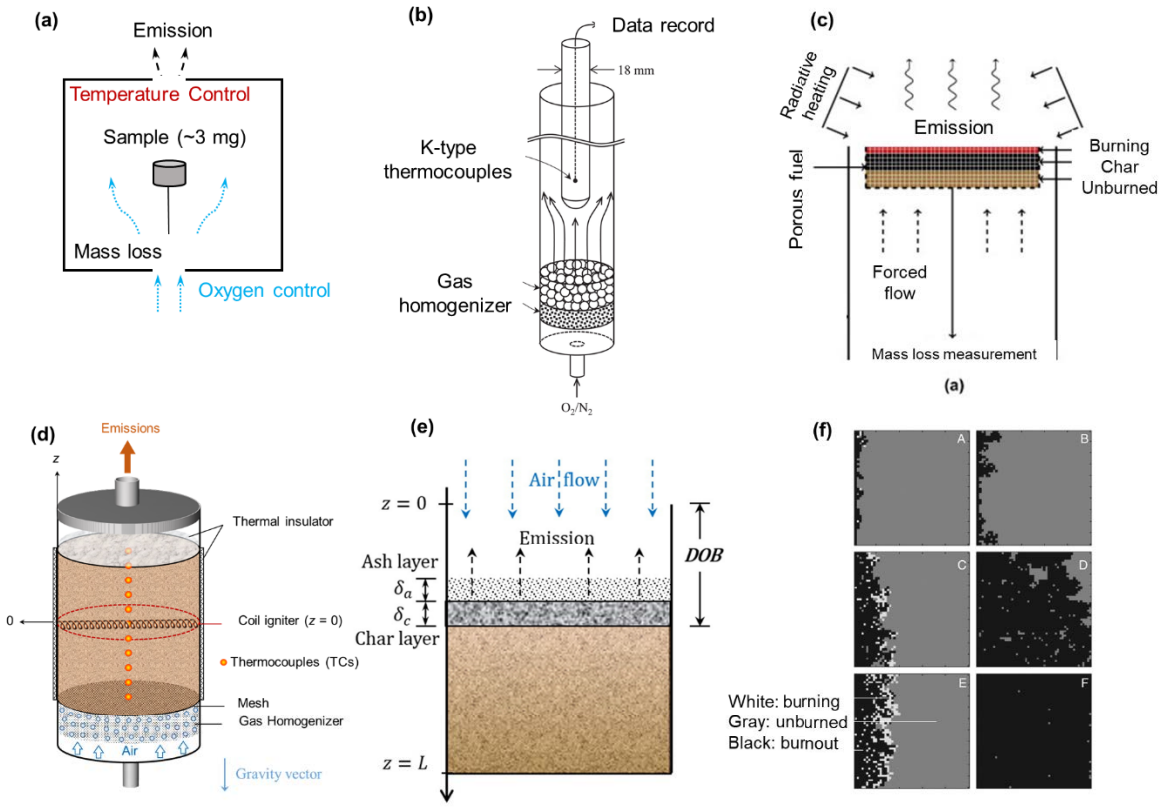

Fig. 2-2 Current representative experimental and computational setups on smouldering oxygen supply limits.

Methods for small-scale research on smouldering have been systematically elaborated previously (Christensen *et al.* 2019). However, small-scale experimental studies on the critical oxygen supply characteristics of smouldering typically require introducing an oxygen supply system capable of controlling flow rate and concentration based on the original experiments. External forced oxygen supply experiments usually direct the oxidiser onto the fuel surface (**Fig. 2-2b**) (Kadowaki *et al.* 2021), or utilise standard fire testing methods based on the Fire Propagation Apparatus (FPA) to provide external forced convective oxygen supply and control radiant ignition power (**Fig. 2-2c**) (Hadden *et al.* 2013). Nevertheless, this approach makes it difficult to determine the actual amount of oxygen reaching the smouldering front within the porous fuel and cannot eliminate the influence of natural oxygen diffusion at the surface of the fuel container. Therefore, small-scale experiments often employ internal forced oxygen supply methods, directly measuring the total oxygen supply introduced into the smouldering system using a flow meter (**Fig. 2-2d**) (Qin *et al.* 2024).

In small-scale experiments, oxidiser flows of various concentrations are usually obtained by mixing pure air with nitrogen or argon gases. To ensure the uniform flow of the mixed gases within tubular containers, gas homogenising layers composed of metal mesh, glass beads, or gravel are typically installed at the inlet or before the gases enter the container. For near-limit critical smouldering experiments, precise control of ignition protocol is also crucial for exploring the critical oxygen supply conditions. Common ignition methods in small-scale experiments include radiant ignition (Hadden *et al.* 2013), variable power coil ignition (Qin *et al.* 2022b, 2024), and heated rod ignition (Yan and Fujita 2019). Different ignition methods can achieve various smouldering ignition intensities by controlling the applied radiation intensity (radiant heat flux) or the conductive temperature of the metal igniter. In addition to directly observing combustion phenomena, thermocouples and infrared cameras are also commonly used to detect temperatures, indirectly inferring whether the current oxygen supply conditions are sufficient to sustain smouldering. In terms of large-scale experiments, there are very few large-scale experimental studies on smouldering combustion and fires in the literature due to the challenges in monitoring and extinguishing smouldering fires. The existing largest study is the GAMBUT experiment conducted in Indonesia (10 m × 10 m) (Santoso *et al.* 2022). However, it is difficult to effectively control environmental wind in natural settings to explore the impact of oxygen supply. Therefore, such studies only focus on the ignition, propagation, extinction, and emission dynamics of smouldering fires.

Numerical simulations of the oxygen supply characteristics of smouldering are relatively limited and can be categorised into physical models based on heat and mass transfer and statistical models using discrete event simulations. A typical 1-D smouldering physical model is shown in **Fig. 2-2e**, which has been used to simulate ignition, fire spread, and extinction in smouldering (Huang *et al.* 2015; Lin *et al.* 2022a). This model includes heterogeneous chemical reactions and heat and mass transfer processes between the gas and solid phases within a porous medium. It assumes thermal equilibrium at the same location in the system, that is, efficient heat exchange within the porous medium, where the gas and solid phases share the same temperature within the same grid cell. The main governing equations in the model are consistent with those used in the open-source software Gpyro (Lautenberger and Fernandez-Pello 2009), including the conservation of (2.3) mass, (2.4) species, and (2.5) energy in the condensed phase, as well as the conservation

of (2.6) mass, (2.7) species, and (2.8) momentum (Darcy's law) in the gas phase.

$$\frac{\partial \bar{\rho}}{\partial t} = -\dot{\omega}'''_{fg} \tag{2.3}$$

$$\frac{\partial (\bar{\rho} Y_i)}{\partial t} = \dot{\omega}'''_{fi} - \dot{\omega}'''_{di} \tag{2.4}$$

$$\frac{\partial (\bar{\rho}\bar{h})}{\partial t} + \frac{\partial (\dot{m}'' \bar{h}_g)}{\partial z} = \frac{\partial}{\partial z}\left(k \frac{\partial T}{\partial z}\right) + \sum \dot{\omega}'''_{di,k} \Delta H_k \tag{2.5}$$

$$\frac{\partial (\rho_g \bar{\psi})}{\partial t} + \frac{\partial \dot{m}''}{\partial z} = \dot{\omega}'''_{fg} \tag{2.6}$$

$$\frac{\partial (\rho_g \bar{\psi} Y_j)}{\partial t} + \frac{\partial (\dot{m}'' Y_j)}{\partial z} = -\frac{\partial}{\partial z}\left(\rho_g \bar{\psi} D \frac{\partial Y_j}{\partial z}\right) + (\dot{\omega}'''_{fj} - \dot{\omega}'''_{dj}) \tag{2.7}$$

$$\dot{m}'' = -\frac{\overline{K}}{\nu}\frac{\partial \bar{p}}{\partial z} \quad (\rho_g = \frac{P\overline{M}}{RT}) \tag{2.8}$$

In addition to traditional physical models, discrete statistical models based on Cellular Automata (CA) have also been used to study the critical oxygen conditions for smouldering combustion **Fig. 2-2f** (Belcher *et al.* 2010). CA consist of a large number of regular units, and they exhibit complex global behaviour by simulating local interactions between adjacent cells (Wolfram 1983). CA models have been widely applied not only in natural system simulations, image processing, and crowd behaviour modelling, but their characteristic of "neighbour cell interactions" also makes them highly suitable for simulating fire spread phenomena. For example, existing smouldering CA models have already achieved simulations of smouldering fire spread under varying MC (Purnomo *et al.* 2023, 2024), field-scale simulations (Purnomo *et al.* 2021), and complex fire spread behaviours such as fingering spread (Fernandez-Anez *et al.* 2019). In the study of critical oxygen conditions based on CA (Belcher *et al.* 2010), a grid of 50 × 50 cells is first established, where each cell can be in one of three states: "unburned", "burning", and "burned out". The model also includes two parameters: the local fire spread probability β and the local fire extinction probability μ. Through extensive simulations with random values of these two parameters to compare with experimental results, the optimal parameter choices are finally determined, and the model's applicability is validated.

Table 2-1 summarizes the micro-scale and small-scale experimental and simulation studies in the existing literature related to the critical oxygen supply characteristics of smouldering combustion, including the fuel types, configurations, and oxygen supply

modes.

Table 2-1 Experimental information on the LOC of smouldering combustion, sorted by fuel type and study scale.

Fuel	Configurations	Study type	Oxygen supply mode	LOC	Ref.	Remarks
Peat	Disclosed cylindrical reactor, H=30 mm, D=125 mm	Small-scale experiment	Forced external flow concentration 9-35% fixed flow rate 20-150 mm/s	10%	Hadden et al. 2013 (Hadden *et al.* 2013)	Burning rate after ignition is independent of external heating
Peat	1D mode, H=12 cm	Numerical simulation	Diffusion under different oxygen concentration	13%	Huang and Rein. 2016 (Huang and Rein 2016a)	Relationship between critical oxygen concentration and critical water content of fuel
Peat	Simulation domain 10 × 10 cm, grid 50 × 50	Numerical simulation (CA)	Diffusion under different oxygen concentration	16%	Belcher et al. 2010 (Belcher *et al.* 2010)	Verification based on combustion rate and time in experiments
Pine dust	Disclosed square reactor, H=12 cm, l=3.8 cm	Small-scale experiment	Forced internal flow concentration 5-21% fixed flow rate 15 mm/s	5%	Wang et al. 2017 (Wang *et al.* 2017a)	Relationship between limiting concentration and external heating
Moxa rod	Fuel rod, D=18 mm	Small-scale experiment	Forced external flow Fixed flow 18L/min	13.5%	Kadowaki et al. 2021 (Kadowaki *et al.* 2021)	Quenching is due to the limited char oxidation rate in the absence of oxygen.
Wood brick	Dimension 8 × 8 × 3 cm	Small-scale experiment + Numerical simulation	Exp: Forced external flow concentration 0-21% flow rate: 200L/min Sim: natural diffusion	4% (ig.)	Richter et al. 2021 (Richter *et al.* 2021)	LOC is affected by external radiation intensity
Paper scraps	Disclosed cylindrical reactor,	Small-scale experiment	Forced internal flow	N. A.	Yan and Fujita, 2019	Influence of density and

	H=15 mm, D=20 mm		Concentration 21% Max. flow rate 18 cm/s		(Yan and Fujita 2019)	heating rod temperature
Coal	5 mg	ESR Micro-scale experiment	Forced external flow Concentration 3-21% Fixed flow 50 mL/min	9%	Zhou et al. 2021 (Zhou *et al.* 2021)	Determining the oxygen limit by measuring free radicals and reaction rates
PMMA	Cylindrical fuel, D=13.2 cm, l=15 cm	Small-scale Experiment (microgravity)	Forced internal flow Max. flow 3.66 g/m^2·s	N. A.	BAR-ILAN et al., 2004 (Bar-Ilan *et al.* 2004)	Microgravity experiment; explored the role of buoyancy in smouldering

2.1.3 Findings from existing studies

In small-scale studies, it is challenging to experimentally explore the critical oxygen concentration under natural diffusion. Therefore, the limiting diffusive oxygen supply is usually solved by numerical simulation. One study on wood blocks identified the oxygen concentration ranges required for pyrolysis, smouldering, and flaming under different heat fluxes (**Fig. 2-3a**): <4% for pyrolysis, 4-15% for smouldering, and >15% for flaming. It is important to note that the smouldering limits this study only focuses on ignition phase.

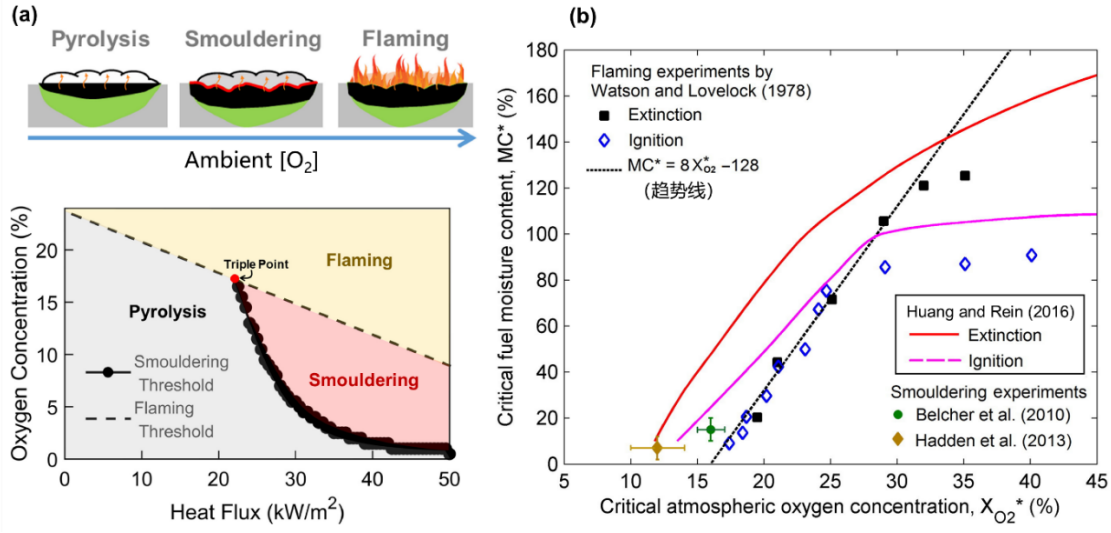

Fig. 2-3 Transitions from pure pyrolysis to smouldering, then to flaming by increasing oxygen concentration **(a)**; Critical moisture content vs. critical ambient oxygen volume fraction **(b)**.

Another computational study based on physical model also identified the relationship between the critical oxygen concentration ($X_{O_2}^*$) and the critical moisture content (MC^*) (Huang and Rein 2016a) (**Fig. 2-3b**). The results indicate that as MC increases, the critical oxygen concentration for smouldering ignition and fire spread rises significantly. Compared to flaming combustion, smouldering can sustain under higher fuel MC (with a conventional oxygen concentration of X_{O_2} =21%, the MC^* for smouldering reaches up to 100%, while for flaming it is only 40%) and lower oxygen concentration (smouldering $X_{O_2}^*$ =13%, flaming 16%). However, CA simulations yielded higher results: it showed that smouldering reactions are suppressed at oxygen concentrations below 18.5% and completely cease at concentrations below 16%. The study also re-assessed Earth's flammability limits over the past 350 million years based on these findings (Belcher *et al.* 2010).

Furthermore, there is a study employed an internal forced oxygen supply model in smouldering pine sawdust (Wang *et al.* 2017a). It found that the critical oxygen concentration required for smouldering is related to external heating. Self-sustained smouldering can only be initiated when the oxygen concentration is between 10% and 21%. When the oxygen concentration decreased below 7.5%, sustaining smouldering combustion requires additional external radiant heating. At oxygen concentrations of 5% or lower, smouldering cannot occur, even with the assistance of external heating.

Studies under forced external supply is found to have critical oxygen concentration than that observed with internal oxygen supply. Representative studies include directly applying airflow to the surface of ignited fuel (Kadowaki *et al.* 2021) (**Fig. 2-2b**) and using the FPA to control ignition intensity and oxygen supply conditions (Hadden *et al.* 2013) (**Fig. 2-2c**). These studies determined critical oxygen concentrations of 13.5% (**Fig. 2-4a**) and 10% (**Fig. 2-4b**) for external forced oxygen supply. Similarly, both studies found that char content was higher in quenched fuel when oxygen concentration was insufficient (**Fig. 2-4b**), indicating that the limited char oxidation to release sufficient heat is the primary reason for smouldering extinction. As the oxygen concentration increased, both experiments observed higher fire spread rates, burning temperatures, and fuel mass loss rates. The study in smouldering peat also revealed that the duration of smouldering decreased as oxygen concentration increased (Hadden *et al.* 2013). This helps explain the

phenomenon of persistent smouldering fires in deep underground peat layers.

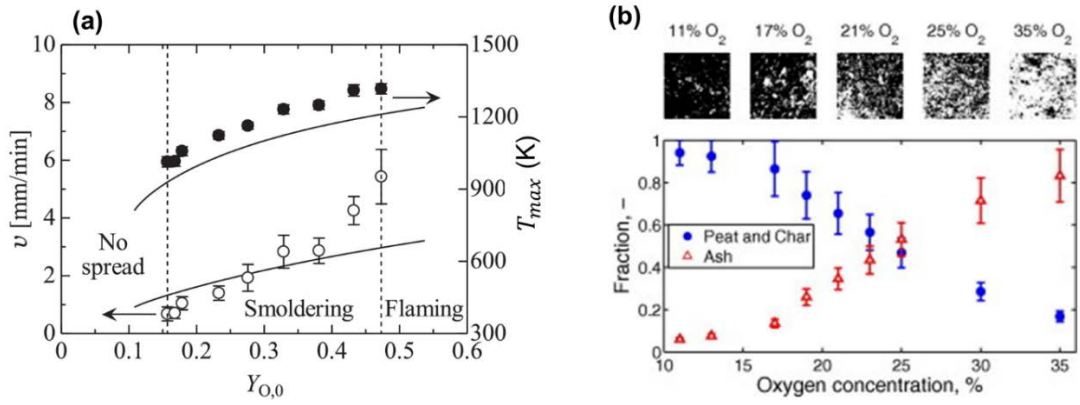

Fig. 2-4 Critical oxygen supply under forced external flow of moxa rod (~13.5%) (Kadowaki et al. 2021) **(a)**; and peat soil (~10%) (Hadden et al. 2013) **(b)**.

Although there are relatively few studies on critical oxygen supply rates in the literature, it plays important role in the ignition and extinction of smouldering combustion. The critical oxygen supply rates can be influenced by both fuel properties and environmental conditions. A study on smouldering ignition in paper scraps found that in low-density fuel, there is sufficient oxygen within the gaps of the porous material during ignition. As a result, ignition can occur successfully even without additional oxygen supply. However, excessively high airflow rates can enhance internal convective heat loss, leading to failed ignition (**Fig. 2-5a**). When the fuel bulk density (ρ_b) increases, oxygen supply becomes the primary factor controlling ignition success, as shown by the U-shaped trend in **Fig. 2-5 b-c**, where ignition fails both under insufficient oxygen supply and excessive airflow rates.

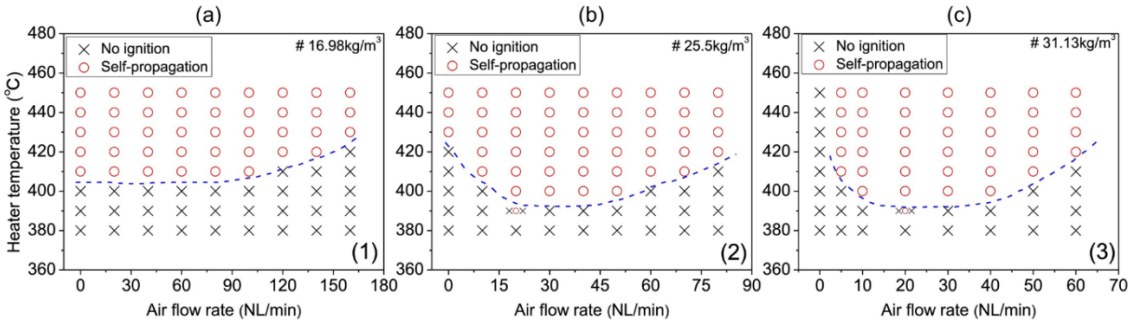

Fig. 2-5 Effects of ignition temperature and air flow rate on ignition behaviour in the smouldering ignition experiment of wastepaper with different densities (Yan and Fujita 2019).

The influence of environmental conditions on the critical oxygen supply rate for smouldering is primarily reflected in the heat loss at system boundaries (Carvalho *et al.* 2002; Torero *et al.* 2020). However, no previous studies have systematically explored the impact of boundary heat loss on the smouldering oxygen supply limit. Additionally, gravity and buoyancy may also influence smouldering in porous fuels. One study used polyurethane foam as fuel, and compared the results of forced flow tests under normal gravity with those in microgravity (Bar-Ilan *et al.* 2004). The results showed that under normal gravity, self-sustained propagation required approximately 0.5-0.8 $g/m^2 \cdot s$ of air mass flux. In contrast, this critical air mass flux decreased to 0.3 $g/m^2 \cdot s$ under microgravity conditions. This is due to the removal of gravity reduces buoyancy-driven heat loss, allowing smouldering to be sustained under lower oxidation rates.

In summary, even though numerous experimental and numerical studies have explored limiting oxygen supply characteristics in near-limit smouldering, most have been conducted under quiescent ambient conditions or with external wind, which cannot completely isolate oxygen diffusion from the surroundings. This has led to knowledge gaps: (1) the fundamental research problem of the actual minimum oxygen rate required to sustain smouldering remains unclear. (2) the roles of fuel properties and environmental conditions are still not well understood. (3) Even for the same fuel, varying values of LOC are reported due to different setup and boundary conditions. Hence, further systematic investigation in smouldering oxygen thresholds is required.

2.2 Wildfire emissions and chemical transport models

2.2.1 Overview of global wildfire emissions

Smoke from wildland fires comprises a complex mixture of particles (e.g., $PM_{2.5}$), CO, volatile organic compounds (VOCs), and other toxic substances that pose significant threats to human health. Notably, nearly half of the global population (3.5 billion) resides in WUI areas (Schug et al. 2023), where residents live near flammable landscapes. This increases the number of individuals exposed to wildfire smoke, elevating the risk of both acute and chronic health issues. It is estimated that 2.18 billion people were exposed to at

least one day of significant wildfire air pollution annually during 2010-2019, with an average global exposure of 9.9 days per person per year, which rose by 6.8% and 2.1% compared to 2000–2009, respectively (**Fig. 2-6**) (Xu et al. 2023). Vulnerable populations, including children, the elderly, pregnant women, and those with pre-existing respiratory or cardiovascular conditions, are particularly susceptible to the adverse effects of smoke inhalation (Rappold et al. 2017). Acute exposure can result in respiratory distress, eye irritation, and exacerbated cardiovascular problems, while long-term exposure may lead to premature death and elevated mortality rates.

Moreover, wildfire smoke can remain stable in the atmosphere and undergo long-distance transport, leading to transboundary haze events that impact regions far from the original fire sources. Regions affected by those notorious events span across the globe, from tropical Southeast Asia to the Arctic Circle (Aouizerats et al. 2015; Silver et al. 2024). For example, during the 2006 El Niño event, 21% of the total aerosol in Singapore was originated from fire activities in Sumatra, Indonesia (Silver et al. 2024). In longer temporal and spatial scales, it is estimated that between 2001 and 2014, 17% of BaP (Benzo(a)pyrene, the most toxic polycyclic aromatic hydrocarbons) concentrations in Southern Europe could be traced back to sources in Africa (Wu et al. 2022). The trans-boundary haze caused by smoke from these fires not only results in severe health impacts on the residents from the source and affected countries, but also leads to severe economic burden, psychosocial costs and geopolitical tensions (Quah 2002; Du et al. 2024).

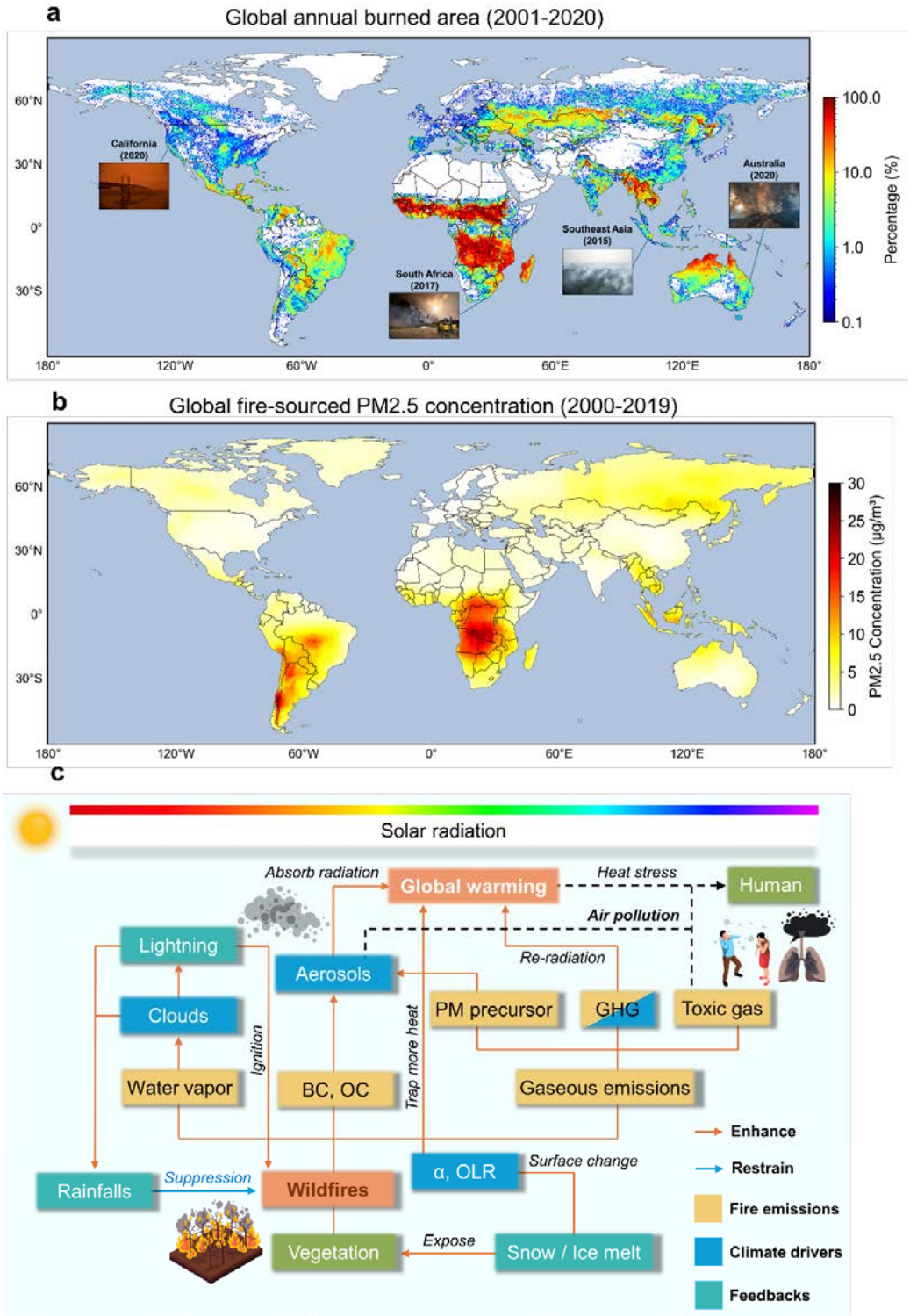

Fig. 2-6 Global distribution of mean annual Burned Area (BA) from 2001 to 2020 (Data source: GFED5 in Chen et al. 2023b) **(a)**; and Global distribution of mean fire-sourced $PM_{2.5}$ concentration from 2000 to 2019 estimated by model (Data source: Xu et al.. 2023) **(b)**.

2.2.2 Emission sampling and emission factor calculations

Gaseous toxic emissions from wildland fires often concern CO, nitrogen oxides (NO_x), hydrogen cyanide (HCN) and VOCs. FTIR and Proton transfer reaction mass spectrometry (PTR-MS), and Gas chromatography with mass spectrometry (GC-MS) are most common monitoring instruments, depending on the specific species and monitoring scenarios. Among them, FTIR can detect a broad spectrum of trace gases by measuring their infrared absorption spectra and provide real-time data without much sample preparation procedures. Therefore, it is developed for field *in-situ* measurement as airborne FTIR (AFTIR) (Yokelson 1999; Goode *et al.* 2000) and ground-based mobile FTIR (Christian *et al.* 2007). However, the accuracy (ppmv level) is lower than the other instruments and it is challenging to analyse complex organic mixtures with FTIR. PTR-MS can analyse real-time VOCs emissions with high sensitivity (pptv level), but the species are limited to VOCs despite coupling with other instruments (e.g., GC) (Karl *et al.* 2007; Yokelson *et al.* 2007). GC-MS is capable of analysing complex mixtures, but the samples should be volatile and thermally stable. In addition, Chemiluminescence (CL) is also used to analyse gaseous emissions such as NO_x and ozone (O_3). More comparisons and range of applicable gases are further summarized in **Table 2-2**.

Table 2-2 Comparison of common monitoring equipment for fire gas emissions

Feature	FTIR	PTR-MS	GC-MS	CL
Principle	IR absorption spectra	Proton transfer ionization, MS analysis	GC separation, MS identification	Light emission from chemical reactions
Advantages	Non-destructive, versatile samples	Real-time, high sensitivity	High sensitivity, specificity	Real-time, high sensitivity, specificity
Disadvantages	Relatively low detection limits	Limited to VOCs	Time-consuming	Limited to specific reactions
Applicable toxic gases	CO, HCN, NH_3, SO_2, etc.	VOCs	CO, VOCs, etc.	NO_x, O_3, etc.

In addition to toxic gaseous emissions, aerosols such as PM also have a significant impact on human health, making them worthy of attention. Gravimetric and optical meth-

ods are two basic measurement principles of PM emissions (Cui *et al.* 2023). The gravimetric method uses cascade impactors to collect and categorize PM by their size. For example, when the flue smoke with a fixed flow rate passes through cascade impactors, the PM can be classified as PM_1 (aero-dynamic diameter $\leqslant$ 1 μm), $PM_{2.5}$, PM_{10}, and other PM sizes. This PM measurement method is portable and cost-effective, but it cannot perform continuous monitoring of smoke. In contrast, the optical method can provide real-time mass fraction concentrations including PM_1, $PM_{2.5}$ and PM_{10}. It is based on principals of light scattering, absorption, and extinction. For example, photometers, integrated nephelometers, and optical particle counters are three most common instruments based on optical method (Shukla and Aggarwal 2022). It is important to note that optical scattering instruments are highly sensitive to slight changes in scattering angle, particle size or shape, and particle refractive index (Hinds and Zhu 2022).

Based on its definition, the Emission factor (EF) (g/kg) of species *i* is calculated by mass flux of emission generation and fuel mass loss rate:

$$EF_i = \frac{\dot{m}_i''}{\dot{m}''} \tag{2.9}$$

where $\dot{m}_i''$ (g/s) is the emission flux of species *i* and $\dot{m}''$ (kg/s) is the burning mass loss rate or fuel consumption rate of the dry fuel.

However, fuel consumption rate is difficult to be determined in some situations (e.g., measurement at real fire scenes). Therefore, a carbon balance method was proposed to approximate EFs of each emission (Eq. 2.10) (Ward and Radke 1993; Paton-Walsh *et al.* 2014), especially when the fire smoke contain the majority of the carbon from fires.

$$EF_i = F_c \times 1000\ (g/kg) \times \frac{MM_i}{12} \times \frac{C_i}{C_T} \tag{2.10}$$

where F_c is the fractional carbon content of the fuel, MM_i is the molecular mass of species *i*, 12 is the atomic mass of carbon, and C_i/C_T is the number of moles of species *i* emitted divided by the total number of moles of carbon emitted, which can be further determined by Eq. 2.11:

$$\frac{C_i}{C_T} = \frac{\Delta[i]}{\sum_{j=1}^{n}(NC_j \times \Delta[j])} \tag{2.11}$$

where $\Delta[i]$ and $\Delta[j]$ are the excess mole fractions of species *i* and *j* respectively (defined as the mole fraction, e.g. $[i]$ measured in the smoke, minus the mean background mole fraction measured before the fire $[i]_{background}$), NC_j is the number of carbon atoms in compound *j* and the sum is of all carbon-containing species emitted by the fire (Paton-Walsh *et al.* 2014).

2.2.3 EF of major fire emissions

Fig. 2-7 summarizes current laboratory and field studies that measure the EFs of flaming and smouldering wildland fires. The fuels are categorized as grass (including savanna), forest litter (e.g., pine needles, truck, branches, etc.), peat, crop (e.g., rick straw, wheat straw, etc.), and shrubs. The classification of fuel regions is according to 14 regions in GFED (Giglio *et al.* 2013). The literature on EF-related data shows a greater number of studies conducted under controlled laboratory conditions compared to measurements taken real wildfire scenarios. Additionally, these studies are particularly concentrated on two types of fuels: forest litter and peat. Regardless of laboratory or field study, wildland fuels from Temperate North America (TENA) have received the most attention. The reported number of EF measurements from TENA region exceeds the total from all rest other regions, indicating a higher level of concern about wildfire emissions in this region. In terms of combustion forms, the number of EF reports associated with smouldering combustion is comparable to those associated with flaming combustion. It is worth to note that if the combustion form is not clearly stated in the literature, we classify it based on the associated Modified Combustion Efficiency (MCE) Eq. 2.12:

$$MCE = \frac{\Delta[CO_2]}{\Delta[CO] + \Delta[CO_2]} \tag{2.12}$$

where $\Delta[CO_2]$ and $\Delta[CO]$ are the fire-integrated excess molar mixing ratios of CO_2 and CO (Urbanski 2013). Specifically, MCE values greater than 0.9 indicate flaming combustion, while values below 0.9 indicate smouldering combustion. In terms of emission types, the overall number of EF reports on gaseous and particulate emissions is comparable. Among gaseous emissions, CO and CO_2 receive the most attention, followed by CH_4

and NO_x. In studies related to PM, $PM_{2.5}$ is the primary focus. Many aerosol-related studies report more details on BC, organic carbon (OC), and elemental carbon (EC).

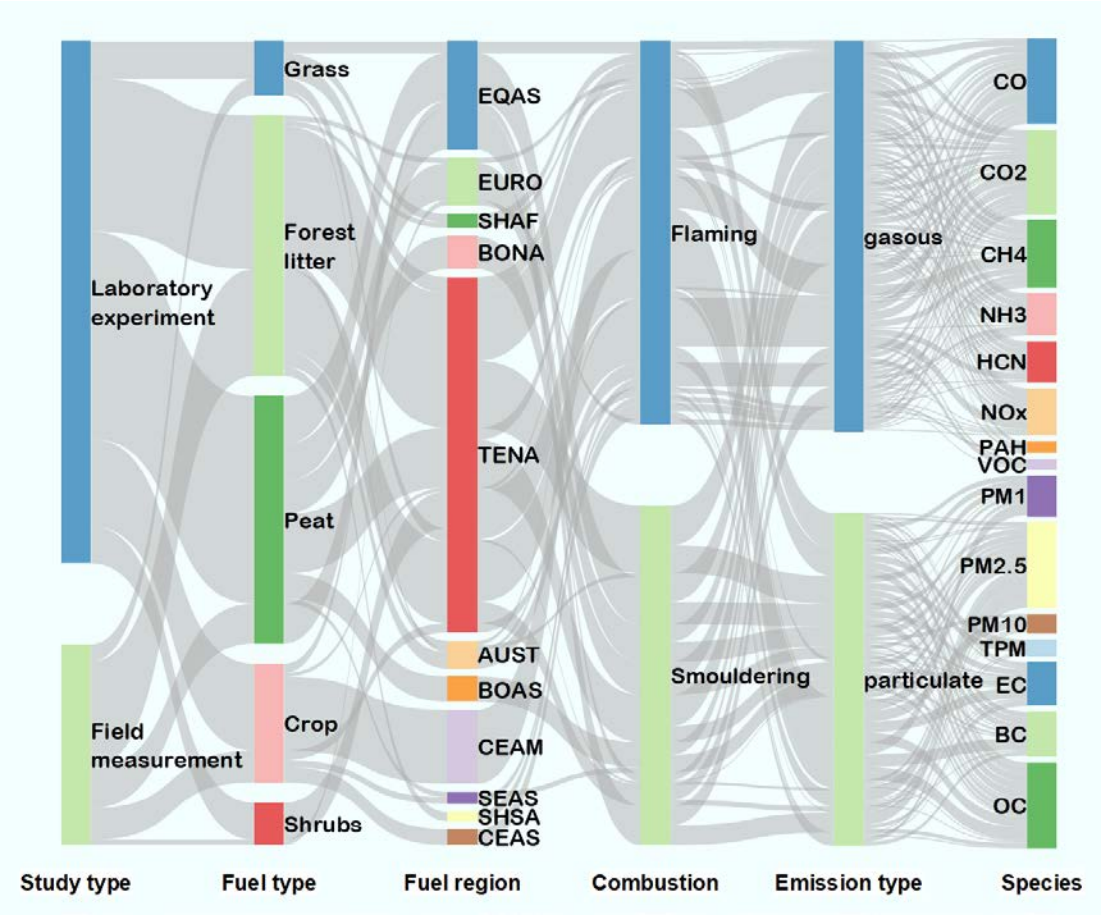

Fig. 2-7 Alluvial diagram of reviewed 42 wildland fire emission studies. The size of nodes reflects the frequency reported in the literature. Fuel region is referred to as in GFED regions: EQAS, Equatorial Asia; EURO, Europe; SHAF, Southern Hemisphere Africa; BONA, Boreal North America; TENA, Temperate North America; AUST, Australia and New Zealand; BOAS, Boreal Asia; CEAM, Central America; SEAS, Southeast Asia; SHSA, Southern Hemisphere South America; CEAS, Central Asia (Giglio *et al.* 2013).

Table 2-3 shows major gaseous and particulate emissions from wildland fuels in laboratory experiments (Christian *et al.* 2003; Chen *et al.* 2007; Iinuma *et al.* 2007; McMeeking *et al.* 2009; Burling *et al.* 2010; Yokelson *et al.* 2013; May *et al.* 2014; Stockwell *et al.* 2014; Black *et al.* 2016; Chakrabarty *et al.* 2016; Santiago-De La Rosa *et al.* 2018; Watson *et al.* 2019; Hu *et al.* 2019b; a; Lestari *et al.* 2020; Nim *et al.* 2023; Garg *et al.* 2024), and field measurements (Ferek *et al.* 1998; Yokelson *et al.* 2003, 2007, 2011, 2013; Sahai *et al.* 2007; Dhammapala *et al.* 2007; Alves *et al.* 2010; Janẖall *et al.*

2010; Burling *et al.* 2011; Urbanski 2013; Vicente *et al.* 2013; Geron and Hays 2013; Robertson *et al.* 2014; Zhang *et al.* 2014; Stockwell *et al.* 2016; Nara *et al.* 2017; Desservettaz *et al.* 2017; Roulston *et al.* 2018; Guérette *et al.* 2018; Jayarathne *et al.* 2018; Li *et al.* 2020; Aurell *et al.* 2021; Urbanski *et al.* 2022; Tomsche *et al.* 2023; Lestari *et al.* 2024). The results are presented as average EF (with standard deviation) for each fuel type, including crop, forest litters, grass, peat, and shrub.

Table 2-3 Comparison of laboratory and field measurement results of EFs for major fire emissions from the literatures (the standard deviation is in brackets).

Fuel	**Crop**		**Forest litters**		**Grass**		**Peat**		**Shrub**	
EF (g/kg)	**Lab**	**Field**	**Lab**	**Field**	**Lab**	**Field**	**Lab**	**Field**	**Lab**	**Field**
CO	80.76 (50.61)	57.25 (20.69)	80.86 (62.57)	113.1 (72.56)	68.7 (43.97)	115.5 (69.2)	183.24 (87.56)	278.97 (52.68)	66.5 (32.5)	73.98 (18.08)
CO_2	1533.62 (285.4)	1731 (48.26)	1322.5 (486.6)	1569.5 (207.85)	1656 (232.7)	1595.6 (160.9)	1327.9 (255.8)	1567.58 (80.86)	1688.9 (128.4)	1670.1 (41.8)
CH_4	3.37 (2.54)	3.77 (1.36)	4.13 (3.97)	3.14 (1.72)	18.51 (43.3)	3.05 (1.69)	9.41 (4.6)	9.82 (4.79)	2.19 (2.1)	6.58 (8.68)
NH_3	2.55 (2.19)	1.33 (0.53)	0.47 (0.08)	1.0 (0.81)	0.97 (0.74)	0.43 (0.21)	5.66 (5.85)	3.03 (0.98)	0.97 (0.84)	1.36 (1.2)
HCN	0.87 (-)	0.37	0.39 (0.46)	0.42 (0.23)	0.16 (-)	0.53 (-)	4.91 (3.69)	5.39 (1.43)	0.1 (0.09)	0.69 (0.2)
NO_x	1.56 (1.33)	2.7 (1.05)	2.31 (1.3)	2.78 (0.79)	3.1 (2.06)	3.92 (1.96)	1.89 (1.2)	0.29 (0.39)	2.81 (1.15)	1.83 (0.7)
VOC	-	8.7 (1.23)	-	28.5 (6.4)	-	-	-	-	-	-
PM_1	3 (-)	-	93.19 (87.94)	-	13.57 (9.44)	-	8.25 (10.99)	-	6.48 (6.88)	-
$PM_{2.5}$	5.72 (4.13)	10.53 (5.24)	7 (5.39)	25.57 (23.01)	10.36 (12)	49.36 (64.54)	18.36 (16.68)	20.64 (11.4)	11.61 (9.78)	6.24 (2.73)
PM_{10}	7.86 (6.92)	8.1 (2.69)	-	28.05 (14.5)	-	30.65 (10.82)	21.16 (3.24)	-	-	-
TPM	-	0.5 (-)	20.73 (21.57)	15 (-)	-	3.3	-	-	-	-
EC	0.22 (0.09)	0.25 (0.07)	1.14 (0.52)	0.3 (-)	2.21 (3.1)	0.7 (-)	0.61 (0.53)	0.14 (0.14)	1 (0.92)	-
BC	0.74 (-)	-	0.77 (0.79)	12.05 (3.75)	1.3 (0.44)	4.88 (6.4)	0.12 (0.08)	-	1.49 (0.42)	-
OC	2.39 (2.04)	1.67 (1.64)	74.39 (87.33)	1.1 (-)	6.33 (6.42)	4.97 (2.87)	15.51 (10.96)	13.22 (5.71)	4.55 (6.6)	-

Among the emissions from wildland fires, substances such as CO, NH_3, Polycyclic Aromatic Hydrocarbons (PAH), VOCs, and PM have the adverse impact on public health. In all types of fuels, CO emissions from peat fires have been observed to be significantly higher than estimated values in both laboratory and field measurements (**Fig. 2-8**). This is because the dominant combustion mode of peat is smouldering, which is a typical form of incomplete combustion, resulting in a large amount of CO. MCE of smouldering is typically below 0.9. In terms of other EFs, both VOCs and other trace gases have relatively low EF values (**Table 2-3**), and the exposures in real fires are generally below the acceptable level (Reisen *et al.* 2006).

Fig. 2-9a provides a comparison of the differences between current results from laboratory field measurement across all natural fuels under similar MCE conditions (difference < 0.02). It shows that, despite the limited data available for comparison, the lab results can effectively represent the field $PM_{2.5}$ emissions measurement ($EF_{PM2.5\_field} = 1.1\ EF_{PM2.5\_lab} - 5.87$, $R^2 = 0.97$).

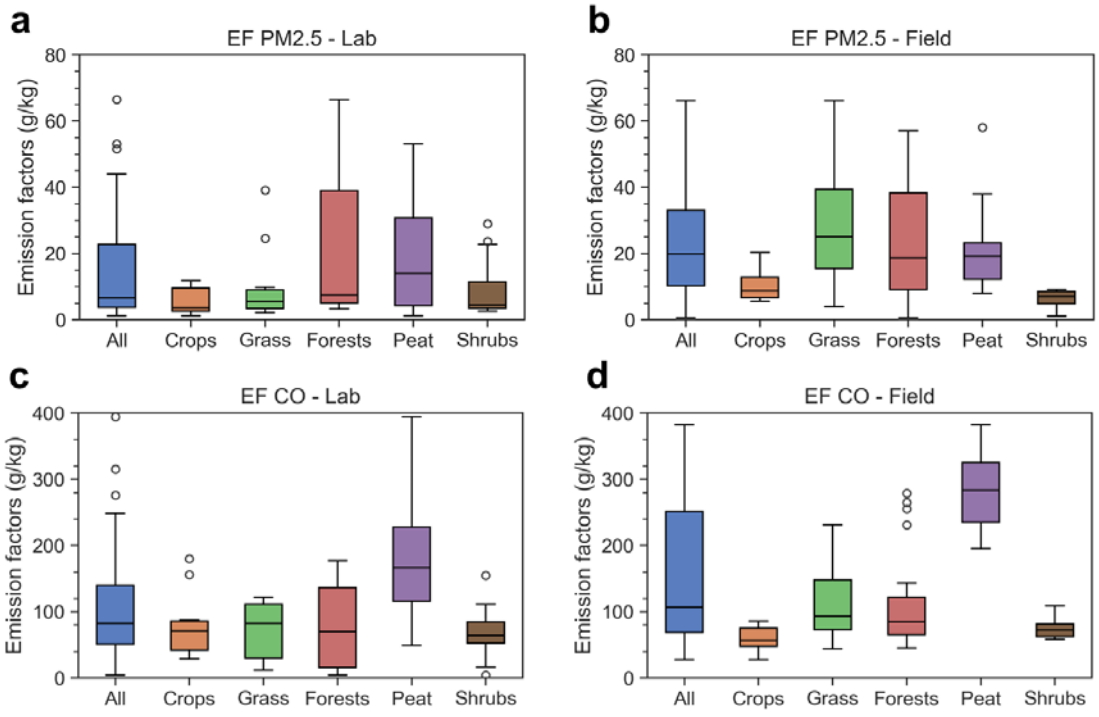

Fig. 2-8 Comparisons of emissions factors of $PM_{2.5}$ **(a-b)**, and CO **(c-d)** from various fuel sources in wildland fires.

Fig. 2-9b further compares $PM_{2.5}$ emissions from all types of fuels and combustion modes against the MCE. The findings indicate that $PM_{2.5}$ emissions are highly correlated with the completeness of fuel combustion, with a strong linear relationship between EF $PM_{2.5}$ and MCE. The relationship is described by $EF_{PM2.5} = -1166.3\ MCE + 1160$, with $R^2 = 0.9$.

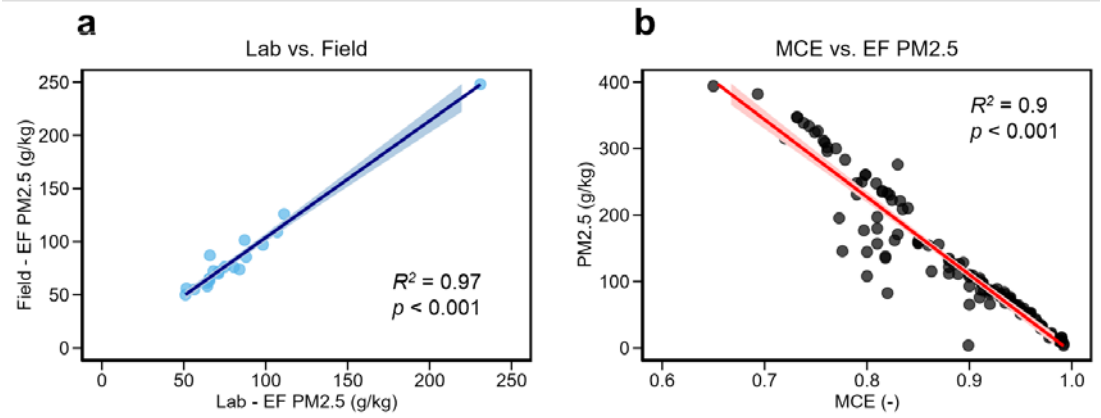

Fig. 2-9 Comparison of lab and field $PM_{2.5}$ emissions under similar MCE conditions (difference < 0.02), with the x and y axes corresponding to lab and field values, respectively ($EF_{PM2.5\_field}$ =1.1 $EF_{PM2.5\_lab}$ - 5.87) **(a)**. The emission factor of $PM_{2.5}$ demonstrates a strong linear relationship with modified combustion efficiency ($EF_{PM2.5}$ = -1166.3 MCE + 1160). Filled regions show the 95% confidence intervals **(b)**.

2.2.4 Satellite-based fire emission databases

Satellite observations are a reliable approach to monitoring and estimating fire emissions. In terms of *bottom-up* approach, satellite can estimate BA and fuel loads, therefore calculating the total fire emissions by EFs. Fire emissions can also be estimated by fire radiative energy measurement by satellite sensors, because the relationship between fire radiative energy and fuel mass combusted is linear and highly significant and Fire Radiative Power (FRP) is well related to combustion rate (Wooster *et al.* 2005). In addition, fire emissions can also be estimated by *top-down* methods that use the spaceborne light detection and ranging (LiDAR) to measure the biomass storage and biomass change (Xu *et al.* 2021; Liu and Popescu 2022).

Table 2-4 summarizes the current major fire emission databases, namely five bottom-up approaches based on Moderate Resolution Imaging Spectroradiometer (MODIS) BA,

fuel load, and emission factors from literature: GEFD4s (Giglio *et al.* 2013), and its updated version GEFD5 (Chen *et al.* 2023b), FINN (Fire INventory from National Centre for Atmospheric Research, U.S.) (Wiedinmyer *et al.* 2023), GFFEPS (Global Forest Fire Emissions Prediction System) (Anderson *et al.* 2024), one databases that based on FRP: GFAS (by European Centre for Medium-Range Weather Forecasts, ECMWF) (Kaiser *et al.* 2012), and two top-down databases, QFED (Quick Fire Emission Database) (Darmenov and Silva 2015) and FEER (Fire Energetics and Emission Research),(Ichoku and Ellison 2014) by NASA Goddard Space Flight Centre, which measure both FRP and Aerosol Optical Thickness (AOT). Two community models based on existing databases and statistic methods are included: FiTCH (Global fire emission dataset using the three-corner hat method) (Liu and Yang 2023) and FireMIP (Fire Modelling Intercomparison Project) (Li *et al.* 2019). This subsection introduced and compared the most representative products.

Table 2-4 Satellite-based fire emissions products.

Inventory	Full name	Approach	Based on	Resolution	Reference
GEFD4 (4.1s)	Global Fire Emission Database	Bottom-up	MODIS BA	daily, 0.25°	Giglio et al., (2013)
GEFD5	Global Fire Emission Database	Bottom-up	MODIS BA	monthly, 0.25°	Chen et al., (2023)
FINN2.5	Fire INventory from NCAR	Bottom-up	MODIS+VIIRS BA	daily, 1 km	Wiedinmyer et al., (2023)
GFAS1.2	Global Fire Assimilation System	Bottom-up	MODIS FRP	daily, 0.1°	Kaiser et al., (2012)
GFFEPS	Global Forest Fire Emissions Prediction System	Bottom-up	MODIS+VIIRS BA, and FWI + FBF	3-hour, 1 km	K. Anderson et at., (2024)
QFED2	Quick Fire Emission Database	Top-down	MODIS FRP and AOT	daily, 0.1°	Darmenov and da Silva, (2015)
FEER1	Fire Energetics and Emission Research	Top-down	MODIS FRP and AOT	daily, 0.1°	Ichoku and Ellison, (2014)
FiTCH	Global fire emission dataset using the three-corner hat method	Statistic	Existing databases	daily, 0.1°	Liu and Yang, (2023)
FireMIP	Fire Modelling Intercomparison Project	Multi-model merges	Existing databases	monthly, 1° historical from 1700	Li et al., (2019)

GFED is the earliest global BA dataset that use MODIS data to monitor the BA and Carnegie-Ames-Stanford Approach (CASA) Model to calculate fuel consumption, respectively.(Giglio *et al.* 2013; Chen *et al.* 2023b) The satellite BA data are merged with active fires from various sensors to monitor the small fires (GFED 4.1s). Furthermore, GFED5 fuses multiple streams of remote sensing data (including MODIS MCD64A1, Along-Track Scanning Radiometer (ATSR), and Visible Infrared Imaging Radiometer Suite (VIIRS) active fire data) to create a monthly BA dataset, which can estimate global BA that is 93% higher than MCD64A1 and 61% higher than GFED4.1s. However, due to robustness issues in higher resolutions, GFED5 is still on a 0.25-degree grid, and the small fires are detected by active fire data.

Fire Inventory from NCAR (FINN) is another widely used fire emission product which estimates emissions by multiplying BA with fuel consumption per unit BA, similar to GFED. However, the BA in FINN is estimated from actives and scalars factors, whereas GFED is based on mapped BA. The spatial resolution of FINN (1 km) is much higher than GFED (0.25-degree).

In addition to BA-based methods, global fire emissions are also estimated by fire power. One representative product is the GFAS, which assimilates FPR observations from the MODIS sensors onboard the Terra and Aqua satellites (Kaiser *et al.* 2012). The fire radiative power is linked to the dry matter combustion rates and aerosol emission rates, which were used to calculate the fire emissions. It can estimate forty species (including CO, CO_2, $PM_{2.5}$, etc.) by FRP and EFs from literature for five land cover classes (savannas, agriculture, tropical forest, peat, and extratropical forest)(Andreae 2001; Christian *et al.* 2003; Akagi *et al.* 2011).

2.2.5 Atmospheric chemistry modelling

The impact of wildfire emissions on human health constitutes a long-term process. Therefore, comprehending the evolution and transportation of smoke in the atmosphere is crucial for evaluating the health implications of fires. Meteorological conditions can influence the emission of chemical constituents into the atmosphere, as well as subsequent chemical reactions, transport, and removal processes (Zheng *et al.* 2015). Many atmospheric chemistry models have been developed to couple the regional meteorology

data (e.g., wind, temperature, and moisture) with emission inputs of source, girded, and inventory data.

One of the most widely used models is GEOS-Chem, a global 3-D model of atmospheric composition driven by assimilated meteorological observations from the Goddard Earth Observing System (GEOS) of the NASA Global Modelling and Assimilation Office (GMAO). Basically, it is driven by NASA GEOS meteorological data and simulates the evolution of atmospheric composition by solving the system of coupled continuity equations for an ensemble of *m* species (gases or aerosols) with the following concentration vector $\boldsymbol{n} = (n_1, \ldots, n_m)^T$ (Martin *et al.* 2022):

$$\frac{\partial n_i}{\partial t} = -\nabla \cdot (n_i \boldsymbol{U}) + P_i(\boldsymbol{n}) - L_i(\boldsymbol{n}) + E_i - D_i \qquad i \in [1, m]. \tag{2.13}$$

where $\boldsymbol{U}$ is the wind vector (including sub-grid components parameterized as boundary layer mixing and wet convection); $P_i(\boldsymbol{n})$ and $L_i(\boldsymbol{n})$ are the local production and loss rates of species *i* from chemistry and/or aerosol microphysics, which depend on the concentrations of other species; and E_i and D_i represent emissions and deposition.

Table 2-5 Atmospheric models for pollution chemistry transport modelling.

Model	Full name	Developer
GEOS-Chem	Goddard Earth Observing System-Chemistry transport model	Harvard University, Washington University
WRF-Chem	Weather Research & Forecasting coupled with Chemistry	NOAA/ESRL
CMAQ	Community Model for Air Quality	US EPA
CESM (CAM-Chem)	Community Earth System Model 2	NCAR
GEFS-Aerosol	Global Ensemble Forecast System - Aerosols	NOAA
UFS	Unified Forecast System	NOAA
CALPUFF	CALPUFF dispersion model	TRC

In addition, the GEOS-Chem High-Performance version (GCHP) is designed for multi-node massively parallel computation using a message-passing interface (MPI) distributed-memory parallelization in order to fulfil the requirement of flexibility and scalability for high-resolution applications.(Martin *et al.* 2022) WRF-GC model (Lin *et al.*

2020a; Feng *et al.* 2021) is integrated online with the Weather Research & Forecasting (WRF) meteorological model and GEOS-Chem model. It allows independent updates for two-parent models and massive parallel computation. Similar global and regional atmospheric simulation models include WRF-Chem, CESM2, GEFS-Aerosol, UFS model, etc (**Table 2-5**).

2.3 Health effects of wildfire emissions

$PM_{2.5}$ is always one of the primary hazardous emissions to human health and the focus of epidemiological investigations (McClure and Jaffe 2018; Aguilera *et al.* 2021). Concentration-response functions (CRF) is often used to estimate the premature mortality associated with short-term pollutant exposure, which is typically based on Relative Risk (RR, the relative exposure risk caused by a pollutant beyond the specified concentration, defined as the mortality rate ratio between exposed group and unexposed group) and Total excess risk (ER, the total excess risks of multiple pollutants) (Cairncross *et al.* 2007; Hu *et al.* 2015; WHO 2021).

$$RR = \exp(\beta(C - C_0)) \tag{2.14a}$$

where RR is described as an exponential relationship, C (mg/m^3) is the mass concentration of air pollutants, C_0 (mg/m^3) is the corresponding threshold concentration of air pollutants, $C > C_0$, and β is the exposure-response relationship coefficient, representing the excess risk of health effect (such as mortality) per unit increase of pollutant (e.g., 1 μg/m^3 of $PM_{2.5}$). For example, $RR = 1$ indicates that the pollution has no obvious adverse health effects. Note that Eq. 2.14a is not the only function of RR. For example, Eq. 2.14b uses a power-law form to fit the relationship between RR of lung cancer and cardiovascular disease and $PM_{2.5}$ exposure.(Arden Pope *et al.* 2011; Marlier *et al.* 2013)

$$RR = 1 + \alpha(dose)^{\beta} \tag{2.14b}$$

where α and β are fitting coefficients to be determined by cohort data, $dose = (I \times C)$, which estimates the inhaled $PM_{2.5}$ by multiplying the relevant average ambient $PM_{2.5}$ concentrations (C, mg/m^3) by average daily inhalation rates (I, m^3/day).

For multiple pollutants,

$$ER = \sum_{i=1}^{n} ER_i = \sum_{i=1}^{n} (RR_i - 1) \quad (2.15)$$

where ER reflects the total excess risks of multiple pollutants, and the excess risk ER_i caused by a specific air pollutant, i is equal to $(RR_i - 1)$. The higher the ER value is, the higher the health risk posed by air pollution, with a value of 0 indicating no risk.

To estimate the long-term exposure effect to $PM_{2.5}$ and the attributed burden of disease, the Integrated Exposure-Response (IER) model is proposed.(Burnett *et al.* 2014) It integrates RR information from various sources of $PM_{2.5}$ and developed functions for causes of mortality in adults: ischemic heart disease (IHD), cerebrovascular disease (stroke), chronic obstructive pulmonary disease (COPD), and lung cancer (LC). It allows a more accurate estimation of health risks from different combustion types, including very high $PM_{2.5}$ concentrations. It has been used to estimate the Global Burden of Disease (GBD) attributable to ambient air pollution (Cohen *et al.* 2017).

For example, the GEMM quantifies the relationship between long-term $PM_{2.5}$ exposure and excess relative risk (Burnett *et al.* 2018), which has been widely used by research organizations the World Health Organization (WHO), the World Bank, and the United States Environmental Protection Agency (EPA). It is based on cohort studies of outdoor air pollution, encompassing data from 41 cohorts across 16 countries, and then modelled the shape between $PM_{2.5}$ exposure and disease mortality. GEMM can predict higher excess deaths in low-concentration exposures than GBD risk functions.

The majority of previous epidemiological studies of fire impacts on health have focused on PM, while others have investigated the roles of O_3 (Chen *et al.* 2024) and PAHs (e.g., Benzo(a)pyrene) (Wu *et al.* 2022). Previous studies have investigated the time scale of short-term acute effects over days and months, the long-term chronic effects over years, as well as projections of future impacts (Lou *et al.* 2023). The spatial scale of these studies ranges from regional cohort studies to the application of cohort results to assess global impacts.

A cohort study in a nonurban area of North America revealed the acute influence (5-day lags) of exposure to peat fire smoke (Rappold *et al.* 2011). Significantly, RR increases

of 1.65 [95% CI 1.25-2.1] for asthma, 1.73 [1.06–2.83] for chronic obstructive pulmonary disease, and 1.59 [1.07–2.34] for pneumonia and acute bronchitis were observed. They found that asthma-related outcomes from fire smoke were most prevalent, particularly among adult women. They also observed smoke exposure leads to an increase in emergency department visits for heart failure and is associated with acute coronary syndrome. However, this study relied only on aerosol optical depth (AOD) data and did not account for specific toxic species in the smoke. Another cohort study in North America evaluates odd ratios (OR) of the short-term health impact of wildfire PM_{10} emissions (Henderson *et al.* 2011). Results indicate that for a 30 $\mu g/m^3$ increase in PM_{10}, ORs were 1.05 [1.03–1.06] for respiratory physician visits, 1.16 [1.0-1.23] for asthma-specific visits, and 1.15 [1.00-1.2] respiratory hospital admissions. Interestingly, the associations between wildfire PM_{10} and cardiovascular outcomes were essentially non-significant.

Short-term exposure effects to fire emissions on a regional or global scale have been investigated with CTMs. One study evaluated the acute health impacts of California wildfires from August to October, including the number of hospital admissions, work loss days, and mortality (Carreras-Sospedra *et al.* 2024). It estimates an additional 1,391 hospitalizations, 466 deaths, and 420,661 work loss days over just three months in California. The primary contributor was $PM_{2.5}$, while O_3 was responsible for only a few mortality cases. Another study, for the first time, systematically explored the health effects of short-term exposure to wildfire-related O_3 across 43 countries from 2000 to 2017 (Chen *et al.* 2024). Statistical evidence revealed that short-term exposure to wildfire-related O_3 is associated with all-cause and respiratory mortality, but not significantly associated with cardiovascular mortality (Chen *et al.* 2024). This may be due to the fact that acute effects often occur in the respiratory system (e.g., irritation and asthma), while cardiovascular diseases are typically chronic. Therefore, the effects of short-term exposure on the cardiovascular system are insignificant in this study. Projections of mortality due to short-term exposure to wildfire-related $PM_{2.5}$ in China from 2021 to 2100 have also been conducted (Lou *et al.* 2023). They estimated that deaths attributable to wildfires could reach the peak in 2021-40, with increases of 28.1% and 38.38% under optimistic and intermediate scenarios, respectively. Therefore, a stricter policy for wildfire management is urgently needed in China.

Long-term exposure studies focus on the chronic or cumulative effects of exposure over months to years to fire smoke. Typically, annual-average exposure to wildfire-related smoke is estimated at a regional scale, (e.g., south-east Asia (Kiely *et al.* 2020), Africa (Wu *et al.* 2022), and South America (Nawaz and Henze 2020)) or on a global scale (Johnston *et al.* 2012; Roberts and Wooster 2021). Similar to studies on short-term impacts, $PM_{2.5}$ remains the most concerning emission from fires, while some research also focuses on the other persistent organic pollutions (e.g., PAH (Wu *et al.* 2022)) that undergo long-term range atmospheric transport. Premature death estimates vary across studies. For example, one global-scale study estimated that annual deaths due to landscape fire smoke exposure between 1997 and 2006 were approximately 339,000 (Johnston *et al.* 2012), which is much lower compared to 800,000 deaths from urban air pollution (Cohen *et al.* 2005) and 1,600,000 associated with household solid fuel use (Lopez 2006). Notably, the global burden during El Niño years (1997-1998) was twice that of La Niña years (1999-2000), with Southeast Asia being the most vulnerable region, experiencing nearly seven times the impact during El Niño periods (Johnston *et al.* 2012). A similar study has a higher estimate of global premature death of 677,745 during 2016-2019 (Roberts and Wooster 2021). The uncertainties are raised from (1) methods in emission estimate and transport prediction and (2) different CRF functions that are used to relate the health risk and smoke exposures. This work also highlighted that 44 million people are exposed to unhealthy air annually, and 39% are children under 5 years among global fire-attributed premature deaths (Roberts and Wooster 2021).

Fig. 2-10 compares the total number of excess deaths caused by wildfires on a global scale, as estimated using epidemiological models (Johnston *et al.* 2012; Roberts and Wooster 2021), with deaths associated with modifiable risk factors from WHO GBD 2021 report (Brauer *et al.* 2024). The results show that wildfire smoke exposure is a significant contributor to global mortality, with estimates comparable to those for factors like high BMI (body-mass index), occupational risks, and high alcohol use. However, due to the outdated epidemiological models and satellite-derived emission products used in the estimates, as well as the relatively short time scale of the study, there is an urgent need for more systematic research. This should involve the application of the latest and most accurate emission estimates and epidemiological models over longer time scales to better assess global mortality due to wildfire smoke exposure.

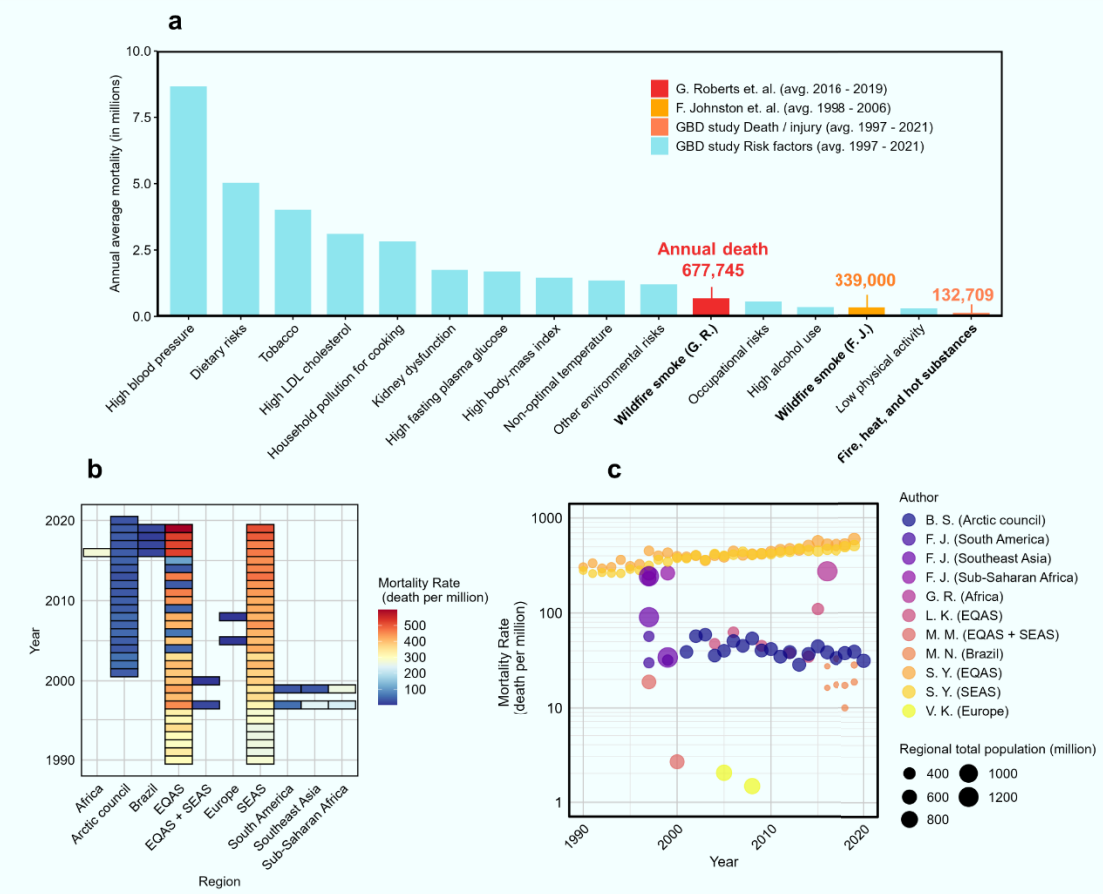

Fig. 2-10 Estimate of global burden of death due to fire smoke exposure (red and orange bars),(Johnston *et al.* 2012; Roberts and Wooster 2021) compared with modifiable risk factors caused cardiovascular diseases and chronic respiratory diseases (blue bars), as well as direct death from fire, heat, and substances (pink bar) assessed by the Global Burden of Disease (GBD) 2021.(Brauer *et al.* 2024) The definition of each risk factor can be found from Institute for Health Metrics and Evaluation (IHME) and GBD. Figure adapted from references(Ezzati *et al.* 2002; Johnston *et al.* 2012) **(a)**. Heatmap **(b)**, and scatter plot **(c)** in logarithmic scale of regional estimates of death due to fire smoke exposure, the mortality rate (estimated death per million people) is calculated by estimated premature death and regional total population from World Bank.

Moreover, **Fig. 2-10** also compares the annual average mortality rates due to wildfire smoke exposure across time and spatial scales in different studies, expressed as the number of excess deaths estimated by the models divided by the total population of the region in that year. Although there are currently few comparable studies, the overall trend shows

an increase in wildfire-related deaths worldwide from 1990 to 2020. Notably, the estimated mortality rate for Southeast Asia is significantly higher than in other regions. An important reason is the higher wildfire risk near the equator, and the persistent smouldering peat fire in Indonesia and Malaysia are burning at deep layers and extremely difficult to extinguish (Qin *et al.* 2022a), continuously contributing to PM emissions. Additionally, the studies using the latest emission and epidemiological database indicate a higher value. Future studies on a global scale are needed to better quantify the transboundary health impacts of regional wildfire smoke exposure.

CHAPTER 3 Methodology

3.1 Lab experiments

3.1.1 Fuel samples

In this study, commercially available moss peat was selected as the test fuel to ensure homogeneity and reproducibility under controlled combustion conditions. While we acknowledge that tropical peat differs in organic composition, ash content, and pore structure, the use of commercial peat allows for a more systematic investigation of the relationships between combustion conditions and emission characteristics. This peat had a high organic content (OC~97%), a uniform density (128 ± 10 kg/m^3), and a homogenous particle size (Φ_p = 0.90 ± 0.01), thus ensuring high repeatability of experiments. EA shows that its mass fraction of C/H/O/N/S is 45.6/6.0/48.0/0.5/0.3%, respectively. Before the tests, the peat soil was first dried in an oven at 75 ºC for 48 h (Huang and Rein, 2017). The dried peat was stored in the ambient, so it absorbed air moisture and eventually reached a new equilibrium with a low MC of ~10%, defined as air-dried peat.

To investigate the moisture effect, the dry peat was well mixed with water and left in sealed boxes for homogenisation for at least 48 h. Note that the peat sample volume naturally expanded during water absorption, which was also observed in our previous works (Huang and Rein 2017; Lin *et al.* 2019). The TGA of the peat sample was conducted with a PerkinElmer STA 6000 in both air and nitrogen atmospheres, and the representative data are shown in **Fig. 3-1**. The chemical properties of the peat sample are also summarised in **Table 3-1**.

Table 3-1 Properties of dried peat used in the experiments.

Bulk density (kg/m^3)	Dried moisture (%)	Volatile content (%)	Ash content (%)	Fixed carbon (%)	Heat of combustion (MJ/kg)	C (%)	H (%)	O (%)	C/O (-)	H/O (-)
127.8±10	<10	72.0	3.5	24.5	13.1	46.1	5.8	47.5	0.97	0.12

Fig. 3-1 shows the thermogravimetric results using PerkinElmer STA6000 under five oxygen concentrations by mixing air and N_2: 21% (air), 10%, 5%, 2% and 0% (N_2). In this study, it exposes 2-3 mg samples to a temperature ramp of 30 °C/min from room temperature to 800 °C. For each scenario, tests were repeated at least twice to ensure good

experimental repeatability.

The peat sample used in **Chapter 4** was first pulverised into powders and dried at 90 °C for 48 h. The initial mass was around 2-3 mg, and the sample was heated at a relatively low heating rate of 10 K/min. **Fig. 3-1** shows the remaining mass fraction and mass-loss rate curves of this peat. As expected, the mass-loss rate rapidly increases at about 250 °C, which could be defined as the pyrolysis temperature.

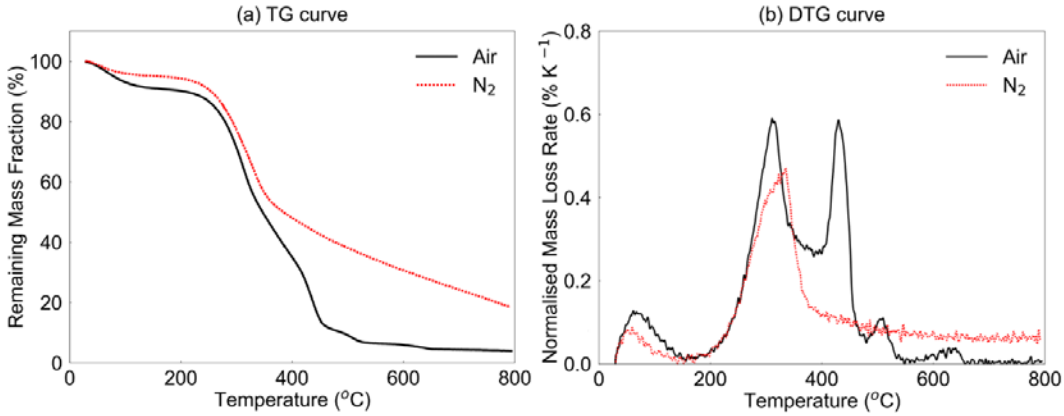

Fig. 3-1 TGA results of the peat sample at a heating rate of 10 K/min.

Fig. 3-2 shows the derivative thermogravimetric (DTG) curves of organic peat soils against the temperatures in different test scenarios in **Chapter 5**. For all tests, the first mass loss stage below 200 °C is mainly due to the dehydration process, which accounts for less than 10% of the total mass loss. Basically, except for the drying stage at the temperature below 100 °C, there were two curve peaks with fast mass loss. One peak represents the pyrolysis process, at around 270 °C where the mass loss rate rises rapidly. In this process, peat samples absorbed heat and decomposed into pyrolysis gases and char. It showed that the pyrolysis temperatures of the samples under different oxygen conditions were very close. However, the peak mass loss rate increased as the oxygen concentration increases. It indicated that some oxidation process should also exist in this temperature (~ 320 °C) whose reaction rate increases with the oxygen concentration. With the temperature rising, the fuel was gradually decomposed, and then, oxidation turns into the main reaction causing the mass loss. It is worth noting that oxidation reaction was observed at any oxygen concentration (excluding N_2 without any oxygen) in this study. That is, smouldering can occur under extremely low oxygen concentration (below 2%). From **Fig. 3-2a**, we can also see that reducing the oxygen concentration does not affect

the final total mass loss unless all oxygen was removed (i.e., pure N_2 environment). Nevertheless, a lower oxygen concentration will significantly slow down the rates of oxidation and smouldering propagation.

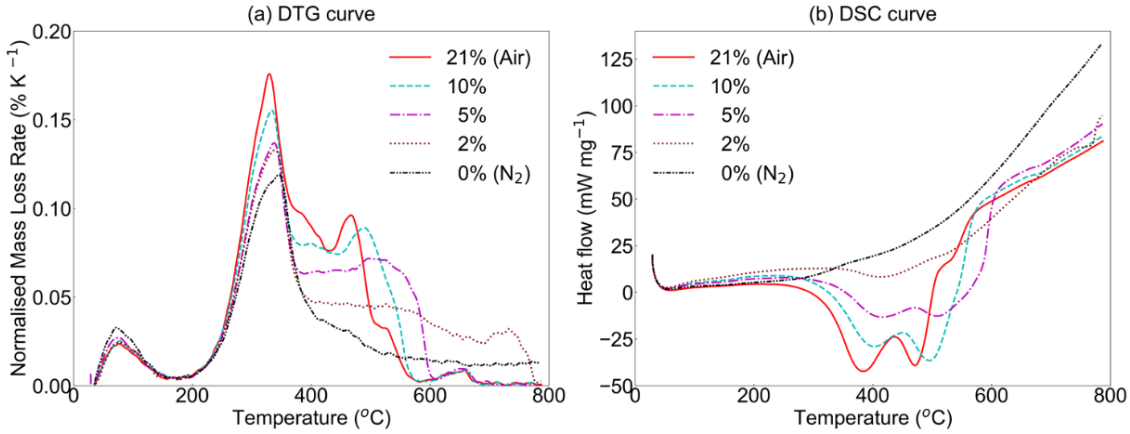

Fig. 3-2 DTG **(a)** and DSC **(b)** curves of peat in various oxygen volume fractions.

Fig. 3-2b shows the amount of heat required to increase the temperature of the sample, which provides a reference for the temperature reaction that occurs, and the heat released. Basically, decreasing the oxygen concentration increases the temperature required for the reaction and decreases the peak exothermic rate of the reaction. The total smouldering heat of the whole temperature range (up to 800 °C) was calculated to be almost constant (about 12.6 MJ/kg). Nevertheless, if the maximum smouldering temperature is lower, the released heat of smouldering will be smaller.

3.1.2 Experimental setup

Fig. 3-3 presents the schematic of the experimental setup. To better study and observe the in-depth peat fire, the height of the test setup was 100 cm, which is the largest laboratory apparatus used for smouldering study. The 1 m peat column was selected as a practical compromise to simulate prolonged smoldering while ensuring experimental feasibility. Although this setup does not fully capture the maximum burning depths observed in natural peatlands, it exhibits pronounced vertical gradients in both temperature and oxygen availability, which are key characteristics of underground smouldering. Due to limitations in in-situ measurement instrumentation, pressure gradients were not directly quantified in this study. However, we are currently developing large-scale numerical models to further investigate the role of pressure-driven oxygen transport in deep smouldering scenarios. The test setup was built of 1 cm-thick insulation ceramic fibreboards

due to its low conductivity and non-flammability (Christensen *et al.* 2019). Similar setups of smaller sizes had been widely used for past lab-scale peat fire experiments (Benscoter *et al.* 2011; Huang *et al.* 2016; Prat-Guitart *et al.* 2016a; Huang and Rein 2017, 2019; Depci and Karta 2018; Lin *et al.* 2021a). Two layers of aluminium foil were attached to the outer surface of the insulation board to seal the reactor and reduce the radiative heat loss due to its lower emissivity (Incropera 2007). The test setup had a large internal cross-section of 24 cm × 24 cm to avoid quenching by the cold wall (Lin and Huang 2021). Together with the ceramic insulation and aluminium foil, the wall cooling was minimised and similar to field condition. However, the use of ceramic fibreboard makes it impossible for the infrared camera to capture the evolution and propagation of the smouldering front from the side view.

To limit the conductive cooling effect through inserted thermocouples on the smouldering temperature and reactions, thus the spacing and number of thermocouples should be carefully optimised. Therefore, on the assumption of 1-D smouldering propagation, an array of K-type thermocouples with a bead diameter of 1.5 mm was inserted into the reactor from the side wall at an interval of 6 cm to record the temperature and capture the location of fires. The coil ignitor was inserted into the sample to initiate the smouldering combustion. A Testo 340 real-time emission sensor was installed 5 cm above the top free surface to measure the CO emission during the smouldering process. Because of the slow fire propagation and persistence of the burning process, the time interval for recording the in-depth temperature profile and the emission of deep peat fire was set to once per minute.

A 20 cm coil heater was embedded in the peat layers for ignition. In order to initiate the combustion and form a robust smouldering front, the ignition protocol was set to 200 W for 60 min, which was sufficient to ignite a uniform smouldering fire in wet peat samples (MC < 150%) (Huang and Rein 2017). The successful ignitions were verified by thermocouple measurement at the ignition stage. By placing the coil ignitor at different heights at an interval of 20 cm from the top free surface (0 cm) to the bottom (-100 cm), the smouldering front can be formed at different depths and free to propagate vertically. The tests are stopped until all peat has returned to room temperature after 12 hours. For each scenario, tests were repeated at least twice. With the decreasing ignition position, if

different fire propagation modes were observed, three or four repeated tests were conducted to ensure repeatability. Our results show excellent repeatability because of the use of commercial peat soil with uniform density, particle size and organic content (Lin *et al.* 2021b).

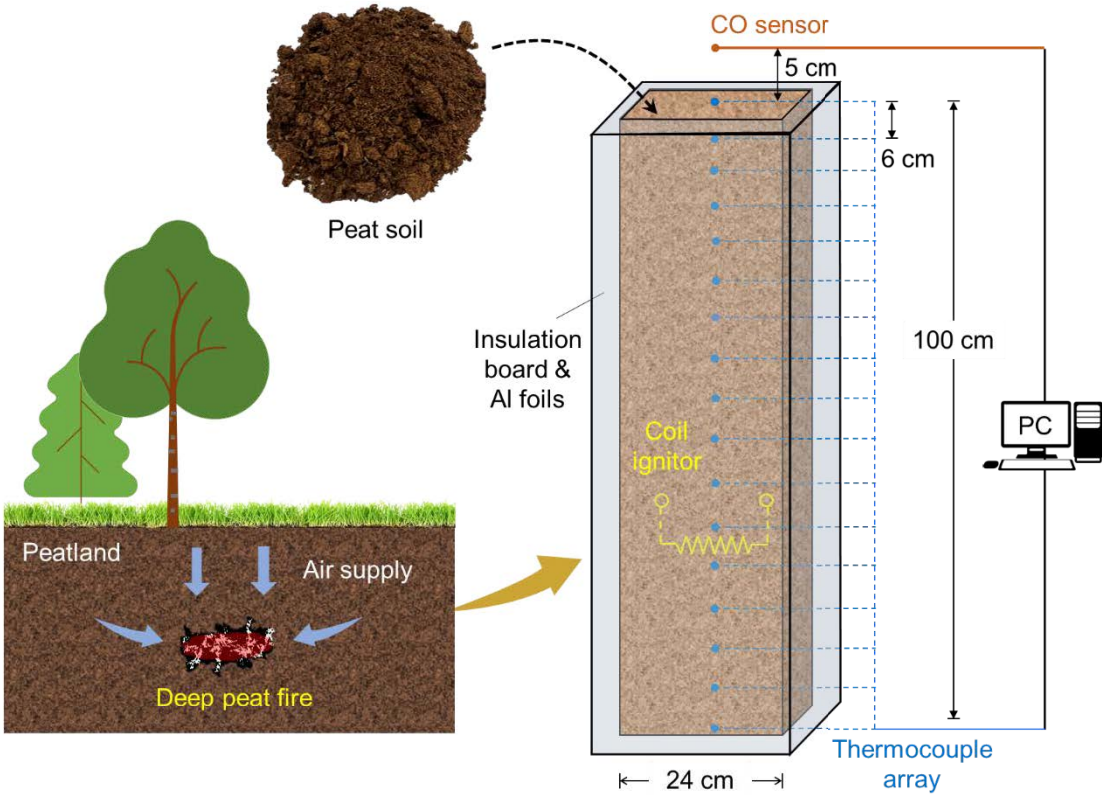

Fig. 3-3 Experimental setup for in-depth smouldering peat fire.

Because of no forced flow is provided in this demonstration, the oxygen supply was mainly from the top open surface. There might be tiny gas leakages from the holes that were used to insert the thermocouples, which could be detected. Nevertheless, in real peat fire scenarios, the oxygen can also infiltrate and diffuse to the smouldering zone from the side. Therefore, such weak lateral gas leakages may make the laboratory tests closer to the actual peat fire in the field.

Previous small-scale experiment is designed in quiescent ambient of external wind, which is difficult to quantify the actual amount of oxygen that feed to smouldering front. To address this, a novel combustion reactor that provide internal forced flow was designed. The schematic diagram of experimental setups which mainly consisted of a disclosed tubular smouldering reactor, an ignition system, and an oxidiser supply system, is

shown in **Fig. 3-4**. The smouldering reactor was made of 2-mm thick quartz glass with a depth of 30 cm. The internal diameter of the reactor was designed to be 12 cm to minimise the quenching effect from the reactor wall (Lin and Huang 2021; Lin *et al.* 2022a). Meanwhile, a 1-cm thick ceramic insulation layer was attached to the surface of the reactor to further reduce the environmental heat losses. To homogenise the flow from the bottom, a steel mesh was placed 3 cm above the bottom of the reactor, and a 5-cm thick layer of glass beads was poured above the steel mesh. Then, a fresh fuel sample with a constant height of 20 cm was placed on the glass beads.

An array of five K-type thermocouples (1 mm bead diameter) was inserted into the fuel with an interval of 5 cm, recording the temperature profiles with a time interval of 1 min. The ignition source was a heating coil placed at the middle of apparatus, fixed at 100 W for 15 min. A forced oxidiser flow was supplied from the bottom end of the reactor, and the flow rate was controlled by a flow meter with an uncertainty of 5%. A gas outlet with a diameter narrowed to 1 cm was designed on the top of the reactor to allow the injection of emission gas and prevent the atmospheric oxygen from entering the reacting sample. Therefore, the oxygen supply to the smouldering front only came from the forced oxidiser flow on the bottom.

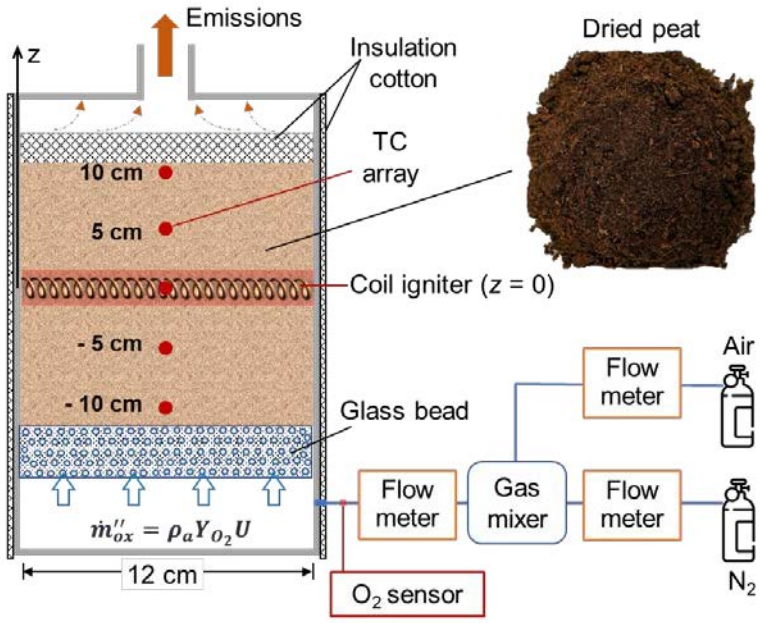

Fig. 3-4 Schematic diagram of experimental setup and photo of tested organic peat soil sample.

3.1.3 Test procedure and controlled parameters

The ignition protocol was set at 100 W for 15 min, sufficient to ignite dry peat and initiate robust smouldering combustion under atmospheric conditions. Afterward, a 1-cm layer of insulation cotton was put on the fuel surface to prevent heat loss and flying ashes. Then, the oxidiser flow with a prescribed X_{O_2} and flow velocity (U) was fed from the bottom of the reactor. Herein, the oxygen supply rate was defined by the mass flux of oxygen through the cross-section of the reactor as:

$$\dot{m}''_{ox} = \rho_g Y_{O_2} U \tag{3.1}$$

where U is an overall value for the cross-section of the reactor rather than a local velocity in pores; ρ_g is the air density; $Y_{O_2}$is the oxygen mass fraction. The relationship between X_{O_2} and Y_{O_2} is given as:

$$X_{O_2} = \rho_g \frac{Y_{O_2}}{\rho_{O_2}} \tag{3.2}$$

The test started with normal airflow (X_{O_2}= 21%). If the smouldering propagation can self-sustain after ignition, the flow velocity was decreased for another individual case. By following this procedure of gradually decreasing flow velocity for each individual combustion case, the minimum flow velocity (U_{min}) could be determined. Subsequently, the value of X_{O_2} was reduced to conduct tests with fresh samples and find the relationship between X_{O_2} and U_{min}. In this work, the oxygen concentration changes from 21% to 2%, and the flow velocity changes from 0.1 mm/s to 14.7 mm/s. During the experiments, the ambient temperature was 22 ± 2 ºC, the humidity was 50 ± 10%, and the pressure was 101 kPa. For each scenario, at least two repeating tests were conducted to ensure repeatability.

3.2 Numerical simulations

3.2.1 Governing equations

The 1-D computational model solved the transient conservation equations for condensed and gaseous phases in the absence of gravity, since the gravity and buoyancy effect inside the porous media of such a small fuel sample played a negligible role (Huang and Rein 2016a; Lin et al. 2022a). The governing conservation equations were provided here, including the conservation of (3.3) mass, (3.4) species, and (3.5) energy in the condensed phase, as well as the conservation of (3.6) mass, (3.7) species, and (3.8) momentum (Darcy's law) in the gas phase. All symbols were explained in the Nomenclature, and more details can be found in Gpyro technical reference (Lautenberger 2014). This model also assumed the thermal equilibrium between gas and condensed-phase species (i.e., local gas and solid species have the same temperature), unit Schmidt number, and the same gas diffusion coefficient and specific heat for all gas species. For simplification, the air was assumed to have a constant ρ_g = 1.161 kg/m^3, regardless of the oxygen mass fraction (Y_{O_2}) or gas temperature (T_g). The effect of sample shrinkage is not included in this model, since it plays a negligible role in the limiting oxygen supply for smouldering combustion. More details of the mathematical form of these equations can be found in (Lautenberger and Fernandez-Pello 2009).

$$\frac{\partial \bar{\rho}}{\partial t} = -\dot{\omega}_{fg}^{'''} \tag{3.3}$$

$$\frac{\partial (\bar{\rho} Y_i)}{\partial t} = \dot{\omega}_{fi}^{'''} - \dot{\omega}_{di}^{'''} \tag{3.4}$$

$$\frac{\partial (\bar{\rho}\bar{h})}{\partial t} + \frac{\partial (\dot{m}^{''}\bar{h}_g)}{\partial z} = \frac{\partial}{\partial z}\left(k\frac{\partial T}{\partial z}\right) + \sum \dot{\omega}_{di,k}^{'''} \Delta H_k \tag{3.5}$$

$$\frac{\partial (\rho_g \bar{\psi})}{\partial t} + \frac{\partial \dot{m}^{''}}{\partial z} = \dot{\omega}_{fg}^{'''} \tag{3.6}$$

$$\frac{\partial (\rho_g \bar{\psi} Y_j)}{\partial t} + \frac{\partial (\dot{m}^{''} Y_j)}{\partial z} = -\frac{\partial}{\partial z}\left(\rho_g \bar{\psi} D \frac{\partial Y_j}{\partial z}\right) + (\dot{\omega}_{fj}^{'''} - \dot{\omega}_{dj}^{'''}) \tag{3.7}$$

$$\dot{m}'' = -\frac{\bar{K}}{\nu}\frac{\partial \bar{p}}{\partial z} \quad (\rho_g = \frac{P\bar{M}}{RT}) \tag{3.8}$$

3.2.2 Smouldering chemical kinetics

The heterogeneous chemistry of the pyrolysis and oxidation of pine needles was modelled using a 5-step kinetic scheme with three major components: hemicellulose, cellulose, and lignin (Rana et al. 2023). The 5-steps included (3.9) drying [dr]; (3.10-3.12) pyrolysis of hemicellulose, cellulose, and lignin (the typical temperature at ~250 °C, ~300 °C, and ~350 oC, respectively) [hp], [cp], [lp]; (3.13) char oxidation [co], expressed as:

$$Water \rightarrow Water\ vapor\ [dr] \tag{3.9}$$

$$Hemicellulose \rightarrow Char + Pyrolyzates\ [hp] \tag{3.10}$$

$$Cellulose \rightarrow Char + Pyrolyzates\ [cp] \tag{3.11}$$

$$Lignin \rightarrow Char + Pyrolyzates\ [lp] \tag{3.12}$$

$$Char\ +\ O_2 \rightarrow Ash + gas\ [co] \tag{3.13}$$

The normalized destruction rate of condensed-phase species A in reaction k follows the Arrhenius law:

$$\dot{\omega}_k^* = Z_k \exp\left(-\frac{E_k}{RT}\right) f(m_A^*) g(Y_{O_2}) \tag{3.14}$$

where Z_k is the pre-exponential factor, and E_k is the activation energy. The mass action function for reactant A:

$$f(m_A^*) = (m_A^*)^{n_k} = \left(\frac{m_A}{m_{sA,0}}\right)^{n_k} \tag{3.15}$$

where $m_{sA,0}$ is the original mass of the species A, and n_k is the reaction order. The oxidation model considers oxidative pyrolysis as

$$g(Y_{O_2}) = \begin{cases} 1 & (n_{k,O_2} = 0) \\ (1 + Y_{O_2})^{n_{k,O_2}} - 1 & (n_{k,O_2} \neq 0) \end{cases} \tag{3.16}$$

Physical properties of all condensed-phase species were obtained from (Lin et al. 2022b) and listed in **Table 3-2**, where the subscript *s* and *o* represents the solid physical properties (i.e., $\psi = 0$) and bulk physical properties, respectively. It is worth noting that compared to fuels with fine particle sizes such as wood dust, pine needle fuel may be more heterogeneously and unevenly distributed in real scenarios. However, this model does not consider such factors and treats pine needles as uniform porous media. Therefore, the effective thermal conductivity in porous media included the radiation heat transfer across pores as

$$k_i = k_{s,i}(1 - \psi_i) + \gamma_i \sigma T^3 \tag{3.17}$$

where γ is dependent on the pore size (d_p) as $\gamma \sim d_p = 1/S\rho$. The permeability ($K \sim {d_p}^2$) of all solid species: hemicellulose, cellulose, lignin, char, and ash, was assumed to be independent and estimated on the scale of 10^{-12}~10^{-10} (Huang and Rein 2016b). The averaged properties of condensed-phase species in each cell were calculated using mass- or volume-weighted fractions:

$$\bar{\rho} = \sum X_i \rho_i \,, \bar{k} = \sum X_i k_i \,, \bar{c} = \sum Y_i c_i \,, X_i = \bar{\rho} \frac{Y_i}{\rho_i} \tag{3.18}$$

The kinetic and stoichiometric parameters of the 5-step reactions were also obtained from (Lin et al. 2022b) (**Table 3-3)**.

Table 3-2 The physical parameters of condensed-phase species

Species (*i*)	Y_0 (-)	$\rho_{s,i}$ (kg/m^3)	$\rho_{o,i}$ (kg/m^3)	$k_{s,i}$ (W/m·K)	$c_{p,i}$ (J/kg·K)
Water	0.05	1000	1000	0.6	4186
Hemicellulose	0.2	782	150	0.2	1500
Cellulose	0.5	694	150	0.2	1500
Lignin	0.25	454	150	0.2	1500
Char	0	500	100	0.05	3000
Ash	0	150	15	0.1	3000

Table 3-3 Chemical kinetic parameters of 5-step reaction for pine needles

Parameter	*dr*	*hp*	*cp*	*lp*	*co*
$lgZ_k(\mathbf{lg(s^{-1})})$	8.12	8.2	12.4	14.7	11.9
E_k **(kJ/mol)**	67.8	106	160	236	184
$n_k(-)$	3	1.49	0.95	8.7	1.27
$n_{k,O_2}(-)$	0.252	454	150	0.2	1500
$\nu_{B,k}$**(kg/kg)**	0	0.24	0.27	0.40	0.06
ΔH_k **(MJ/kg)**	2.26	0.2	0.5	0.5	-20
$\nu_{O_2,k}$**(kg/kg)**	0	0.5	0.5	0.5	1.5

The initial temperature of the fuel was set to 300 K. To simulate the dried pine needles in the experiments, the MC of fuel was assumed to be 5%, and the component ratio of was 0.209 (hemicellulose): 0.529 (cellulose): 0.262 (lignin) (Lin et al. 2022b). The heat transfer coefficient of $h_c = 10\ W/m^2K$ was applied to represent environmental cooling from top and bottom layer, and the emissivity of biomass was set to 0.95. The specific heat capacity (c_g) was assumed to be 1100 J/kg·K for all gas species (Lautenberger and Fernandez-Pello 2009). A forced oxidizer flow was applied from the bottom of the computational domain. To initiate smouldering, a heat flux of 30 kW/m^2 was applied on the top of fuel for the first 5 minutes. A successful smouldering propagation was defined if the smouldering front can gradually propagate downwards and reach the bottom without any discernible deceleration of propagation or decrease in temperature (Lin and Huang 2021). To eliminate the influence of inadequate heating on unsuccessful ignition, if no smouldering propagation occurred, the ignition protocol would be progressively enhanced to be 50 kW/m^2 for 30 minutes. The ambient pressure and temperature were assumed to be 1 atm. and 300 K. The solution started to converge at ΔZ = 0.1 mm and Δt = 0.01 s. Further reducing the cell size and time step by a factor of two gave no significantly different results, so the calculation was sufficiently resolved.

3.2.3 Model validation with experimental data

Although we have experimentally determined the oxygen-supply limits for peat, these

data are difficult to use for model validation because they address only one property and peat's pore size and dry-bulk density are hard to vary. Therefore, pine needles (see photo in **Fig. 3-5**) were used as representative porous media in this work, and they were collected from the larch forest in Saihanwula Biosphere Reserve, China. The natural pine needle bed had a highly porous structure (ψ = 0.9 ± 0.02), and the thermogravimetric analysis test showed an organic content of > 80% and a mineral content of about 15%. All pine needles were pre-dried in ovens at 75 ºC for at least 48 h, and the MC was controlled below 5%, which was demonstrated to have a negligible effect on smouldering propagation (Huang and Rein 2015). By compressing the fuel bed, ρ_b ranging from 50 ± 10 to 150 ± 30 kg/m^3 were achieved.

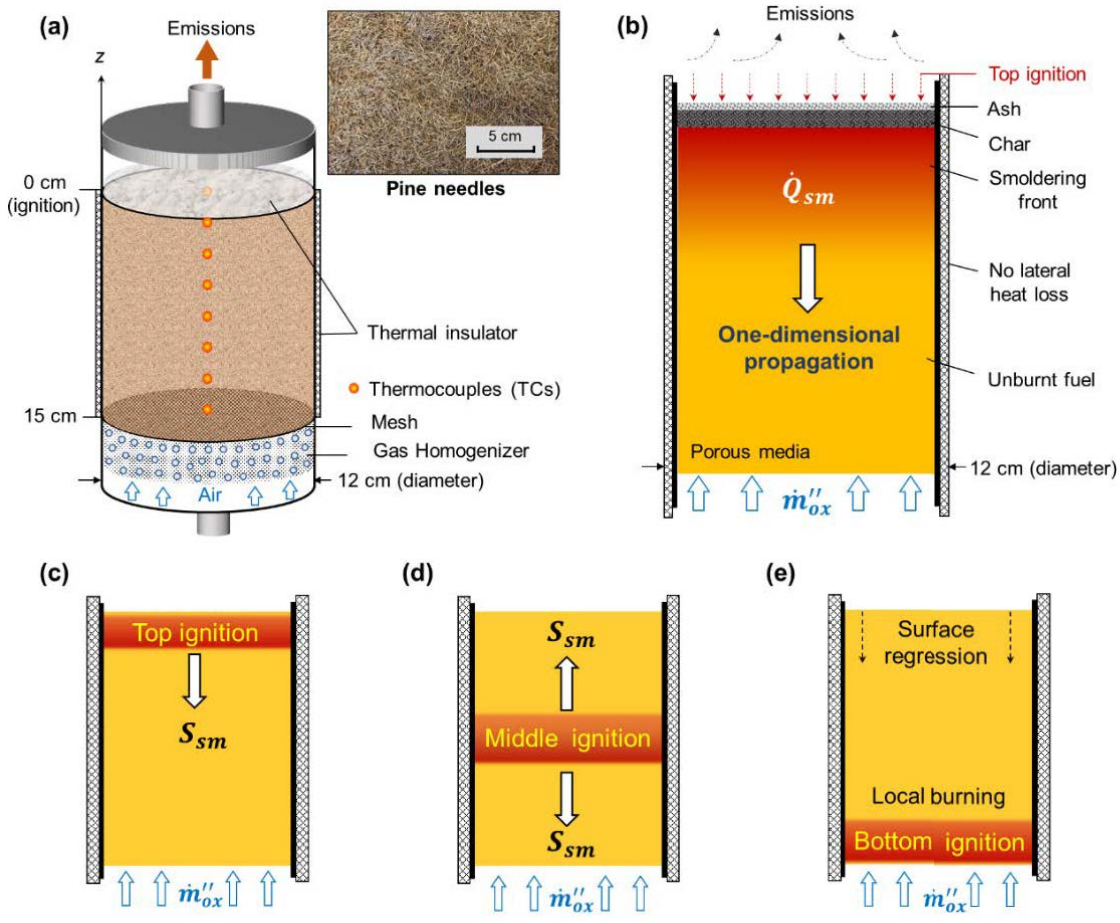

Fig. 3-5 Experimental setup to explore the oxygen supply thresholds (or smothering limits) of smouldering combustion, where pine needles were selected as representative porous fuel **(a)**; schematic diagram of the one-dimensional smouldering model **(b)**; common ignition locations (top, middle, and bottom ignition protocol) used in the studies of in vertical smouldering propagation **(c-e)**.

For all tests, as the lateral heat loss was minimized to a negligible level, and ignition was applied throughout the entire cross-area surface, the whole vertical smouldering spread can be approximated as a one-dimensional spread process (Qin et al. 2022b). Therefore, a one-dimensional computational model with the 20 cm sample depth (same as the experiment, refer to **Fig. 3-5a**) was established using Gpyro v0.7 (Lautenberger and Fernandez-Pello 2009). Gpyro is an open-source code for combustible solids, used to simulate pyrolysis and smouldering in porous media like peat (Lin et al. 2022a), wood (Richter et al. 2021), PU foam (Lautenberger and Fernandez-Pello 2009), and coal (Yuan et al. 2019). Initially, the simulation was started with an excessive oxygen supply. If smouldering can propagate successfully under these conditions, subsequent tests were conducted with reduced oxygen flow rates. Ultimately, the limiting oxygen supply rate will be obtained, below which smouldering cannot be sustained. Following this, oxygen concentrations can be adjusted by changing the ratio of N_2 to O_2, enabling further investigations into the minimum oxygen supply rate under different oxygen concentrations.

3.3 Machine learning predictions

3.3.1 Artificial neural network

The artificial neural network (ANN) is a deep-sequencing data processing model capable of learning from prior events to identify patterns and generate desired outcomes (Zou et al. 2009). To improve the generalizability of experimental results and enable predictive applications, an ANN model was developed to learn the relationship between peat combustion conditions and fire emissions. This model aims to bridge laboratory-scale measurements and large-scale emission estimations. The ANN will be further applied in Chapter 7 to estimate in-situ peat combustion emissions under realistic field scenarios, and in Chapter 8 to support health impact assessments via atmospheric transport modeling. This study employs a backpropagation neural network model. It is a multi-layer feedforward model trained using the error backpropagation algorithm. As illustrated in **Fig. 3-6**, the input layer incorporates fuel type, density, combustion mode, test scale, thermal conditions, and oxygen supply. The output layer predicts EFs of three fire emissions: CO, CO_2 and TPM.

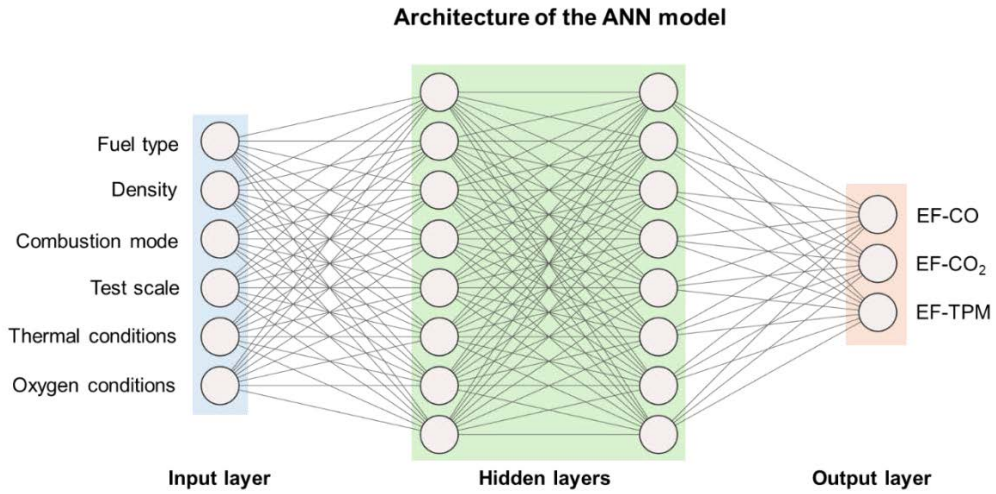

Fig. 3-6 Illustration of the proposed ANN model.

For each perceptron shown in **Fig. 3-6**, the output prediction is based on Eq. 3.19

$$Out_j = h\left(\sum_{i=1}^{N} W_{ji}X_i + B_j\right) \tag{3.19}$$

where X_i represents the input from the preceding layer neuron, W_{ji} is the corresponding weight of X_i, B_j is the bias, and h is the activation function. Various activation functions exist, including sigmoid, ReLU, tanh, and tansig. In this study, the ReLU function was employed as the transfer function between layers.

The ANN model in this study was implemented using the open-source Python library Scikit-Learn. **Fig. 3-7** illustrates the training process of the WUI-EF model. First, the database was normalized and randomly divided into an 80% training set and a 20% test set. The optimal hyperparameters are then selected through a trial-and-error approach within the training set using *k-fold* cross-validation, given the database's limited size. Cross-validation was employed to mitigate overfitting and serves as a resampling method for evaluating models with constrained data inputs.

In *k-fold* cross-validation, the dataset was randomly partitioned into *k* (5 in this work) equally sized folds. Each time, one-fold was used as the validation set, while the remaining *k-1* folds are used to train the model. This process was repeated k times, ensuring that

each fold was used for validation once. A root-mean-squared error (RMSE) was calculated for each iteration, and the average RMSE across all k iterations was computed. Finally, the hyperparameters yielding the lowest average RMSE are selected. The model was then retrained using the entire training dataset with the optimal hyperparameters and evaluated on the 20% test data.

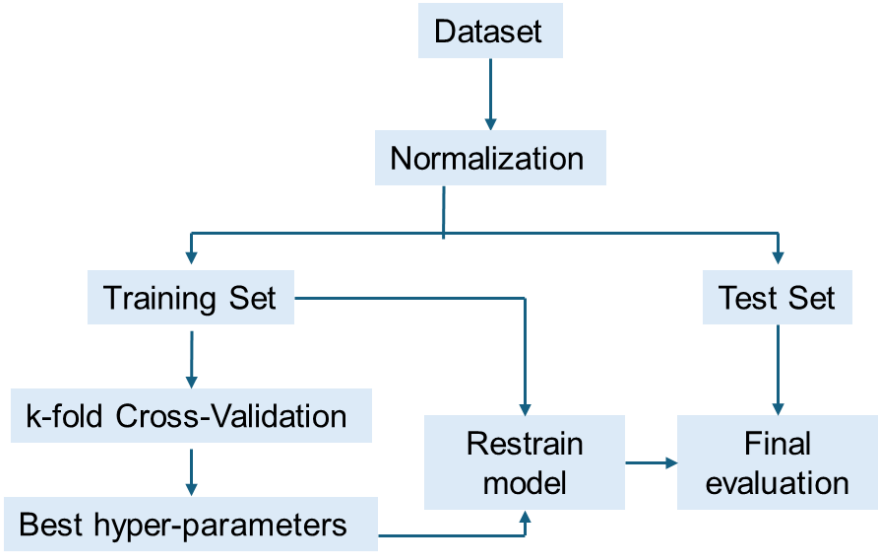

Fig. 3-7 Training flow of the WUI-EF prediction model.

3.3.2 Performance evaluation

The established model was assessed based on the discrepancy between predictions and actual values. Two evaluation metrics are employed: mean squared error (MSE), defined in Eq. (3.20) and coefficient of determination (R^2) in Eq. (3.21).

$$MSE = \frac{1}{N}\left(\sum_{i=1}^{N}(Y_{predicted} - Y_{actual})\right)^2 \tag{3.20}$$

$$R^2 = 1 - \frac{\sum_{i=1}^{N}(Y_{predicted} - Y_{actual})^2}{\sum_{i=1}^{N}(Y_{predicted} - Y_{mean})^2} \tag{3.21}$$

where $Y_{predicted}$ is the model prediction, Y_{actual} is the actual output, Y_{mean} is the mean of target outputs, and N is the number of instances.

3.4 Earth-scale chemical transport modelling

3.4.1 Emission inventory

This study selected two of the most typical and widely used products: GFED4 (based on BA) and the GFAS (based on fire radiative power). Combined with emission factors, both inventories can be the emission input for atmospheric chemical transport modelling.

GFED is the earliest global BA dataset that uses MODIS data to monitor the BA and Carnegie-Ames-Stanford Approach (CASA) Model to calculate fuel consumption (Giglio *et al.* 2013; Chen *et al.* 2023b). The satellite BA data are merged with active fires from various sensors to monitor the small fires (GFED 4.1s). In addition to BA-based methods, global fire emissions are also estimated by fire power. One representative product is the GFAS, which assimilates FPR observations from the MODIS sensors onboard the Terra and Aqua satellites (Kaiser *et al.* 2012). The fire radiative power was linked to the dry matter combustion rates and aerosol emission rates, which were used to calculate the fire emissions.

3.4.2 Atmospheric chemistry transport modelling

The full aerosol atmospheric transport and annual average fire-sourced $PM_{2.5}$ exposure is estimated using a global chemical transport model, GEOS-Chem. GEOS-Chem is a widely used CTM that has been applied to estimate the contribution to ambient air pollutant concentrations from a specific emission sector.

This study employs GEOS-Chem v14.4.0, driven by MERRA-2 meteorological fields from NASA's Global Modelling and Assimilation Office. The gridded dataset, with a 0.5° × 0.625° resolution, is publicly available via NASA Goddard Earth Sciences Data and Information Services (https://disc.gsfc.nasa.gov/). The GEOS-Chem model operates at the same spatial resolution with 47 vertical layers. Simulations were conducted from 2014–2016 with a six-month spin-up starting from July 2013. $PM_{2.5}$ in the bottom layer were taken to represent the ambient $PM_{2.5}$ concentrations of public exposure.

3.5 Epidemiological model

In this study, we employ the Global Exposure Mortality Model for Five Causes of

Death (GEMM-5COD) to estimate premature mortality linked to $PM_{2.5}$ exposure from smouldering peat fire emissions. GEMM-5COD quantifies the health risk associated with long-term exposure to $PM_{2.5}$ based on a non-linear exposure–response function derived from extensive epidemiological data (Burnett *et al.* 2018). The model accounts for five major causes of death, including Ischaemic Heart Disease (IHD), Lung Cancer, Stroke, Chronic Obstructive Pulmonary Disease (COPD), and Lower Respiratory Infections (LRI). The model first calculates excess $PM_{2.5}$ exposure by subtracting a theoretical minimum risk exposure level (TMREL) of 2.4 μg/m^3 from the ambient concentration:

$$z\left[\frac{\mu g}{m^3}\right] = \max\left(0,\ \begin{matrix} PM_{2.5}\ ambient \\ concentration \end{matrix} - 2.4\right) \tag{3.22}$$

where $z[\mu g/m^3]$ is the excess $PM_{2.5}$ exposure. The exposure–response function (ERF), $\Gamma(z,\ age)$, describes the relationship between $PM_{2.5}$ exposure and health risk, incorporating age-specific susceptibility:

$$\Gamma(z,\ age) = \frac{ln\left(1 + \frac{z}{\hat{\alpha}}\right)}{1 + exp\left(\frac{\hat{\mu} - z}{\hat{\pi}}\right)} \tag{3.23}$$

where parameters $\hat{\alpha}$, $\hat{\mu}$, and $\hat{\pi}$ play roles in building non-linear relationship between $PM_{2.5}$ exposure and health risk. The actual value of $\hat{\alpha}$, $\hat{\mu}$, and $\hat{\pi}$ is dependent on the age group and death cause. For simplicity, we use "Group 25+" in this work, instead of the five-year age groupings for excess mortality estimation across different age segments provided by GEMM model. Then, the hazard ratio (HR) is computed as

$$ln\begin{pmatrix} hazard \\ ratio \end{pmatrix} = \left(\hat{\theta} \pm 2\ se\right) \cdot \Gamma(z,\ age) \tag{3.24}$$

where $\hat{\theta}$ represents the estimated exposure-mortality coefficient and se is its standard error. Combined with baseline mortality data obtained by the latest Global Burden of Diseases, Injuries, and Risk Factors Study (GBD) 2021 analysis (Brauer *et al.* 2024), the premature death associated with fire-sourced $PM_{2.5}$ exposure can be estimated:

$$\begin{matrix} Number\ of \\ deaths \end{matrix} = \left(1 - \frac{1}{\begin{matrix} hazard \\ ratio \end{matrix}}\right) \cdot \begin{matrix} Baseline \\ mortality \end{matrix} \tag{3.25}$$

CHAPTER 4 Persistent smouldering fires: a lab large demonstration

4.1 Introduction

Peat, as a carbon-rich organic soil, accumulates a considerable amount of incompletely decomposed vegetation residues under anaerobic conditions (Page *et al.* 2002; Hugron *et al.* 2013). Peatlands are essential terrestrial carbon pools, storing one-third of the world's soil carbon (500-600 Gt C), as much carbon as surface vegetation globally, and may be of similar magnitude to the atmospheric carbon pool (~850 Gt C) (Ballhorn *et al.* 2009; Turetsky *et al.* 2015). Peat is also a porous and charring natural fuel that is prone to smouldering fire. Smouldering is a slow, low-temperature and flameless, and one of the most persistent types of combustion (Rein 2009, 2013) (**Fig. 4-1 a-b**). Due to climate change and human activities, peatlands are more prone to large-scale fires than ever before (Jolly *et al.* 2015; Witze 2020). Over the past few decades, frequent peat fires have caused severe ecological and climatic damage, as well as significant economic losses (Mack *et al.* 2011; Jolly *et al.* 2015; Turetsky *et al.* 2015). For example, in 2019, the slash-and-burn activities in southeast Asia resulted in mega-scale peatland wildfires that burned for several months, leading to severe cross-border air pollution and many health issues for the nearby residents (Normile 2019; Goldstein *et al.* 2020).

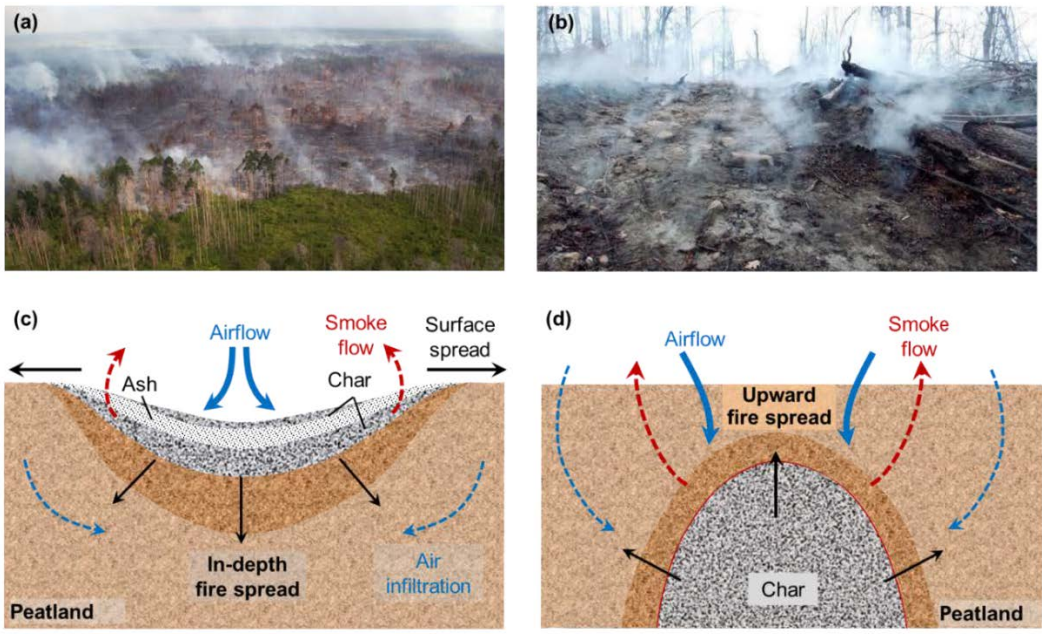

Fig. 4-1 Smouldering peat fires from aerial view (courtesy: Reuters 2017) **(a)**; deep peat fire in the field (courtesy: WV News 2016) **(b)**, lateral and downward peat fire spread after ignition on top surface **(c)**; and upward spread of deep-layer peat fires (Huang and Rein 2017, 2019) **(d)**.

Peat can hold a high MC to prevent ignition, but natural and anthropogenic-induced droughts can dramatically increase the risk of peat fire (Sinclair *et al.* 2020). Similarly, the ignition sources of peat fire can also be led by natural (e.g., lightning (Anderson 2002; Zhang *et al.* 2020), flaming wildfire (Lin *et al.* 2019), self-heating ignition (Restuccia *et al.* 2017) and volcanic eruption (Svensen *et al.* 2003)) or man-made reasons (e.g., deforestation (Silva *et al.* 2021), poor land management (Dickinson and Ryan 2010), accidental ignition and arson (Prestemon and Butry 2005)). In general, smouldering requires less ignition energy than flaming combustion and can persist in wetter and lower oxygen conditions (Huang and Rein 2016a; Lin *et al.* 2019), and once ignited, it can propagate vertically and horizontally to expand the burning area rapidly (**Fig. 4-1c**) (Huang and Rein 2019). These fires can burn for months or even years, despite the extensive rain, weather changes or firefighting operations, thus sustaining the largest and most persistent fire on Earth (Rein 2013).

When the rainy season arrives or substantial firefighting operations take effect, even though near-surface smouldering fires could be extinguished, hidden underground smouldering hotspots may still sustain at a low temperature and spread at a very low propagation rate that is extremely difficult to detect by human patrols and satellite imaging (Rein 2013; Rein and Huang 2021). With the advent of the dry and hot season, the soil on the surface gradually dries, and deep smouldering spots begin to spread upwards towards the ground and flare up, forming a new fire point (**Fig. 4-1d**) (Huang and Rein 2019; McCarty *et al.* 2020). This recurrent fire behaviour has been observed in the peatlands of Southern Africa, Southeast Asia and even the Arctic region (Gumbricht *et al.* 2002; Rein 2013; Scholten *et al.* 2021). However, such 'holdover' or deep peat fire behaviours in global peatlands are still poorly understood, so we need to explore the underlying mechanism and limiting conditions of these persistent in-depth peat fires.

Past studies have investigated the dynamics of smouldering peat fires, including heterogeneous chemical kinetics (Huang and Rein 2014), ignition (Frandsen 1987, 1997; Restuccia *et al.* 2017; Lin *et al.* 2019), fire spread (Huang *et al.* 2016; Prat-Guitart *et al.* 2016b; Huang and Rein 2017, 2019; Yang and Chen 2018), extinction (Lin *et al.* 2021b; Santoso *et al.* 2021; Mulyasih *et al.* 2022) and fire emissions (Rein *et al.* 2009; Hu *et al.* 2018, 2019a). For downward smouldering spread, small-scale lab experiments have

demonstrated that fire can spread to a depth of about 30 cm (Benscoter *et al.* 2011; Huang and Rein 2017). Airborne LiDAR measurement showed that real peat fire could spread down to 50 cm and last for a long period (Rein *et al.* 2008; Ballhorn *et al.* 2009).

Our previous small-scale pilot experiments showed that smouldering peat fires could be ignited by a coil heater at a depth up to 15 cm and then spread upward to the surface (Huang and Rein 2019). During the in-depth burning and upward fire spread process, no visible smoke plume or soil volume change was observed until the fire front reached the ground surface, indicating the difficulty of detecting deep peat fires visually. So far, there is a lack of both lab-scale and field-scale smouldering research to reveal the in-depth smouldering propagation behaviour. Moreover, no large experiment has been conducted to explore smouldering fire behaviour at soil layers deeper than 30 cm.

This study conducts a series of laboratory experiments on peat columns of 1 meter tall to explore the underground peat fire behaviours. We also quantify the temperature profile, spread dynamics, persistence, and CO emission of deep peat fires that burn for more than 10 days. This work helps reveal the underlying mechanism of the in-depth smouldering wildfires in peatland and supports future larger-scale peat fire experiments in the field.

4.2 Experimental phenomena and results

The surface and hidden underground smouldering fires in peatlands were noticed previously but poorly understood because it is hard to observe the phenomenon. This section reports and compares the persistently burning and propagation behaviour of smouldering peat fire (initial MC = 10%) with different ignition heights. The temperature history for typical cases is shown in supplementary videos.

4.2.1 Base case of surface ignition

The base case was initially conducted where the smouldering fire was initiated on the surface of the air-dried peat column (MC = 10%; z = 0). **Fig. 4-2** shows the thermocouple measurements of the base case, where the negative signs represent the distance below the initial free surface. After heating by electric coil for 60 min, the temperature near the

surface exceeded 500 ºC, suggesting the formation of a robust smouldering front. Afterwards, smouldering spread downward, where a layer of black char and white ash layer was formed on the free surface due to environmental heat losses. Such phenomenon was also observed in other experiments and real scenarios (Huang and Rein 2017; Lin *et al.* 2020b). As the top ash layer became thicker, the oxygen supply from the top surface to the deeper smouldering front must decrease, so the overall smouldering temperature decreased with the depth from around 550 ºC to around 350 ºC.

After about 4 days, the peak temperature of the smouldering front decreased to about 300 ºC, which was not strong enough to fully oxidised the char layer (see TGA in **Section 3.1.1**). Thus, a lot of unburned peat and char remained. As a result, the peat volume remained constant, and the top surface no longer regressed and remained at about -35 cm.

For better observation, **Fig. 4-2b** further plots the temperature profiles at different moments at a 1-day interval, where the solid red lines represent the temperature profiles, and the dashed black line indicates the position of the top surface after the regression. As expected, after the ignition, a strong smouldering front gradually propagated downward with a regressing top surface. The hottest zone is not on the top surface but consistently below the top free surface. It was because the accumulating layers of unburned char and ash on the top reduced the environmental cooling. However, after the initial fast expansion, the smouldering fire front split into two separated burning fronts at different depths. Such fire phenomenon is observed for the first time.

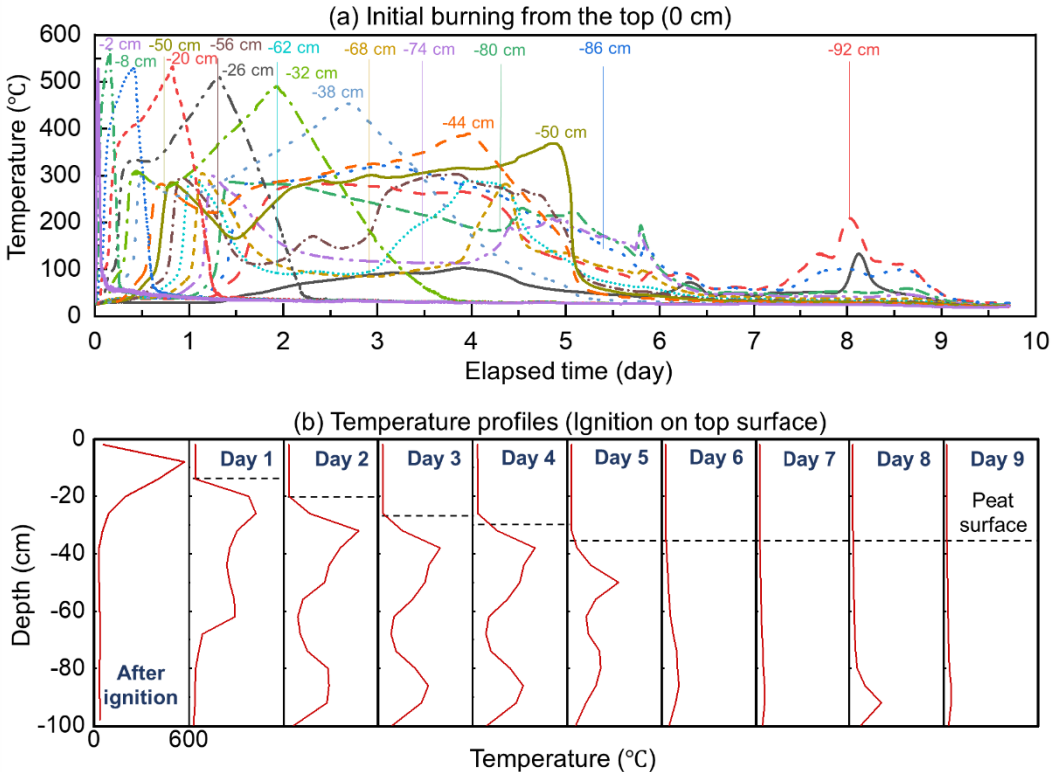

Fig. 4-2 Base case with peat fire ignited on top free surface, thermocouples data **(a)** and evolution of temperature profile **(b)**. The negative sign denotes depth below surface.

The primary reason for the separated multi-depth burning was that the downward fire propagation was localised. In other words, the cross-section area of 24 cm × 24 cm was not entirely ignited because it was much larger than the size of the smouldering front (5~10 cm) (Huang *et al.* 2016). This is different from previous smaller-scale tests with a cross-section area of 10 cm × 10 cm, where the entire cross-section was ignited and propagating (Huang and Rein 2017; Lin *et al.* 2020b). Herein, some air might bypass the localised shallow fire spot and feed the deeper fire front from the lateral direction. Then, we expect that the real underground peat fires also split into multiple smouldering fronts and propagate in different directions because of an even greater oxygen supply from various directions. This is why the spread and growth of peat fires in the field are very fast and difficult to predict. Even if all shallow smouldering fires are extinguished, the deep fires may still survive, so it is not easy to detect them.

Moreover, from **Fig. 4-2b**, we found the first smouldering front propagated faster, first reached the bottom of the reactor on Day 2 and then sustained a weak local burning due to the limited oxygen supply. Afterwards, the second smouldering front continued

propagating downward and eventually, two fronts emerged and continued burning for another 4 days. Note that the peak temperature measured on Day 8 was higher than the previous two days. It was because the thermocouple measurement was only a point in the axis, and they were not in contact with the burning zone on Days 6 and 7. This also proves that the deep smouldering fire front does not cover the whole cross-section area under the limited oxygen supply. The whole burning and propagation process lasted for more than 10 days, showing the persistent and localised smouldering of deep peat fires. After the test, residue weight was measured, and only 25% of the total mass was lost in the fire. Thus, the burning of deep smouldering peat fire is incomplete, because of limited oxygen supply and low fire temperature.

Afterwards, to simulate the in-depth burning and re-emerging behaviour of peat fires, we initiate smouldering fires at different depths of the peat column (starting from -20 cm) to observe the smouldering burning and fire propagation behaviours.

4.2.2 Shallow peat fire propagation (upward-and-downward)

Fig. 4-3 a-b shows the temperature evolution of the peat column where the initial burning depth is 20 cm. After forced ignition at z = -20 cm, the smouldering fire front firstly expanded, as indicated by the thermocouple measurements. During this process, no smoke or volume change could be observed visually until the expanding smouldering front approached the peat surface. After about 12 h, the smouldering fire re-emerged on the top free surface with heavy smoke and higher temperatures. Then, a black charring spot appeared and expanded laterally, quickly covering the entire top surface under the rich oxygen supply from the ambient. These holdover, hibernation, and re-emerging processes are the same as the observations in our previous pilot experiments (Huang and Rein 2019) as well as the real fire scenarios in the peatlands of Southern Africa, Southeast Asia and even the Arctic region (Gumbricht *et al.* 2002; Rein 2013; Scholten *et al.* 2021). However, once the smouldering front re-surfaced to the surface, no flaming fire was ignited as the organic soil is prone to smouldering combustion (Lin *et al.* 2019). In real fire scenarios, other surface fuels (e.g., leaves and branches) on the peatlands may be ignited or even trigger a flame. This process requires future investigations.

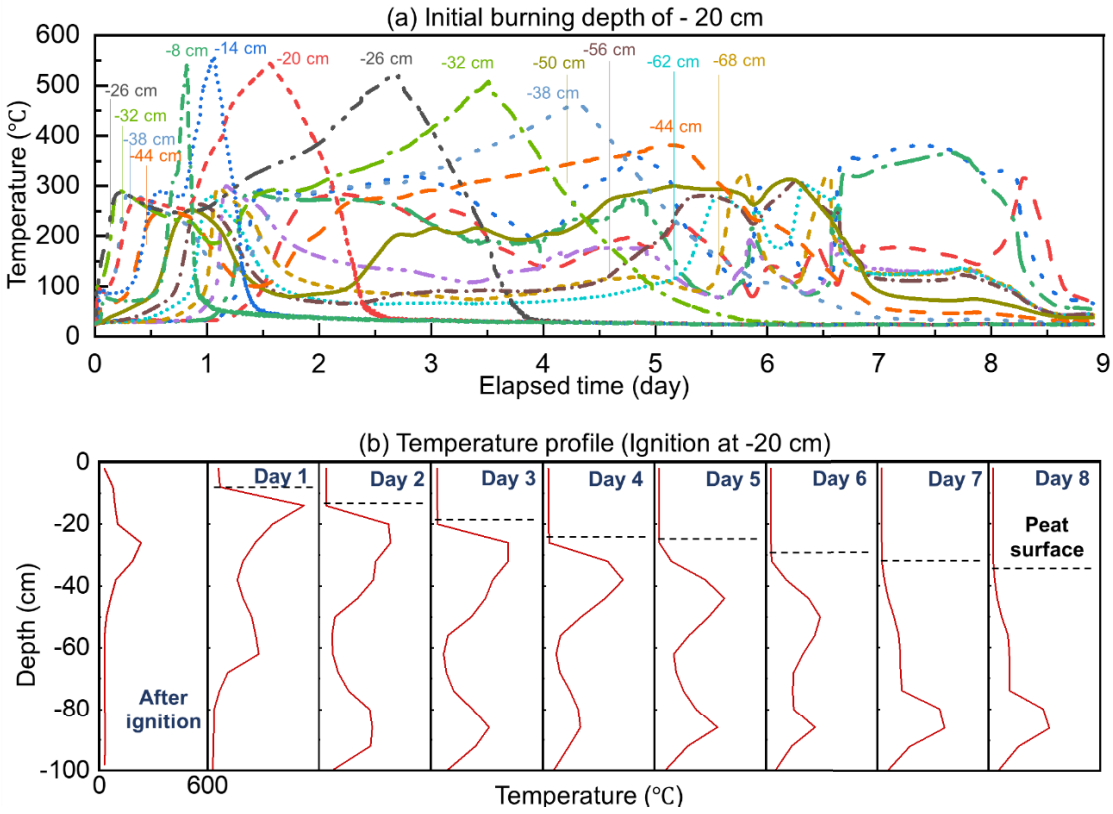

Fig. 4-3 Thermocouple measurement of smouldering peat fire ignited at the depth of -20 cm. The negative sign denotes depth below surface.

Afterwards, the smouldering only propagated downward, and its process was similar to that initiated on the top surface in **Fig. 4-2**. During this process, two burning fronts were also observed, and the peat surface also regressed by around 35 cm after persistently burning for 9 days. The observed peak temperatures on Days 7 and 8 are also larger than that on Day 6, because of the localised burning under limited oxygen supply to the deep fire front. In other words, the smouldering fire seems to stay at -80 cm for 6 days, while it may still have local fire spreads toward different directions in the lateral plane, requiring further investigations.

4.2.3 Deep fire downward propagation

By decreasing the initial burning depth to -40 cm or -60 cm, a different burning phenomenon was observed, as shown in **Fig. 4-4**. After ignition, the smouldering front was persistently burning in the deep peat layer. Above the ignition location, the peat temperature never exceeded 100 °C, and the residual was fresh peat. Therefore, we can first conclude that there was no upward fire spread.

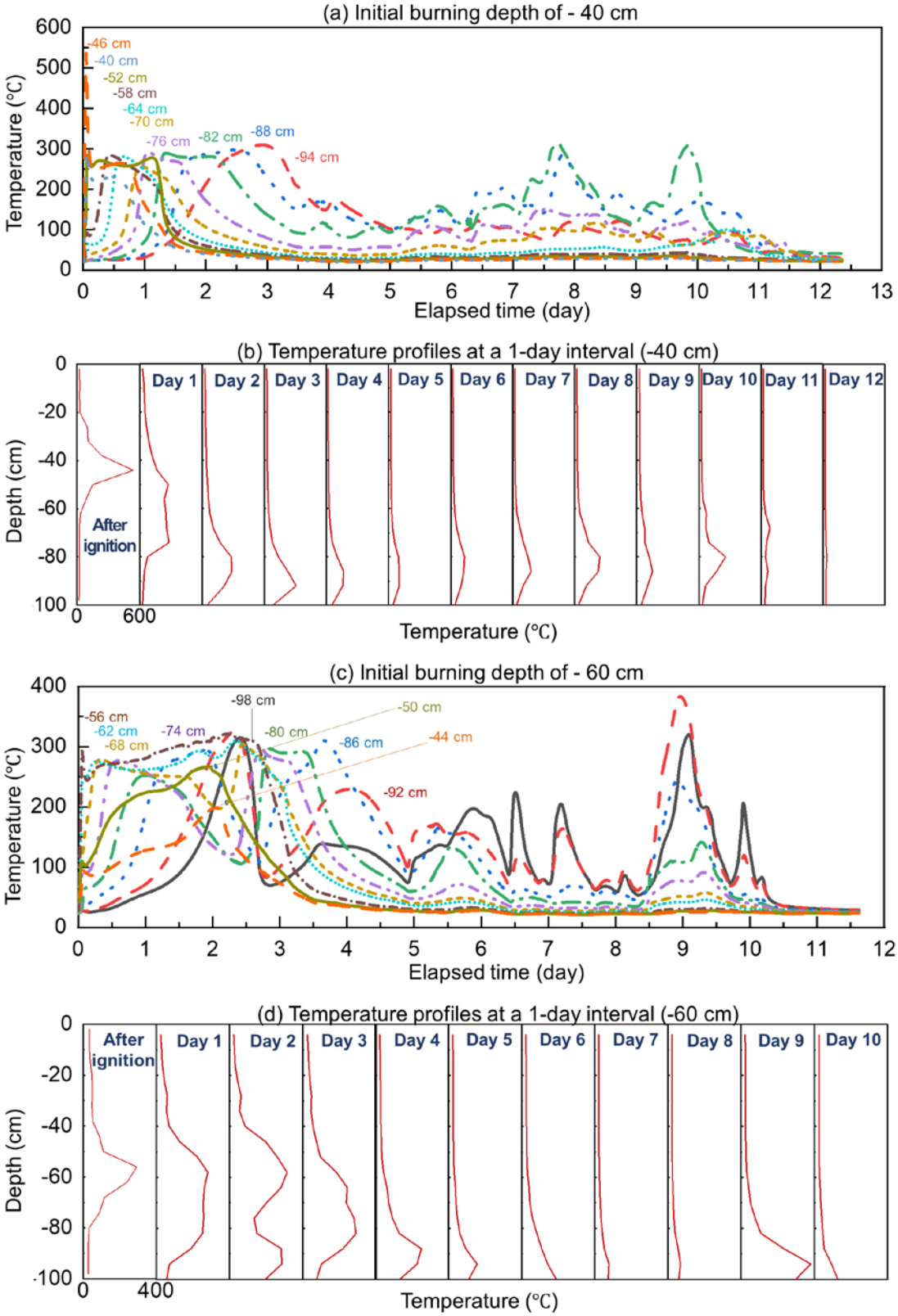

Fig. 4-4 Thermocouple data and temperature profile of smouldering peat fire ignited at depths of -40 cm **(a-b)** and -60 cm **(c-d)**. The negative sign denotes depth below surface.

The peak temperatures below the ignition location barely reached 300 ºC, because the thermocouples were not in contact with the local burning fronts. Nevertheless, we can see the overall fire propagation was downward, and there must be multiple localised fire propagation in different directions. Due to the low smouldering temperature, even after burning for 10 days, the total mass loss was less than 10%. These local fire fronts were not stable that were easily extinguished under the limited oxygen supply. Therefore, even after burning for 10 days, the total mass loss was less than 10%. The residual in the deep layer also included some uncharred fresh peat soil. Therefore, the burning of deep peat fire was incomplete, which is another reason for forming multiple burning fronts in deep layers. These deep local fire fronts were unstable under limited oxygen supply, so they may not always be self-sustained. Moreover, during the entire burning process of 10 days, no visual smoke, noticeable collapse, or surface regression was observed, further demonstrating the difficulty of monitoring these in-depth smouldering peat fires. After the sample was cooled down, we waited for another 3 days to avoid missing the re-emerging fire, but no further temperature increase was observed.

4.2.4 No fire propagation (local partial burning)

By further moving the ignition position deeper to -80 cm or -100 cm, different fire phenomena are observed. As shown in **Fig. 4-5**, after the ignition heating, the temperature of the ignition zone could exceed 400 ºC, indicating a robust heating process. After the heating power was off, the temperature could only sustain at about 300 ºC, close to the minimum smouldering temperature of this kind of peat (Lin *et al.* 2019). However, the fire was successfully initiated because there was some clear temperature increase from time to time.

Within the first 2-3 days after the ignition, the burning zone slightly expanded, but there was neither clear upward nor downward fire spread. Afterwards, the burning was only sustained in these small regions, and a clear fluctuation of temperature was also observed over the next several days because of the limited and uneven oxygen supply. Eventually, after about 10 days, all measured temperatures were decreased to ambient, and no regression of the peat column could be observed. By examining the fire residue, we found that all peat above the ignition point was nearly undisturbed. Around and below

the ignition zone, most of the peat soil was charred, while not much white ash was observed. Around and below the ignition zone, most of the peat soil was charred, while not much white ash was observed because of the lack of oxygen to sustain a robust oxidation process.

The overall burning was so weak that it was both a long-term burning process and a prolonged extinction process. Note that the moisture re-distribution is also possible as the peat sample is relatively large. A burning zone at the deep layer would evaporate the available water in the peat which is potentially re-condensed in the upper layer. As a result, the MC of the upper peat layer may increase and protect the unburned region which contributes to the self-suppression of the smouldering fire. More investigations are necessary in future field fire tests.

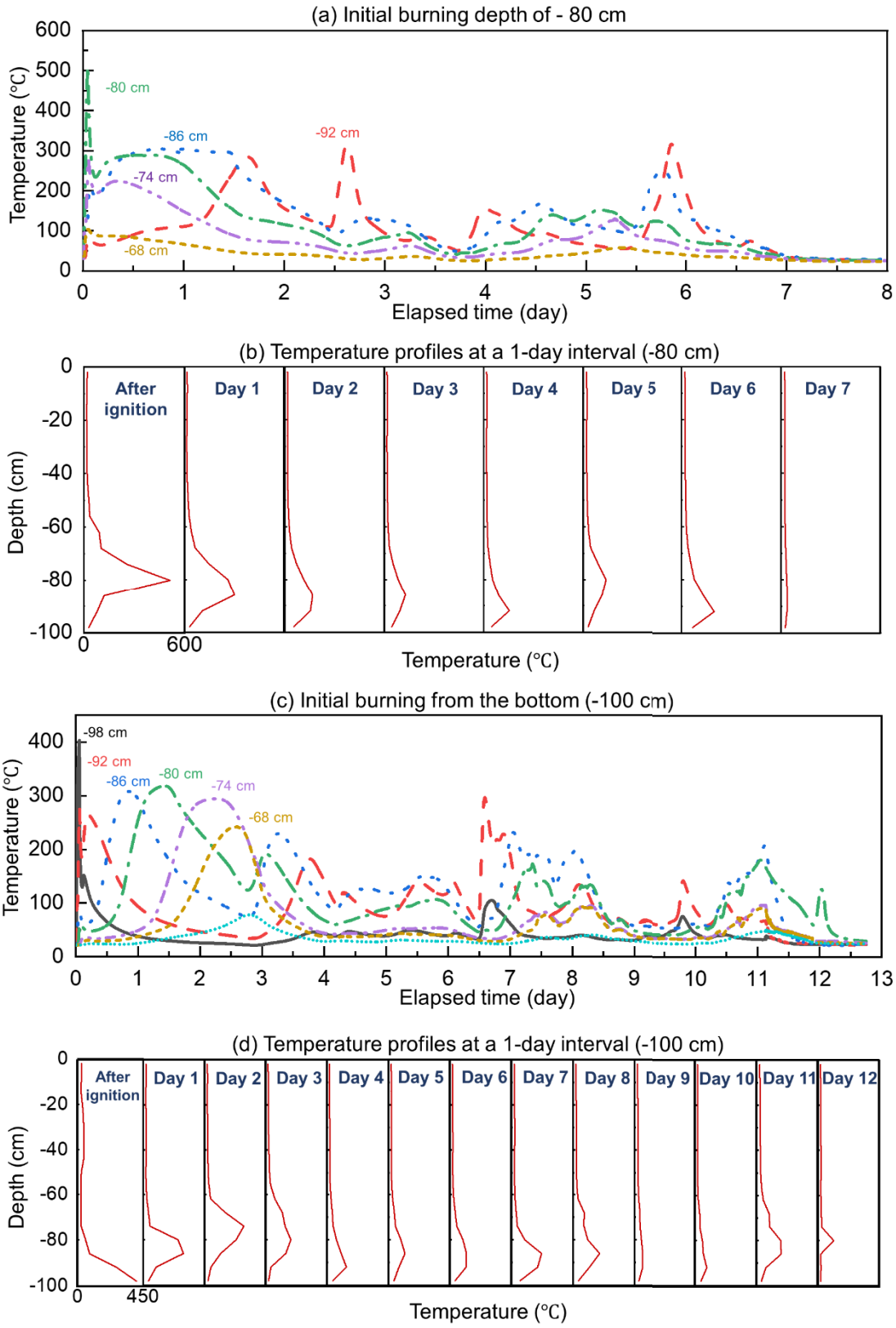

Fig. 4-5 Thermocouple measurement of smouldering peat fire ignited at the depth of -80 cm **(a-b)**, -100 cm **(c-d)**. The negative sign denotes depth below surface.

4.3 Analysis and discussion

4.3.1 Smouldering temperature

Fig. 4-6 compares the measured peak smouldering temperatures of cases with different initial burning depths. It is worth noting that the thermocouple, as a point sensor, may not capture the hottest point of the localised smouldering fire front at that depth, so the overall peak temperature may be inevitably underestimated. Therefore, although Some measured peak temperatures are lower than 250 ºC, but it does not mean that smouldering can sustain under such a lower temperature.

For the fire initiated on the surface, the temperature first decreases from about 550 ºC to 350 ºC as the location drops from 0 cm to -40 cm. However, when the smouldering front propagates to lower than -40 cm, the peak smouldering temperatures almost remain stable at around 300 ºC which is slightly higher than the minimum smouldering temperature. Similarly, for the fire initiated at -20 cm, the temperature also first decreases from 0 cm to -40 cm and remains stable at locations lower than -40 cm. Comparatively, for the fire initiated lower than 40 cm below the top free surface, the smouldering temperature is no longer sensitive to the depth but remains constant at about 300 ºC.

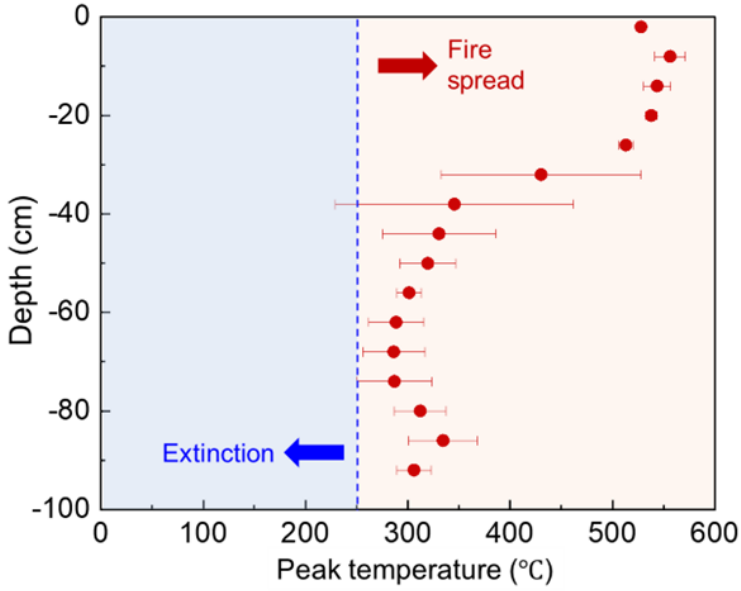

Fig. 4-6 Measured peak smouldering temperature at different depths of the peat fires (the error bar represents the standard deviation of the measured data).

In general, for the oxygen supply from the top free surface, the smouldering temperature will decrease with depth, because the accumulating ash layer on the surface will weaken the oxygen diffusing to the burning area (Huang and Rein 2017). This agrees well with the trend of smouldering temperatures above -40 cm, as shown in **Fig. 4-6**. However, as the smouldering fronts locate at a position lower than -40 cm, the temperatures no longer vary with the depth of the peat column. This may be because the oxygen supply from the top open surface becomes negligible, while lateral oxygen supply starts to dominate when the depth of the smouldering is larger than 40 cm. This also explains why the fire ignited below -40 cm only persistently smoulders locally or propagates downward without re-surface to the free ground. In the future, more experimental and numerical investigations will be essential to reveal the underlying mechanisms.

4.3.2 Burnt mass loss

After fire extinction, the residue mass of the 1-m peat column was measured to calculate the total burned mass loss. For example, if the 20% of mass is lost, it is equivalent to that 20-cm peat out of 1 m is completely burned. **Fig. 4-7** shows the mass loss and the equivalent burned thickness for different initial fire depths. Essentially, the smouldering combustion of deep peat fire is quite incomplete. For ignition on the top surface, only 25% of original mass is lost, which is reasonable for only 35 cm surface regression (**Fig. 4-2**). For deeper fires, the burning mass loss is less than 10%, where no surface regression or internal collapse was found. Therefore, despite of burning for more than 10 days, the burning mass loss is very small, where only a small amount of peat is partially pyrolyzed into char. Even smaller amount of char is oxidised, indicated by the low in-depth peak temperature (~300 oC). As the reaction rate increases exponentially with temperature, burning a longer duration at a lower temperature does not lead to a large mass loss.

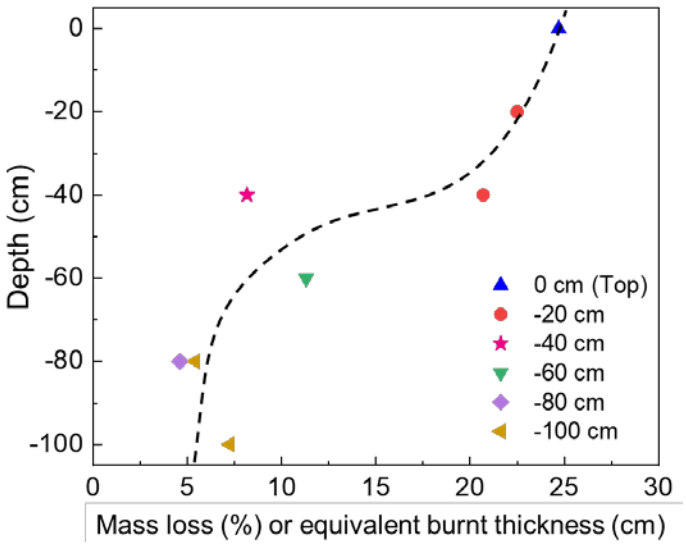

Fig. 4-7 Measured burned mass loss (or equivalent burned thickness) vs. initial peat fire depth.

4.3.3 Smouldering CO emissions

As smouldering is an incomplete combustion process, the CO emission is always the quantity of interest. From the viewpoint of chemical reactions, CO could both come from the pyrolysis of peat and the oxidation of char (Hu et al. 2018). Therefore, **Fig. 4-8** summarises CO emission concentrations (ppm) at 5 cm above the initial top surface for different depths of the peat fire.

During the ignition heating by the coil heater, there was a high level of CO (~10^3 ppm) for all ignition depths. For initially burning at 0 cm and – 20 cm in **Fig. 4-8 a-b**, the CO concentration is on the order of 10^2 ppm. The CO concentration continuously increases to 10^3 ppm during the upward fire spread and following lateral surface spread in **Fig. 4-8b**. Such a high CO concentration is a lethal threat to firefighters and nearby residents (Norris et al. 1986; Ernst and Zibrak 1998). Comparatively, for the in-depth smouldering or local burning cases in **Fig. 4-8 c-f**, the order of the CO concentration decreases to 10 ppm. It is worth noting that even if the in-depth smouldering is extremely difficult to be detected by satellites and patrollers, the CO concentration near the surface remains at a detectable level. This implies that measuring the CO emission near the peatland surface may be an effective method for detecting deep peat fires.

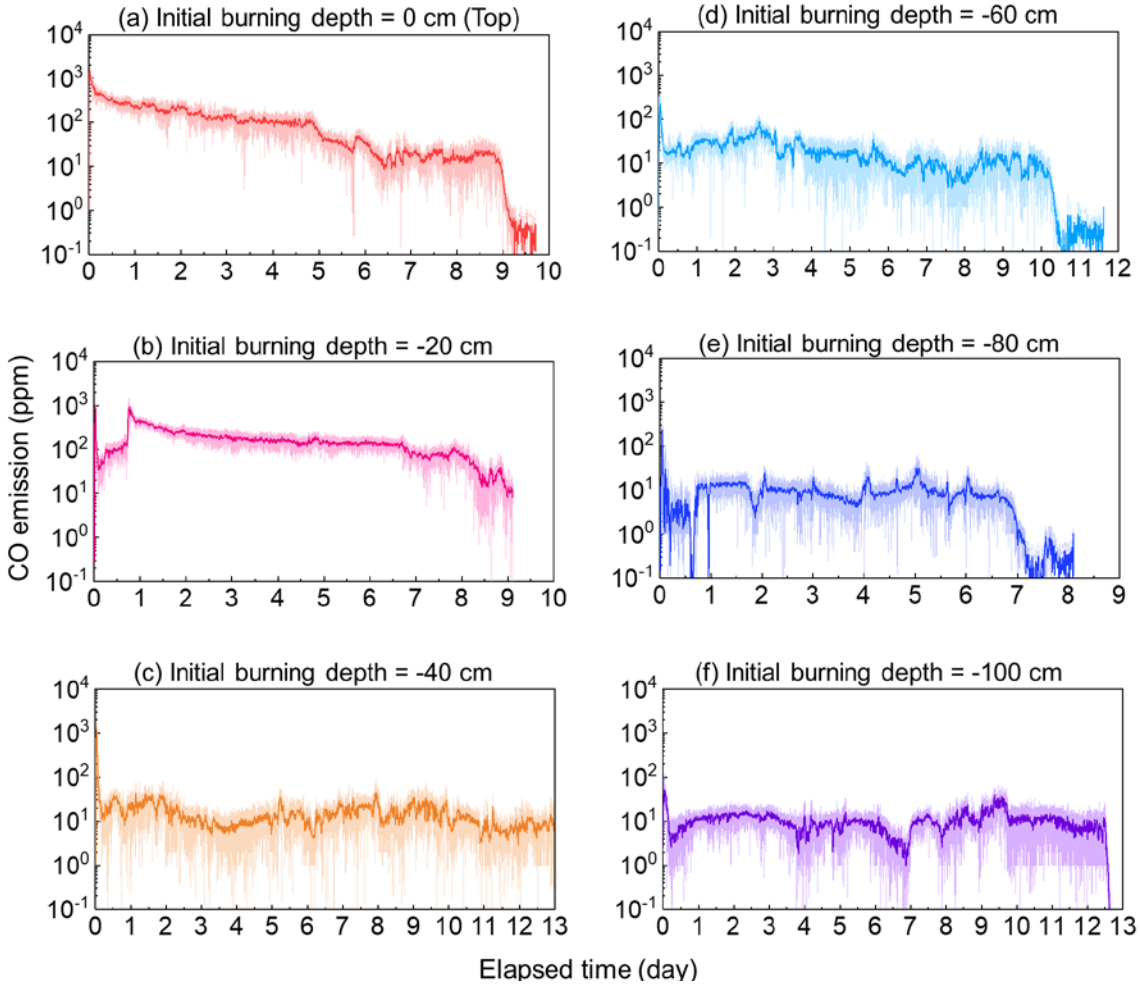

Fig. 4-8 Measured CO concentrations 5 cm above the top surface for peat fires at different depths.

4.3.4 Effect of moisture content

MC is one of the key parameters that affect the properties of peat soils (Frandsen 1987; Prat-Guitart et al. 2016b; Huang and Rein 2017; Dadap et al. 2019; Hu et al. 2019a). To investigate the effect of MC on the in-depth burning of the smouldering peat fire, a peat column with 50% MC was also ignited at -60 cm below the top-free surface. **Fig. 4-9** compares the temperature measure between dry peat (~10% MC) and wet peat (50% MC), where the burning duration of the wetter peat is significantly reduced. Specifically, as the MC increases from ~10% to 50%, the burning duration is decreased by half from about 11 days to 5 days.

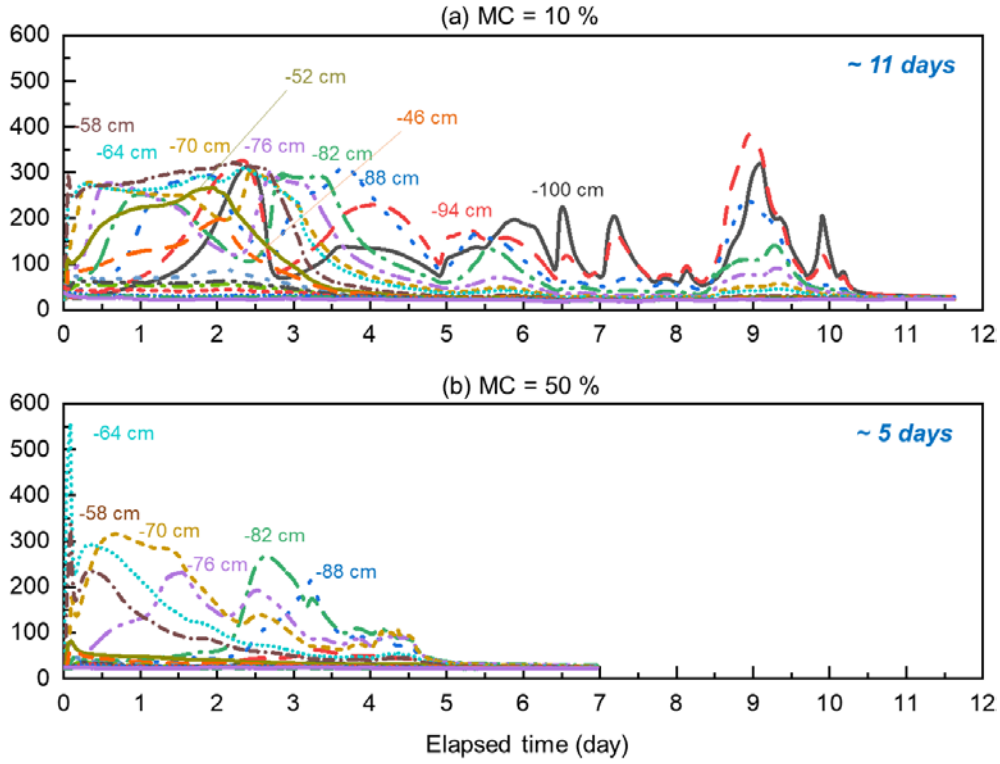

Fig. 4-9 Comparison of smouldering dry peat (MC = 10%) and wet peat (MC = 50%) in the same ignition position of -60 cm. The negative sign denotes depth below surface.

Initially, the wet peat (MC = 50%) was able to be ignited with the same ignition protocol (200 W for 60 min). However, the smouldering front only propagated for a short distance to about -80 cm with a decreasing peak temperature. As a result, the burning duration of wet peat is much shorter than that of dry peat, as in **Fig. 4-9**. In general, the peat moisture has three effects on the deep smouldering fire: (i) altering the thermal properties, (ii) increasing heat transfer efficiency through molecular diffusion; and (iii) acting as a strong heat sink during evaporation (McAllister et al. 2012; Lin et al. 2019). Also, the evaporated water may re-condense in the upper layer to protect the unburned region, which contributes to the self-suppression of smouldering fire. This implies the importance of keeping the peat soil moist in regions prone to underground fires.

While these values (MC = 10% and 50%) do not encompass the full range of field-relevant moisture contents, particularly high-moisture conditions (e.g., MC > 100%) and vertical gradients often observed in natural peat profiles, future work will expand on these scenarios to better reflect real-world heterogeneity.

4.4 Conclusions

In this chapter, we experimentally demonstrated that smouldering underground fires could sustain in deep soil layers for more than 10 days, regardless of the initial burning position. As the initial burning position becomes deeper, four smouldering burning modes can be observed: (I) downward propagation, (II) upward-and-downward propagation, (III) in-depth propagation, and (IV) no propagation (local burning). For the in-depth fire propagation and localised burning, no visual smoke, noticeable collapse, or regression was observed, indicating the difficulty of detecting deep peat fire.

For peat fires shallower than 40 cm, the peak smouldering temperature decreases as the depth increases. For fires deeper than 40 cm, the smouldering temperature remains at about 300 ^{o}C and becomes insensitive to the depth, revealing the dominant role of oxygen supply in peat fire dynamics in deep soil layers. Despite of long-term burning, the mass loss fraction is small, because the low smouldering temperature causes incomplete combustion. The CO concentration near the surface varies on the order of 10 and 10^2 ppm, so it can be used to detect underground fires and monitor its intensity. High peat MC can slow down in-depth fire propagation and reduce the burning duration.

CHAPTER 5 Experimental study on oxygen thresholds: limiting oxygen concentration and supply rate

5.1 Introduction

Smouldering combustion is a sluggish, low-temperature, flameless process driven by exothermic heterogeneous oxidation (Ohlemiller 1985; Rein 2013; Rein et al. 2016). smouldering in porous fuels ignites easily from weak heat sources or self-ignition, enabling a rapid transition to flaming combustion (Lin et al. 2019, 2021c; Santoso et al. 2019; Wang et al. 2021). Once ignited, smouldering persists under extreme conditions, including low oxygen and high fuel moisture, making it dominant in residential, industrial, and natural fires (Quintiere 1997; Huang and Rein 2016a). For example, underground peat fires can survive in deep soil layers with limited oxygen supply, resulting in long-lasting combustion phenomena on Earth (Rein and Huang 2021). On the other hand, persistent smouldering combustion has also been applied for the removal of organic wastes with a high MC (Yermán et al. 2017; Torero et al. 2020; Chen et al. 2022), showing an excellent prospect for industrial application. Therefore, a better understanding of smouldering combustion is vital to mitigate the smouldering fire hazards and promote smouldering-based technologies.

Two key mechanisms control the propagation and extinction of smouldering: oxygen supply and heat loss (Ohlemiller 1985; Rein 2013; Rein et al. 2016). The impact of heat loss on smouldering propagation and extinction has been systematically studied, revealing key insights such as quenching by cold walls (Lin and Huang 2021; Lin et al. 2021b, 2022a), moisture (Hadden and Rein 2011; Huang and Rein 2015; Ramadhan et al. 2017; Lin et al. 2020b, 2021b), and wind (Lin et al. 2021c). On the other hand, the effect of oxygen levels on smouldering has been explored since the 1970s (Moussa et al. 1977), but the current understanding of the oxygen supply thresholds for sustaining smouldering propagation is still limited. Schmidt et al. (Schmidt et al. 2003) found that in the self-ignition test, the smouldering fire could spread to the free surface under an oxygen concentration as low as 6%. Malow et al. (Malow and Krause 2008) showed that lowering ambient oxygen to 5% still could not extinguish the smouldering fire on coal and wood chips.

Even for the same fuel, different values of LOC were found in different experimental work (Belcher et al. 2010; Hadden et al. 2013; Huang and Rein 2016a; Richter et al. 2021). For peat, Belcher et al. (Belcher et al. 2010) found that the smouldering could not be

sustained below a critical oxygen concentration of 16% without forced oxidiser flow. However, Hadden et al. (Hadden et al. 2013) found that with a forced flow of oxidiser, smouldering peat fire can survive at oxygen concentrations as low as 11%. For smouldering wood, the LOC has been found to be 10% with a forced internal flow (Wang et al. 2017a) and 4-6% under intense irradiation (Richter et al. 2021). Our previous work (Huang and Rein 2016a) further found that the LOC of smouldering increases with the fuel MC. So far, the physical meaning of LOC in different smouldering experiments is still poorly understood.

Moreover, reducing the ambient pressure or gravity also lowers the oxygen supply threshold of smouldering (Walther et al. 1996; Bar-Ilan et al. 2004; Yamazaki et al. 2019, 2020). The observed minimum ambient pressure for smouldering is about 10~20 kPa (Yamazaki et al. 2019, 2020), similar to that of flame. Bar-Ilan et al. (Bar-Ilan et al. 2004) found that smouldering of polyurethane foam in microgravity spacecraft required a smaller oxygen supply than in normal gravity. However, the actual minimum rate of oxygen passing through the porous media is also unclear, so there is a big knowledge gap.

The oxygen supply rate into the porous fuel can be defined by the oxygen mass flux, which changes with the oxygen concentration and internal flow velocity. When a smouldering porous fuel is in contact with the ambient, the oxygen can flow into the fuel bed through pores, driven by diffusion and free convection, and such a natural oxygen supply is often sufficient for smouldering. Most past studies were performed with smouldering fuel samples open to the quiescent ambient or under an external wind, which cannot completely isolate the oxygen diffusion from the ambient. Thus, it is difficult to quantify the minimum oxygen supply rate and LOC for smouldering combustion.

This chapter aims to explore the minimum internal oxygen supply rate through a porous fuel bed that is able to sustain a robust smouldering propagation. An oxidiser flow with U up to 14.74 mm/s and X_{O_2} of 2%-21% is fed to peat soil that is isolated from extra oxygen supply from the ambient. The total mass loss and peak temperature under different oxygen supply rates were quantified. A theoretical analysis was proposed to explain the $U_{\min}$ and LOC of smouldering.

5.2 Results and discussion

5.2.1 Smouldering propagation phenomena

Fig. 5-1 shows the thermocouple measurements of self-sustained smouldering propagations and extinction under different airflow velocities (X_{O_2} = 21%). During coil heater ignition, the temperature near the ignition zone increases significantly above 500 ºC for all cases, so that the 15-min ignition is strong enough to initiate a robust smouldering zone. Among them, **Fig. 5-1a** shows the smouldering propagation when the oxygen supply is abundant (U = 4.4 mm/s). After the 15-min ignition, the gas flow was supplied from the bottom end of the reactor. The temperature first decreases but soon increases again, indicating a self-sustained smouldering propagation (Lin et al. 2020b). Moreover, a bidirectional propagation phenomenon is shown, evident by the temperatures over 300 ºC both above (z > 0) and below (z < 0) the ignition zone. **Fig. 5-1a** further illustrates the bidirectional propagation process under large flow velocity. As the oxygen supply is abundant, the oxygen is not fully consumed by the lower downward propagation front. Thus, the remaining oxygen can pass through to sustain the upward smouldering front, showing a bidirectional propagation mode.

As the gas flow was provided from the bottom end, the downward (opposed) propagating smouldering front has more than sufficient oxygen supply, showing a higher smouldering temperature and propagation rate. Comparatively, for the upward (forward) propagation, the oxygen supply is reduced, so that a lower smouldering temperature at z >0 could be observed, as shown in **Fig. 5-1a**. Because the oxygen supply is sufficient, the combustion of solid fuel is more complete. When all temperatures dropped to the ambient temperature, only a thin layer of mineral ash remained at the bottom, so the burning mass loss was maximised.

Fig. 5-1b shows that as the airflow velocity is decreased to 1.2 mm/s, the bidirectional smouldering propagation disappears, where the measured temperature above the ignition zone is lower than the minimum smouldering temperature (~250 ºC) (Lin and Huang 2021). Under such oxygen-limited conditions, the smouldering front only propagates towards the gas flow from the bottom (opposed), as illustrated in **Fig. 5-2b**. As the oxygen

is almost consumed by the downward smouldering front, no excess oxygen is left to sustain another upward (forward) smouldering propagation. After the test, an ash layer together with a thick layer of virgin fuel remained in the reactor, so that not all the peat and char were consumed, resulting in a lower burning mass loss (discussed more in **Section. 5.3.3**).

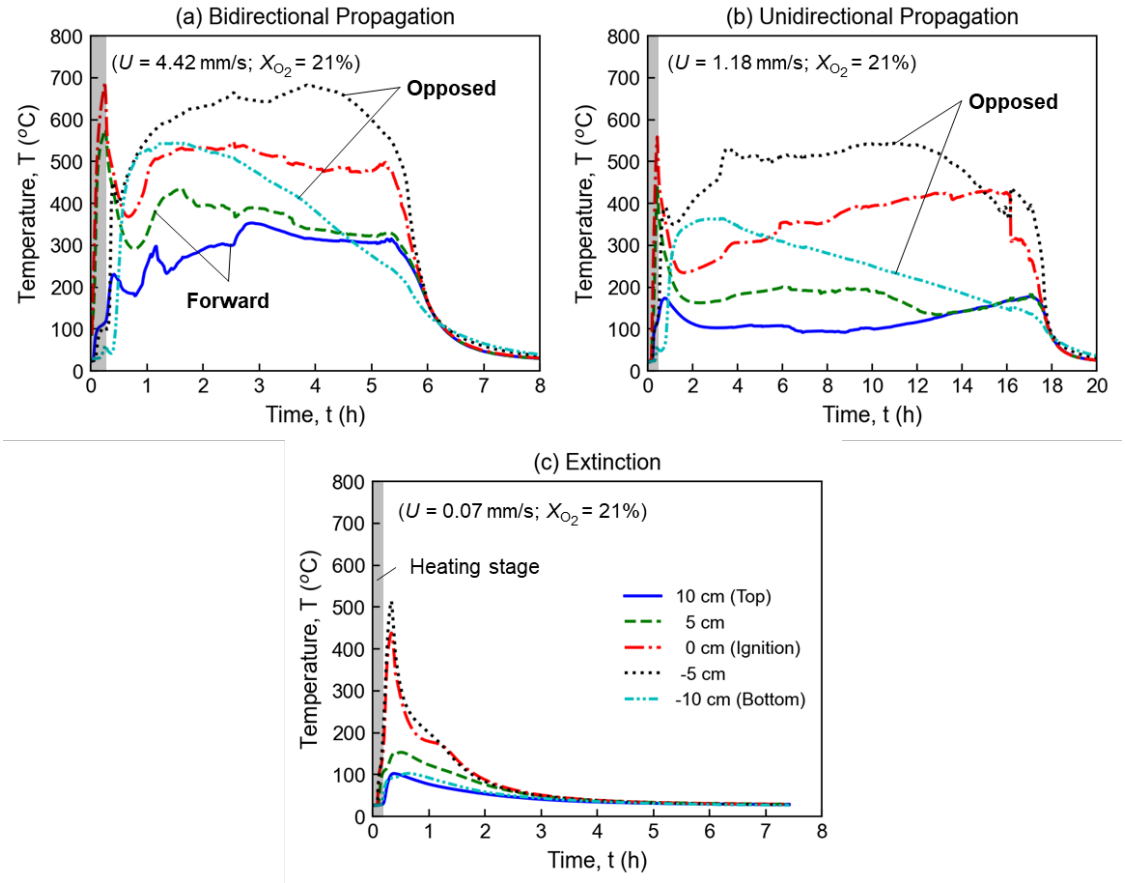

Fig. 5-1 Temperature profiles at different airflow (X_{O_2} = 21%) velocities. U = 4.42 mm/s with a bidirectional propagation **(a)**; U = 1.18 mm/s with a unidirectional propagation **(b)**; and U = 0.07 mm/s without smouldering propagation **(c)**.

Further decreasing the airflow velocity, eventually, smouldering combustion cannot be sustained. **Fig. 5-1c** shows the temperature profile of a no-propagation case, where the forced airflow velocity is 0.07 mm/s. During the ignition process, the temperature near the coil heater also reached about 500 °C, but once the heater was off, it kept decreasing to the ambient temperature without strong fluctuation. Further increasing the ignition du-

ration to 30 and 45 min, smouldering propagation still did not occur, so the applied air-flow velocity is below the smouldering limit of this fuel.

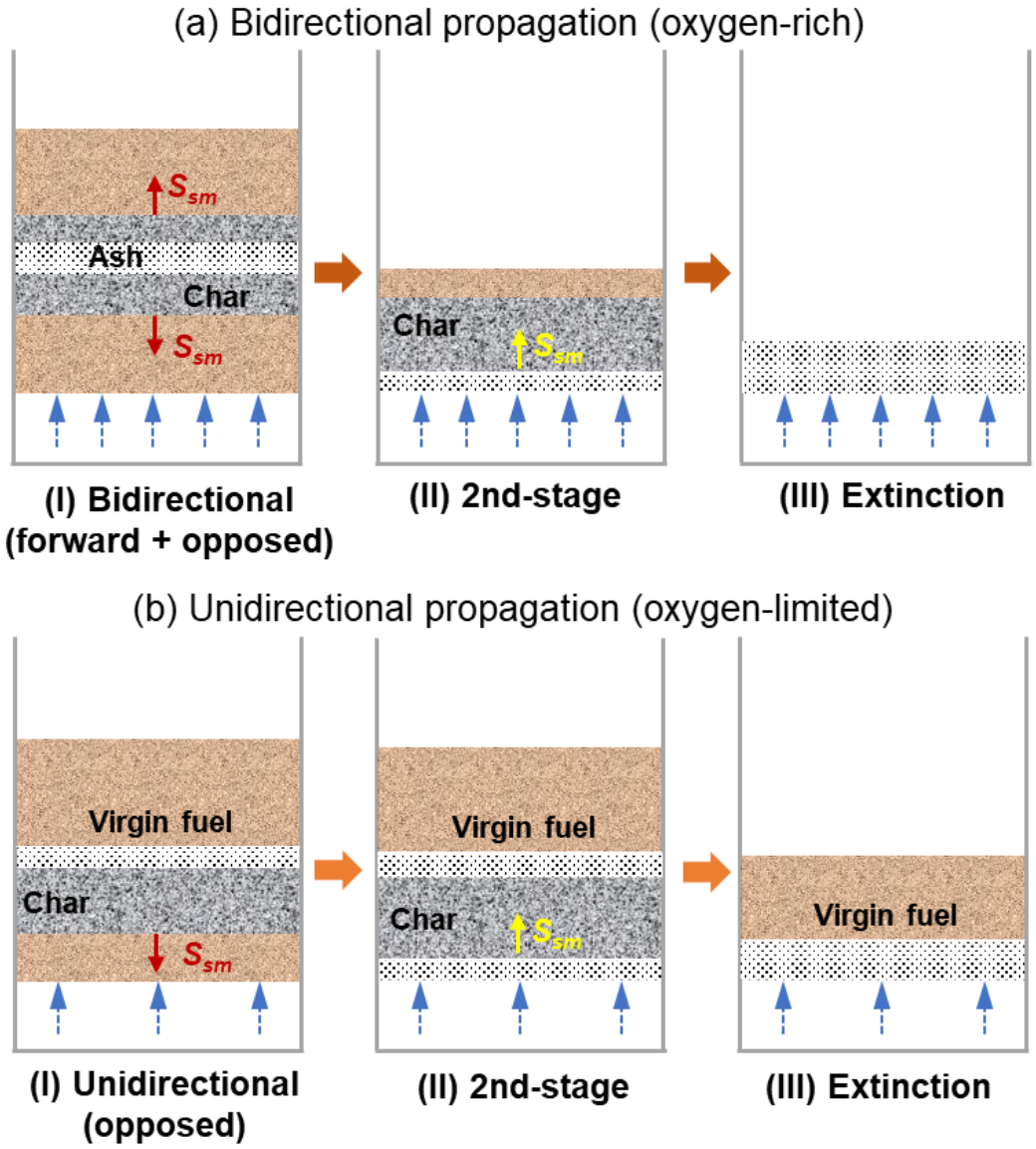

Fig. 5-2 Schematic diagrams of bidirectional smouldering propagation **(a)**; and unidirectional propagation **(b)** under different oxygen conditions.

5.2.2 Oxygen supply limit for smouldering

Fig. 5-3 summarises the experimental results of the U_{min} to sustain smouldering propagation under different X_{O_2}. The hollow, semi-solid, and solid markers represent the cases of "no propagation," "unidirectional propagation," and "bidirectional propagation"

of smouldering fire, respectively. As expected, the boundary of sustaining bidirectional propagation is much higher than that of sustaining unidirectional propagation. For example, with a forced airflow ($X_{O_2} = 21\%$), the minimum flow velocities to sustain bidirectional and unidirectional propagation are 2.9 mm/s and 0.3 mm/s, respectively.

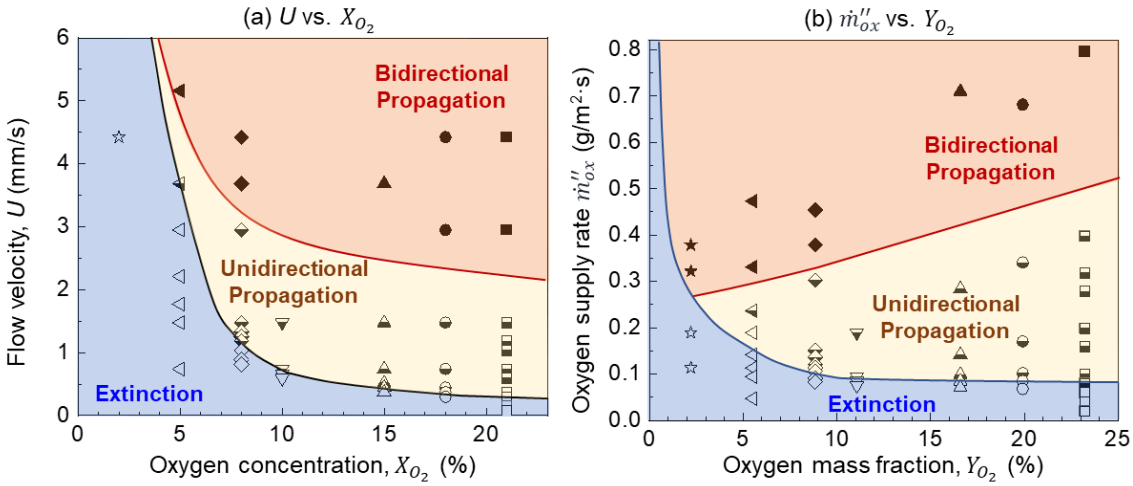

Fig. 5-3 Minimum flow velocity *vs.* oxygen concentration **(a)**; and minimum oxygen mass flow rate *vs*. oxygen mass fraction **(b)**.

Moreover, the required oxidiser flow velocities for both smouldering-propagation modes increase as the oxygen concentration decreases. For example, if the oxygen concentration is decreased from 21% to 10%, the minimum oxidiser flow velocity to sustain unidirectional propagation will increase by over two times from 0.3 mm/s to 0.7 mm/s.

Further reducing the oxygen concentration to 2%, smouldering combustion can still survive when the flow rate exceeds 12.5 mm/s. **Fig. 5-4** shows temperature profiles of a successful smouldering propagation under 2% oxygen concentration. To the best of the authors' knowledge, this is the lowest oxygen concentration reported for smouldering fire. It is reasonable because strong exothermic char oxidation still occurs at 2% oxygen concentration, as shown in the thermogravimetric data (**Fig. 3-1**). In other words, the LOC for smouldering peat fire is below 2%. Therefore, the minimum oxygen concentration (MOC) for smouldering peat is about 1.5 ± 0.5%. Such a low LOC of smouldering fire explains why underground smouldering peat fire can be sustained in the deep soil layers for months (Rein 2013).

Herein, empirical correlations between the minimum flow velocity and oxygen concentration can be formulated as

$$U_{min} = \begin{cases} \dfrac{0.06}{X_{O_2} - MOC} & \text{(unidirectional)} \quad (5.1a) \\ \dfrac{0.06}{X_{O_2} - MOC} + 2 & \text{(bidirectional)} \quad (5.1b) \end{cases}$$

where the unit of the internal flow velocity is mm/s, and R^2 of the fitting is 0.97. This fitting is selected based on the theoretical analysis in **Section 5.2.4**. Note that for using these correlations, the oxygen concentration has to be larger than the MOC (≈ 1.5%); otherwise, it has no physical meaning.

At 2% oxygen concentration, the unidirectional propagation can no longer be observed. When the oxidiser flow is very fast, it does not have sufficient time to fully react with the downward smouldering front. Thus, there is always a large amount of unreacted oxygen leaking to the upward smouldering front to form a bidirectional smouldering propagation. In other words, the boundaries of these two propagation modes will merge in a large oxygen supply rate (see **Fig. 5-3b**).

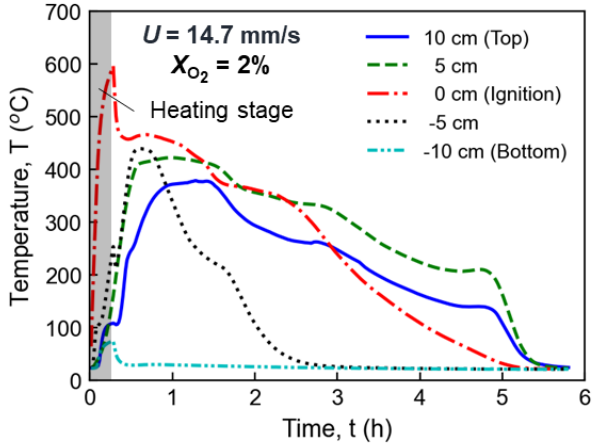

Fig. 5-4 Temperature profile at a flow velocity of U = 14.7 mm/s and X_{O_2} = 2%.

Fig. 5-3 further summarizes the $\dot{m}''_{O_2,min}$ to sustain different smouldering propagation modes under different Y_{O_2}. For the oxygen mass fraction above 10%, the extinction limit of smouldering changes only slightly and approaches a minimum value of 0.08 ± 0.01

g/m^2·s, which could be defined as the minimum oxygen supply rate to sustain a smouldering propagation. Note that the minimum value of oxygen supply rate may still decrease slightly as the oxygen mass fraction increases above atmospheric value, which needs more verifications in future work. As the oxygen mass fraction further drops below 10%, the minimum oxygen supply rate for (unidirectional) smouldering propagation gradually increases to 0.25 ± 0.05 g/m^2·s at X_{O_2}=2%.

Based on Eq. (5.1), we have an empirical correlation between the minimum oxygen supply rate and oxygen level as

$$\dot{m}''_{O_2,min} = \rho_g Y_{O_2} U_{min} \approx \begin{cases} \dfrac{0.08 Y_{O_2}}{Y_{O_2} - MOC} & \text{(unidirectional)} \quad (5.2a) \\ \dfrac{0.08 Y_{O_2}}{Y_{O_2} - MOC} + 2.5 Y_{O_2} & \text{(bidirectional)} \quad (5.2b) \end{cases}$$

where MOC = 1.5 ± 0.5% for the test peat fuel, and R^2 of the fitting is above 0.9 because the difference between oxygen volume and mass fractions are relatively small ($X_{O_2} \approx Y_{O_2}$).

For the boundary between bidirectional and unidirectional smouldering propagation modes, the limiting oxidiser flow velocity also gradually increases with the decreasing oxygen concentration, as shown in **Fig. 5-3**. Such a boundary is almost parallel to the lower boundary of the extinction limit with a constant gap of about 2 mm/s. It is possible that a minimum flow residence time is required to enable a bidirectional smouldering propagation. On the other hand, as the oxygen concentration decreases, both the limiting value of the oxygen supply rate and the gap of the unidirectional-propagation regime decrease, see **Fig. 5-3b**.

5.2.3 Mass loss and smouldering temperature

In addition to the oxygen limits of smouldering, the mass losses and peak smouldering temperatures are also summarized in **Fig. 5-5**, which may help understand the near-limit smouldering behaviour and extinction limits of smouldering combustion. **Fig. 5-5a** summarises all mass-loss fractions, where solid, semi-solid, and hollow symbols indicate bidirectional propagation, unidirectional propagation, and extinction cases, respectively.

First of all, the mass loss during the forced ignition process is quantified, which is around 9.0% (24.3 g out of 270 g). Afterward, the mass loss with different flow conditions can be divided into three regions with different propagation modes.

For the bidirectional propagation, a larger mass loss of over 70% was obtained. As discussed in **Section. 5.2.2** and illustrated in **Fig. 5-2**, the occurrence of bidirectional smouldering propagation is caused by excess oxygen supply. After the test, only a thin ash layer was observed at the bottom of the reactor, thus resulting in a larger mass loss close to the OC of fuel (~ 97%). Comparatively, the unidirectional smouldering propagation can consume 35-70% of the fuel mass. Because the oxygen supply is relatively limited, a layer of virgin unburned fuel remains after extinction, resulting in a lower mass loss. Also, the range of mass loss fraction for unidirectional propagation increases with the X_{O_2}, showing a similar trend to the oxygen supply rate in **Fig. 5-3b**. Finally, for cases of no smouldering propagation, a mass loss of 10-35% could still be achieved. The additional mass loss beyond ignition is caused by a weak char oxidation process that could still survive in the preheated ignition regions. However, due to the lack of oxygen, such a smouldering front could not propagate out (i.e., local burning only).

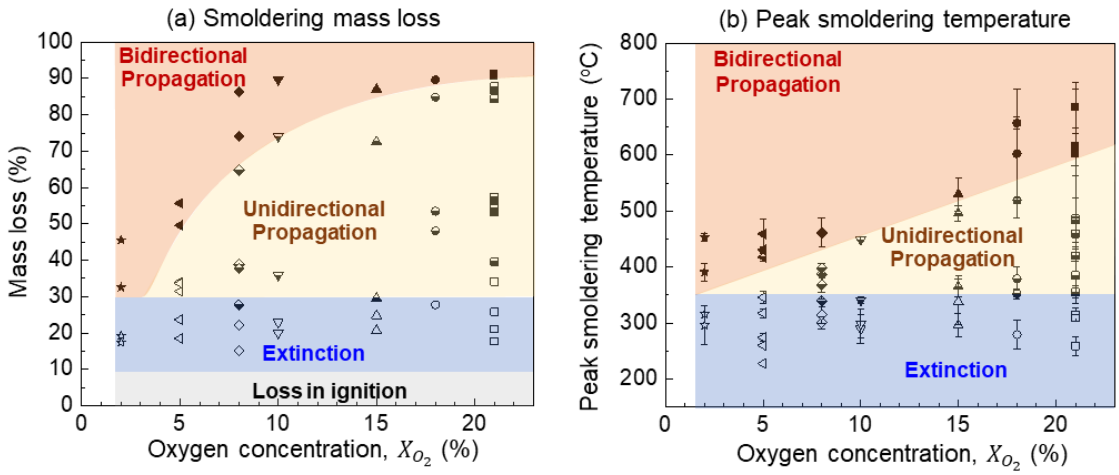

Fig. 5-5 Mass loss **(a)** and the peak temperature **(b)** during different smouldering propagation modes.

Fig. 5-5b shows the effect of flow velocity and oxygen concentration on the peak smouldering temperature. For this organic peat soil, the maximum smouldering temperature is about 700 °C, which is close to the literature values (Huang et al. 2016; Lin et al. 2020b; Lin and Huang 2021). Moreover, as the oxygen concentration or internal flow

velocity increases, the smouldering temperature increases. For example, given an oxygen concentration of 18%, as the flow velocity increases from 0.4 mm/s to 4.4 mm/s, the smouldering temperature increases from 352 ºC to 658 ºC. It is because a stronger oxygen supply can lead to a stronger char oxidation process.

On the other hand, as X_{O_2} and U decrease, the smouldering temperature gradually decreases. Eventually, at the extinction limit, there is a global minimum smouldering temperature of about 300 ºC, regardless of the oxygen concentration and flow velocity. Such a minimum is close to the threshold temperature for char oxidation found in the TGA and similar to the literature data (Huang and Rein 2019; Lin and Huang 2021).

5.2.4 Analysis of minimum oxygen supply

To scientifically explain the relationship between U_{min}, $\dot{m}''_{O_2,min}$ and oxygen fraction (X_{O_2} or Y_{O_2}), a simplified energy conservation equation is applied to a propagating smouldering front, as shown in **Fig. 5-6**. At the extinction limit, the heat generated from the net heterogenous smouldering reactions ($\dot{q}''_{sm}$) should just balance the heat loss from water evaporation ($\dot{q}''_{MC}$), internal flow convection ($\dot{q}''_{conv}$), and environmental heat losses ($\dot{q}''_{e}$) such as cold walls as

$$\dot{q}''_{sm,min} = \dot{q}''_{MC} + \dot{q}''_{conv} + \dot{q}''_{e} \tag{5.3}$$

where the minimum oxidation heat generated is

$$\dot{q}''_{sm,min} = \dot{m}''_{O_2,min}\Delta H_{ox} = \rho_g (UY_{O_2})_{min}\Delta H_{ox} \tag{5.4}$$

where ρ_g is the density of oxidiser flow, and ΔH_{ox} is the heat of oxidation. Therefore, we can derive the minimum oxidiser flow velocity as

$$U_{min} = \frac{\dot{q}''_{MC} + \dot{q}''_{conv} + \dot{q}''_{e}}{\rho_g Y_{O_2}\,\Delta H_{ox}} \propto \frac{1}{Y_{O_2}} \tag{5.5}$$

which shows that the minimum gas flow velocity is inversely proportional to the oxygen concentration ($X_{O_2} \approx Y_{O_2}$). Thus, the trend of experimental data in **Fig. 5-3a** is successfully explained.

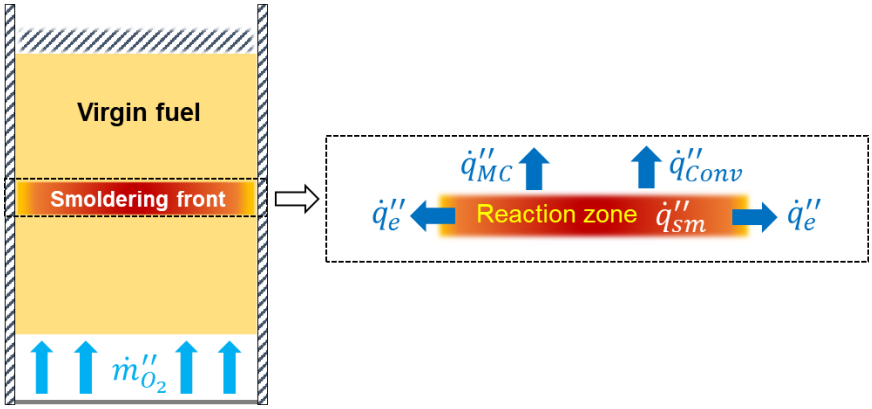

Fig. 5-6 Schematics for energy conservation in propagating smouldering front.

Further reorganising the energy equation, the minimum oxygen supply rate can be expressed as

$$\dot{m}''_{O_2,min} = U_{min}\rho_g Y_{O_2} = \frac{\dot{q}''_{MC} + \dot{q}''_{conv} + \dot{q}''_{e}}{\Delta H_{ox}} \tag{5.6a}$$

As the oxygen concentration decreases, the required internal flow velocity increases significantly (**Fig. 5-3**), and its convective cooling ($\dot{q}''_{conv}$) becomes important (Incropera 2007), as

$$\dot{q}''_{conv} = h(T_{sm} - T_\infty) = Nu\left(\frac{k}{D}\right)(T_{sm} - T_\infty) \tag{5.7}$$

$$Nu \propto Re^m Pr^n \propto (UD/\nu)^m (\nu/\alpha)^n \propto U^m \tag{5.8}$$

where h is convective heat transfer coefficient, T_∞ is ambient temperature, D is the pore size, ν is kinematic viscosity, α is thermal diffusivity, and $0 < m < 1$ (Wang *et al.* 2022a). In other words, the convective cooling of the internal flow also increases with the flow velocity, which becomes significant for limiting cases with low oxygen concentration and large internal flow rate. Thus, with low oxygen concentration and large oxidizer flow rate, the minimum oxygen supply rate can be described as

$$\dot{m}''_{O_2,min} = U_{min}\rho_g Y_{O_2} \propto \dot{q}''_{conv} \propto U_{min}^m \propto \left(Y_{O_2}\right)^{\frac{m}{m-1}} \quad (Y_{O_2} < 10\%) \tag{5.6b}$$

Specifically, with $m = 0.5$, we have $U_{min} \propto 1/Y_{O_2}^2$ and $\dot{m}''_{O_2,min} \propto 1/Y_{O_2}$. Therefore, the minimum oxygen supply rate increases with the flow velocity and decreases with the oxygen concentration. This successfully explains the experimental trend in **Fig. 5-3b**,

when Y_{O_2} is smaller than 10%.

On the other hand, as the oxygen mass flux further increases, the required flow velocity will gradually decrease (see **Fig. 5-3a**). Eventually, the minimum required flow velocity will be tiny, so the convective heat loss becomes negligible as

$$\dot{m}''_{O_2,min} = \frac{\dot{q}''_{MC} + \dot{q}''_{conv} + \dot{q}''_{e}}{\Delta H_{ox}} \approx \frac{\dot{q}''_{MC} + \dot{q}''_{e}}{\Delta H_{ox}} = \text{ const.} \quad (Y_{O_2} \geq 10\%) \qquad (5.6c)$$

As a result, the minimum oxygen supply rate approaches a constant if the fuel condition (e.g., moisture) and reactor configurations are fixed. This well explains the $\dot{m}''_{O_2,min} =$ 0.08 g/m^2·s found in the experiment when the oxygen mass fraction is larger than 10% (see **Fig. 5-3b**).

Eq. (5.6c) also indicate that the value of this minimum oxygen supply rate changes with the fuel. For example, the ΔH_{ox} depends on the fuel type and chemistry, the thermal conductivity of the fuel bed changes the $\dot{q}''_{e}$, and a higher oxygen supply rate is expected due to the increases in $\dot{q}''_{MC}$. Therefore, additional measurements are needed for different fuel types and fuel-bed conditions to form a database that can help evaluate and rank their smouldering fire hazards.

5.3 Conclusions

In this chapter, we experimentally quantify the limiting oxygen supply to sustain different smouldering propagation modes. After ignition in the middle of the fuel bed, by increasing the flow velocity, smouldering transitions from the unidirectional (opposed) propagation to the bidirectional (opposed + forward) propagation. The minimum oxidizer flow velocities to sustain both modes of propagation decrease as the oxygen concentration increases. The minimum oxygen supply rate for stable smouldering propagation decreases with the oxygen concentration and approaches a critical value of 0.08 g/m^2·s at ambient oxygen level. Moreover, smouldering is found to survive at an extremely low oxygen concentration of 2%, so the value of minimum oxygen concentration (if exists) is even smaller.

As the oxygen concentration and oxidizer flow velocity increase, both the mass loss and peak smouldering temperature increase. Meanwhile, the minimum smouldering temperature is found to be around 300 ºC, independent of the oxygen supply conditions. A simplified heat transfer analysis successfully explains the relationship between the minimum oxygen supply rate and oxygen concentration of smouldering propagation. Future numerical simulations are needed to reveal the underlying physical and chemical process of smouldering propagation under different flow conditions. This work provides vital information about the persistence of smouldering propagation and underground peat fire.

CHAPTER 6 Modelling oxygen thresholds: the role of fuel properties and environmental conditions

6.1 Introduction

Smouldering, characterized by its slow, low-temperature, and flameless nature, is one of the most persistent types of combustion phenomena (Ohlemiller 1985; Rein 2013; Rein et al. 2016; Torero et al. 2020). This intricate process is sustained when oxygen molecules directly attack the hot surface of reactive porous media, involving a multitude of elementary chemical reactions coupled with complex heat-and-mass transfer mechanisms (Anca-Couce et al. 2012; Song 2022). Smouldering combustion exhibits a dual nature, presenting both destructive and constructive potentials. On the one hand, it poses catastrophic risks to natural environments such as peatlands, coal seams, and forest litter layers (Rein 2013; Song and Kuenzer 2014; Qin et al. 2022a; Yang et al. 2024a), and serves as a primary contributor to residential fires (Yang et al. 2020; Mitchell et al. 2023). On the other hand, well-controlled applied smouldering processes offer promising avenues for syngas production (Toledo et al. 2023), waste remediation (Rashwan et al. 2021a), and pollution control (Li et al. 2023), playing an important role in the context of our increasing attention to resources, energy, and environment. Therefore, gaining a deeper understanding of the fundamental principles of smouldering combustion is crucial.

Smouldering combustion is governed by the competition between oxygen supply and heat loss (Ohlemiller 1985). Previous studies have explored the effects of heat loss on the smouldering propagation through both experimental (Lin and Huang 2021; Rashwan et al. 2021a) and numerical approaches (Rashwan et al. 2021b), providing a necessary foundation for hazard mitigation and optimization of industrial applications. Oxygen also plays a crucial role in heterogeneous oxidations, releasing heat to balance endothermic processes including pre-heating, drying and pyrolysis reactions, as well as environmental cooling (Decker and Schult 2004). Consequently, the oxygen threshold and smothering limit of smouldering combustion are highly important for determining the criteria of smouldering ignition, propagation, and extinction (Yang et al. 2019; Richter et al. 2021). However, our understanding of the oxygen threshold (smothering limit) of self-sustaining smouldering and the underlying mechanisms remains relatively limited.

In the literature, scattered studies have examined the LOC of smouldering combustion of different biomass fuels under various conditions, including external wind or quiescent ambient environments. These studies have yielded disparate results, with reported LOC

values ranging from 10% (Hadden et al. 2013), 13% (Huang and Rein 2016a), and 16% (Belcher et al. 2010) for peat, 4% (Richter et al. 2021) for wood, to 13.5% (Kadowaki et al. 2021) for cellulosic material. However, as the diffusion of oxygen from the surroundings cannot be completely isolated in the aforementioned studies, the precise amount of oxygen that penetrated the porous fuel remained undetermined. To fill this gap, in our recent study (Qin et al. 2022b), we developed a tubular smouldering reactor capable of precisely controlling the flow of oxidizer with a prescribed oxygen concentration and flow rate through the porous media. We found that, for high organic porous fuel (e.g., peat), the LOC could be < 2%, and the minimum internal oxygen supply rate was approximately 0.08 ± 0.01 g/m^2·s. However, the oxygen threshold of pine needles, a more representative forest litter prone to smouldering combustion, has not yet been reported. Meanwhile, LOC for smouldering of porous fuels is complex that would be influenced by many factors such as the inherent physicochemical properties of the fuels (e.g., density, MC, and IC) and environmental conditions (e.g., system heat loss, environment temperature, and even gravity), requiring further investigations (Bar-Ilan et al. 2004; Huang and Rein 2019; Lin et al. 2022a).

Pine needle litter is a common wildland fuel in coniferous forests prone to fires (Dupuy 1995; Santoni et al. 2014). It often forms highly porous fuel beds that can ignite a smouldering fire with a lower energy input and subsequently transition to flaming fires (StF) under natural wind, posing significant hazards (Thomas et al. 2014; Qiao et al. 2024). Despite many studies have experimentally and numerically investigated the pine needles and other litters (e.g., duff and mulch) in terms of smouldering kinetics (Benkorichi et al. 2017), smouldering ignition (Wang et al. 2017b), smouldering propagation (Morvan and Larini 2001; Valdivieso and Rivera 2014; Yang et al. 2024b), flammability (Thomas et al. 2014), and StF (Smouldering to Flaming) transition (Gong et al. 2024; Qiao et al. 2024), the role of oxygen supply in their near-limit smouldering combustion is still poorly understood. For the first time, our previous work experimentally investigated the minimum oxygen supply rate of smouldering propagation over pine needle beds and quantified the effects of bulk density (Qin et al. 2024), but the effect of other physicochemical properties of the fuels and environmental conditions are still unknown. Furthermore, to the best of the authors' knowledge, no computational model has been estab-

lished specifically for the oxygen threshold and smothering limit of smouldering combustion with forced internal oxygen supply, highlighting a huge knowledge gap.

To address these knowledge gaps, this chapter built a 1-D computational model for smouldering combustion based on Gpyro (Lautenberger and Fernandez-Pello 2009) and previously developed 5-step smouldering kinetics of smouldering pine needles (Rana et al. 2023). Oxygen was supplied as a forced internal oxidizer flow within porous fuels. Numerical simulations were performed to investigate the oxygen threshold or smothering limits specifically for smouldering combustion of pine needle beds as well as smouldering dynamics under different oxygen supply and then verify the previous experiments and theoretical analysis. Moreover, the effects of fuel properties (MCs and bulk densities) and environmental conditions (oxygen concentrations and ambient temperatures) on the smouldering dynamics were also explored.

6.2 Computational results and discussions

6.2.1 Base cases and model validation

Herein, two base cases (successful and failed self-sustaining smouldering propagation) were first compared between the experiment and the simulation, where the pine needle fuel beds were controlled at $\rho_b = 120 \pm 20\ \mathrm{kg/m^3}$ and MC = 5%, and oxygen mass fraction was set at Y_{O_2} = 23%. The example temperature profiles of successful and failed smouldering propagation from experimental and simulation results are compared in **Fig. 6-1**. **Fig. 6-1a** shows the experimental measurements under an internal airflow velocity of 2.6 mm/s, and the simulated temperature profile is presented in **Fig. 6-1b** for comparison. In general, considering the complex nature of the smouldering process, a satisfactory agreement can be observed between computational predictions and experimental data. As depicted in **Fig. 6-1 a-b**, a two-stage opposed-to-forward smouldering process was observed, consistent with our findings in previous works (Huang and Rein 2019; Qin et al. 2022a). In the opposed-to-forward propagation, upon ignition from the top, a robust reaction front was established, then a rapid downward propagation was observed, and the reaction front reached the bottom in 1 h. Subsequently, the smouldering front started to spread upward concurrently with the oxidizer flow, which was dominated by the char

oxidation process with a longer duration and a higher temperature. After burnout, from the experimental residues, it was observed that the char and ash formed a fragile structure that didn't collapse naturally. It reduced the surface regression during the burning process, which was different from other smouldering fuels such as peat or tiny wood chips (Huang and Rein 2017). When the oxygen supply rate was decreased to below the smouldering limit, no propagation occurred in experiments and simulations, as exemplified in **Fig. 6-1 (c-d)**. In those scenarios, the insufficient oxygen supply was not able to support the exothermic oxidations that were necessary for the endothermic drying and pyrolysis process. Therefore, after ignition, the system temperatures at all locations drop without any fluctuations.

Note that the "0-cm" probe in **Fig. 6-1a** did not read a high temperature instantly like that in **Fig. 6-1b** because of the use of an additional "1-cm ignition layer" on the top of the tested fuel bed during experiments (see **Section 6.3.2**). Moreover, there was a clear fluctuation in the temperature of the forward spread during experiments (**Fig. 6-1a**), possibly due to: (1) non-uniform physicochemical properties of the fuel bed, (2) an uneven smouldering front under oxygen-limited scenarios and (3) random local fuel collapses, which were inevitable in experiments and difficult to be included in the numerical model. Furthermore, the establishment of the model involved many assumptions. For example, the input of physical properties of fuels and their temperature variations were simplified to constants. Also, this model didn't consider the microscopic structures of fuel particles, as well as the random local collapses of char and ash during the propagation of smouldering combustion (Lin et al. 2022a). In addition, the "O_2 leakage" induced by the uneven distribution of fuel was impossible to be included in the model (Qin et al. 2024). Therefore, it is impossible to completely match the experimental and simulated results, especially the time-evolution temperature profile (Lin et al. 2022a). Nevertheless, the shape of the predicted temperature profile, peak temperature, and fire spread duration are consistent with the experimental observations. Driven by coupled thermal, chemical, and transport processes, it is difficult to define a single quantitative spread rate. Further studies are required to compare the overall spread rate between experiments and simulations.

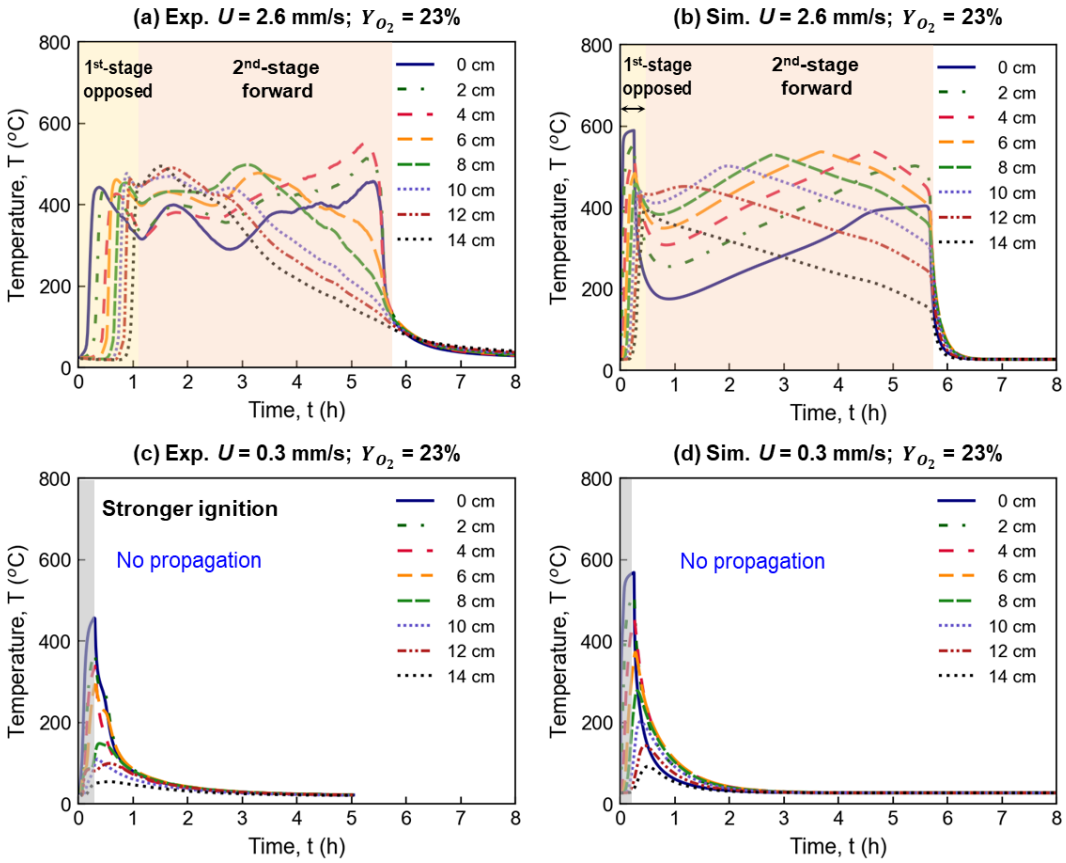

Fig. 6-1 Comparisons of temperature profiles from experimental measurement and simulations results. Successful two-stage smouldering propagation under flow velocity of 2.6 mm/s **(a-b)**; and failed smouldering propagation under insufficient oxygen supply of 0.3 mm/s **(c-d)**.

Moreover, **Fig. 6-2** further summarizes the simulated peak temperatures and burning durations of smouldering (dash lines), and the experimental results (markers) are plotted for comparison. In general, simulation showed satisfactory agreement with experimental results, and our model is therefore further validated. Notably, the effects of oxidizer flow velocity on the peak temperatures and burning durations were well captured by the model; that is, as the airflow velocity increased, the smouldering temperature increased while the burning duration decreased. It is due to more heat released from oxidation reactions with better oxygen availability, leading to a higher reaction rate. Additionally, the behaviour that the same fuel can burn for a longer duration under limited oxygen supply also corresponds to the phenomenon where smouldering fires in deep underground environments can persist for weeks and even months (Rein 2013; Qin et al. 2022a). These smouldering dynamics in near-limit conditions require further research to be revealed.

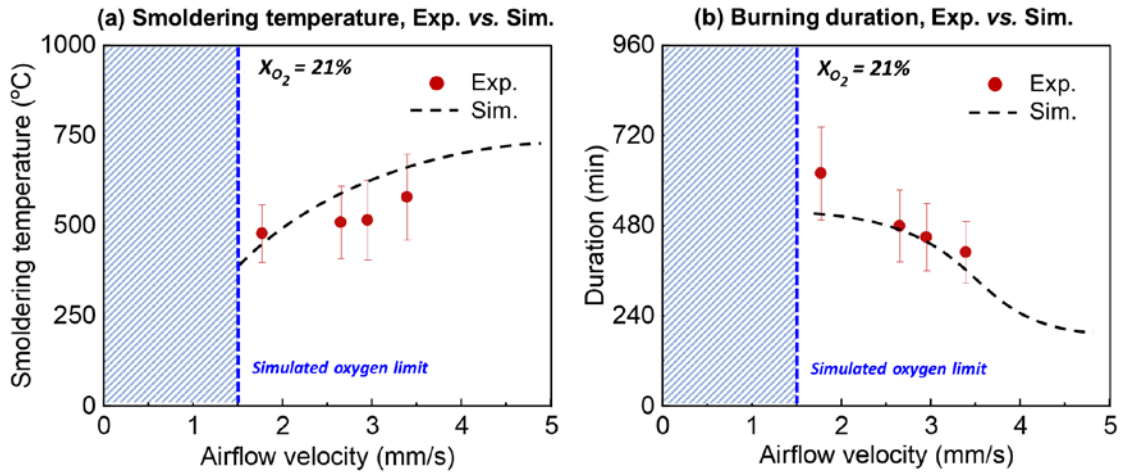

Fig. 6-2 Comparison of experimental and simulation data on smouldering peak temperature **(a)**; and burning duration **(b)**. The satisfactory agreement validates the capability of computational model.

Referring to both **Fig. 6-1** and **Fig. 6-2**, the experiment and simulation results exhibited a strong agreement in terms of propagation mode, spread rate, smouldering temperature, and burning duration. This consistency validates the capability of our model to accurately simulate the propagation and extinction of smouldering combustion driven by oxygen supply in porous pine needle beds.

6.2.2 Roles of oxygen concentrations

Following the validated model and base cases, we further explored the oxygen thresholds or smothering limits by adjusting the Y_{O_2} of internal oxidizer flow. **Fig. 6-3a** describes the simulated boundary trendlines for the smothering limits of smouldering combustion, i.e., the U_{min} to sustain smouldering under various Y_{O_2}. First, the LOC was found to be 3%, below which smouldering was not able to survive, irrespective of the flow velocity. Afterwards, the predicted required flow velocity increased with the decreasing oxygen mass fraction, which was consistent with the trend shown in our previous experimental work on smouldering peat (Qin et al. 2022b). For example, the predicted required flow velocity increased from 1.6 mm/s to 12 mm/s, as Y_{O_2} decreased from 23% to 5%.

Based on previous work (Bar-Ilan et al. 2004; Qin et al. 2022b), at the extinction limit, the heat generated from the net heterogeneous smouldering reactions ($\dot{q}''_{sm}$) should just balance the $\dot{q}''_{MC}$, $\dot{q}''_{conv,in}$, and $\dot{q}''_{e}$ as

$$\dot{q}''_{sm,min} = \dot{q}''_{MC} + \dot{q}''_{conv,in} + \dot{q}''_{e} \quad (6.1)$$

By further organizing Eq. 6.1, we obtain

$$\dot{q}''_{sm,min} = S_{sm}\rho_w \Delta H_{ev} MC + \rho_g c_{p,g} U(T_{sm} - T_\infty) + (h_r + h_c)(T_{sm} - T_\infty) \quad (6.2)$$

where S_{sm} and T_{sm} refers to smouldering propagation rate and temperature. For simplicity, the radiative heat loss is linearized by using the radiation heat transfer coefficient (h_r) (Incropera 2007). On the other hand, the minimum oxidation heat generated can be described as

$$\dot{q}''_{sm,min} = \dot{q}''_{ox} = \dot{m}''_{O_2,min} \Delta H_{ox} = \rho_g (U Y_{O_2})_{min} \Delta H_{ox} \quad (6.3)$$

where ρ_g is the density of oxidizer flow, and ΔH_{ox} is the heat of smouldering oxidation. Therefore, the minimum oxidizer flow velocity and can be derived as

$$U_{min} = \frac{S_{sm}\rho_w \Delta H_{ev} MC + (h_r + h_c)(T_{sm} - T_\infty)}{\rho_g Y_{O_2} \Delta H_{ox} - \rho_g c_{p,g}(T_{sm} - T_\infty)} \propto \frac{1}{Y_{O_2} - C} \quad (Y_{O_2} > 3\%) \quad (6.4)$$

where for a specific fuel with a particular MC and density, S_{sm} and T_{sm} can be regarded as constants at the limiting condition of smouldering propagation (Lin et al. 2022a). $C = \frac{c_{p,g}(T_{sm} - T_\infty)}{\Delta H_{ox}}$ is a constant relying on smouldering and ambient temperatures. Therefore, the minimum gas flow velocity is inversely proportional to the oxygen concentration ($U_{min} \propto \frac{1}{Y_{O_2} - C}$) in Eq. (6.4), and the overall trend of simulated results in **Fig. 6-3a** is successfully explained. Furthermore, the predicted oxygen supply rate was further calculated as $\dot{m}''_{O_2} = \rho_g Y_{O_2} U$, and the results are shown in **Fig. 6-3b**. It is found that $\dot{m}''_{O_2}$ increased from 0.45 g/m^2·s to 0.8 g/m^2·s when Y_{O_2} decreased from 23% to 4%. This trend also agreed well with the trend found in our previous experiments (Qin et al. 2022b).

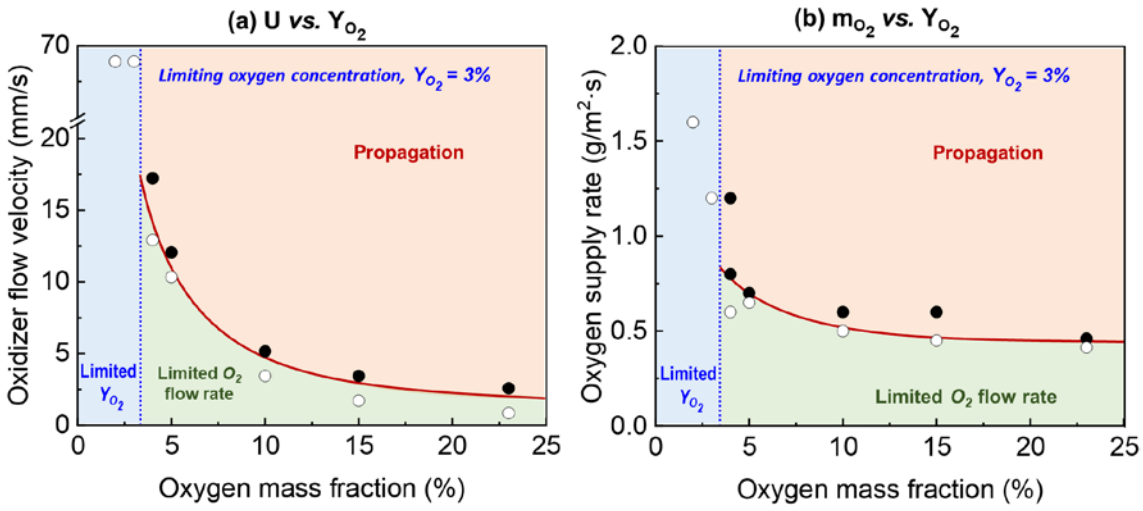

Fig. 6-3 Simulation results and boundary trendlines of U_{min} *vs.* Y_{O_2} **(a)**; m_{O_2} *vs.* Y_{O_2} **(b)**. The solid (●) and hollow (○) mark represents numerical results of propagation and extinction, respectively.

6.2.3 Fuel density, moisture and ambient temperature

Fuel dry bulk density (ρ_{dry}) and MC is expected to vary in applied smouldering systems and wildfire scenarios. More importantly, they were found to play a significant role in the propagation and extinction of smouldering combustion (Huang and Rein 2017). Herein, the sensitivity of the oxygen thresholds or smothering limits to fuel MC was explored by varying MC within a range of 5% and 120% (dry basis). Note that the fuel dry bulk density was controlled as $\rho_{dry} = \rho_{wet}/(1 + \mathrm{MC})$ that the volume expansion from absorbing water can be balanced (Huang and Rein 2017).

Computational results showed that the required airflow velocity was significantly influenced by ρ_{dry} (**Fig. 6-4a**) and MC (**Fig. 6-4b**). On the one hand, as the ρ_{dry} increases, the required airflow velocity was predicted to decrease (**Fig. 6-4a**), well agreeing with previous findings (Qin et al. 2024). For example, when MC is 50%, as the fuel dry bulk density increases from 50 kg/m^3 to 300 kg/m^3, the airflow velocity required for sustaining smouldering was predicted to decrease from about 7 mm/s to 3 mm/s. As the fuel dry bulk density, the effective thermal conductivity of the fuel will increase (Incropera 2007), thus increasing the heat transfer efficiency between the burning zone and virgin fuels and lowering the oxygen required for sustaining smouldering propagation (Qin et al. 2024).

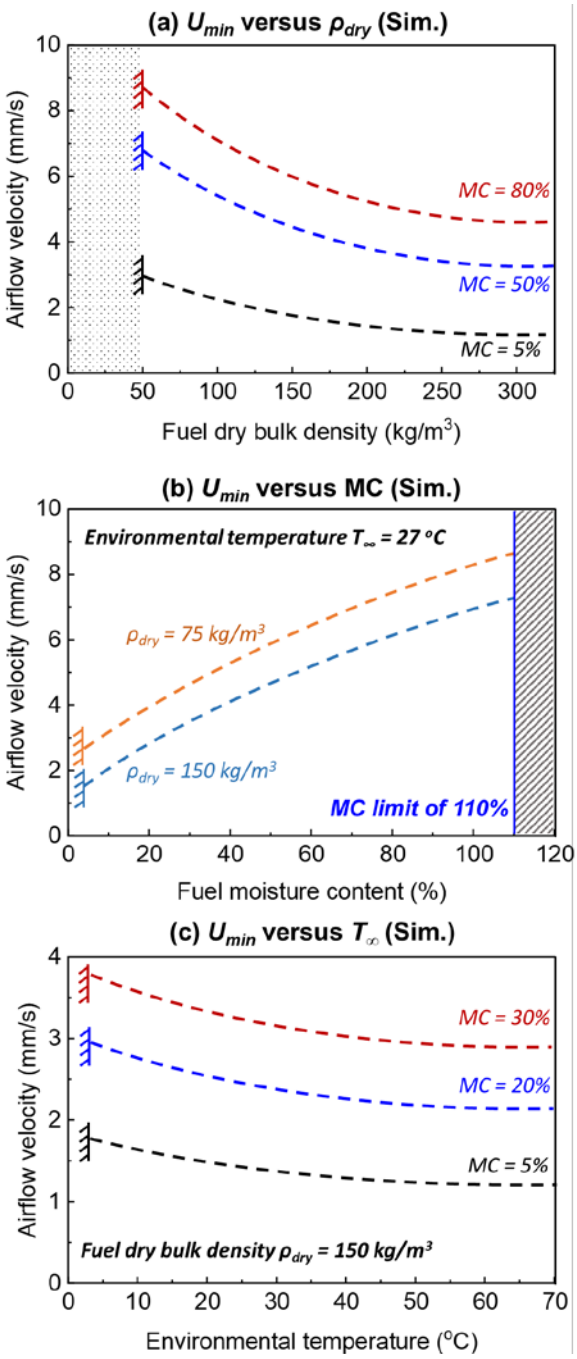

Fig. 6-4 Simulation results of the role of ρ_{dry} **(a)**, MC **(b)**, and T_∞ **(c)** on oxygen threshold of smouldering combustion.

On the other hand, as the fuel MC increases, the required airflow velocity was predicted to increase, as shown in **Fig. 6-4b**. For example, as MC increased from 5% to 50%, the required oxygen supply for high-density pine needles (ρ_{dry} = 150 kg/m^3) rose from about 2 mm/s to about 5 mm/s. This trend can be also explained by Eq. 6.4, where U_{min}

increases as $\dot{q}''_{MC}$ increases; that is, a higher airflow velocity is required to intensity the reactions that release more heats to overcome the heat loss due to the water evaporation. Furthermore, the maximum MC capable of supporting smouldering is about 110% (**Fig. 6-4b**). Beyond this limit, smouldering was not able to be sustained regardless of oxygen supply.

In real fire scenarios, the ambient temperature can be much higher which may lead to a different oxygen threshold. Therefore, the effect of T_∞ was also investigated and summarized in **Fig. 6-4c**. In order to focus on the T_∞, the process of water freezing caused by sub-zero temperature was out of the scope of this study. As a result, the temperature range under investigation was limited to 0-70 ºC. Predicted results showed that the required airflow velocity decreases as T_∞ increases. For example, given a fixed fuel MC of 5%, as the ambient temperature increases from 10 ºC to 70 ºC, the predicted required airflow velocity decreases from about 1.7 mm/s to about 1.4 mm/s. This could be also explained by Eqs. 6.2-6.3, where the convective and radiative heat loss will decrease as T_∞ increases, leading to a lower airflow velocity required for self-sustaining smouldering propagation.

6.2.4 Smouldering temperature and spread rate

Smouldering temperature (T_{sm}) and spread rate (S_{sm}) are two key parameters that describe the smouldering behaviours and reflect the intensities of reactions and the rates of fuel consumption. Therefore, **Fig. 6-5** and **Fig. 6-6** further compare the effects of MC and bulk density on the T_{sm} and S_{sm}, and each curve was controlled to have the same $\dot{m}''_{O_2}$. First of all, at the smothering limit, the minimum smouldering temperature and propagation rate were predicted to be around 300 ºC and 0.5 cm/h, and the predicted T_{sm} and S_{sm} both increase as $\dot{m}''_{O_2}$ increases, agreeing well with the literature (Yermán et al. 2016; Zhang et al. 2023; Song et al. 2024). By considering a 1-step global smouldering reaction, the smouldering burning flux can be described as

$$\dot{m}''_F = \rho S_{sm} = \frac{\dot{m}''_{O_2}}{\nu} \propto T_{sm} \tag{6.5}$$

where ν is the stoichiometric factor. The decline in peak temperature with increasing MC is primarily interpreted as a result of evaporative cooling, where latent heat absorp-

tion during water vaporization limits further temperature rise. A more detailed mechanistic investigation will be pursued in future work. By further reorganizing Eq. 6.5, we obtain:

$$S_{sm} = \frac{\dot{m}''_F}{\rho} = \frac{\dot{m}''_{O_2}}{\nu\rho} \tag{6.6}$$

Therefore, as the $\dot{m}''_{O_2}$ increases, the reaction rate of smouldering combustion increases, leading to a higher smouldering temperature and spread rate.

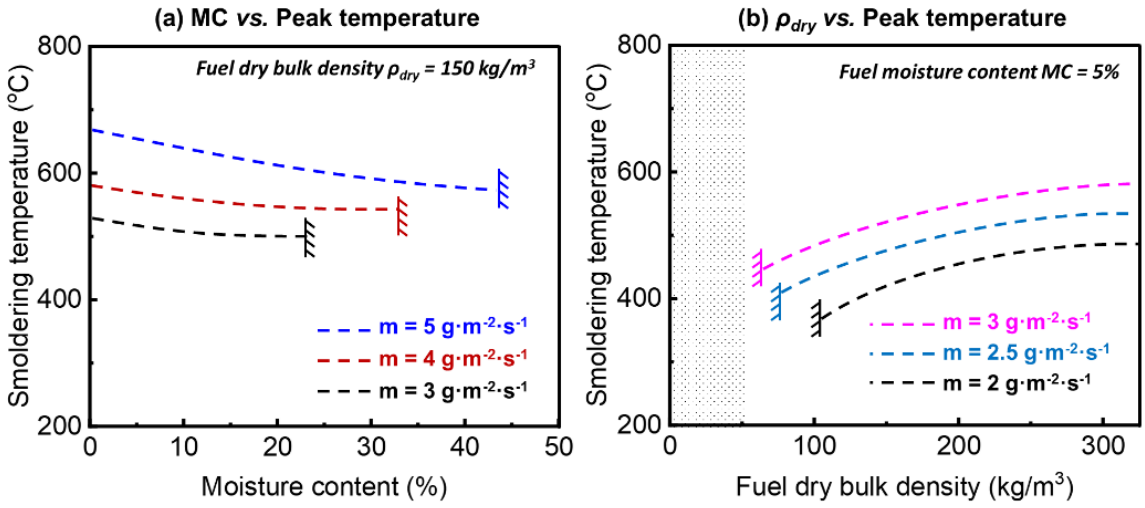

Fig. 6-5 The peak temperature as a function of fuel MC **(a)**, and ρ_{dry} **(b)**. All curves are trend lines with fixed oxygen supply of simulated results.

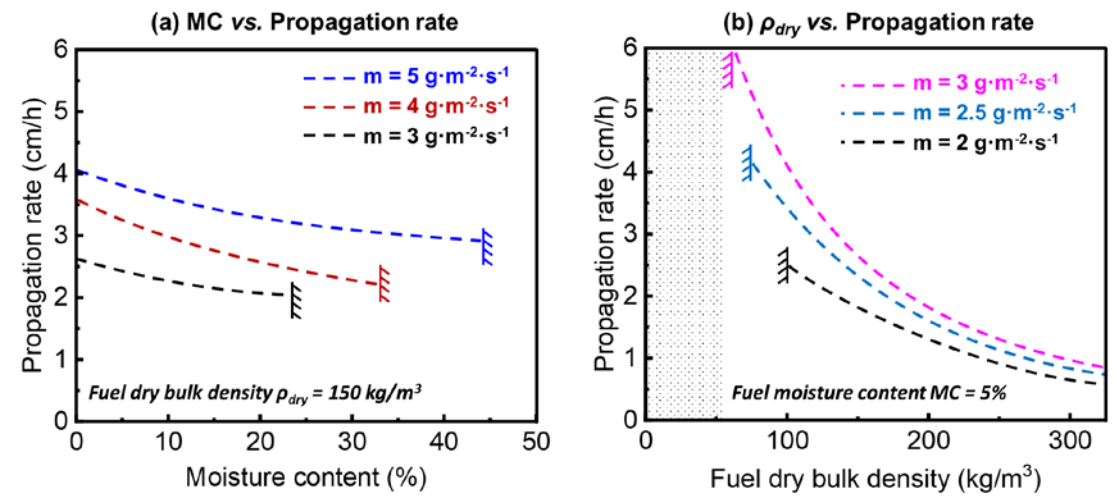

Fig. 6-6 The smouldering propagation rate as a function of fuel MC **(a)** and ρ_{dry} **(b)**. All curves are trend lines with fixed oxygen supply of simulated results.

Furthermore, **Fig. 6-5 a-b** shows the smouldering peak temperature will decrease with the increase of MC or the decrease of dry bulk density in pine needle beds, while **Fig. 6-6** shows the predicted smouldering propagation rate will decrease as the MC and bulk density increase. On the one hand, as the MC increases, extra heat is required to dry the fuel before ignition and propagation, leading to a lower smouldering temperature and propagation rate. On the other hand, if the density of fuel increases, both γ and k_i will decrease. This leads to a higher smouldering temperature but a lower propagation rate as the heat is easier to accumulate and more difficult to dissipate within the fuel due to a lower thermal conductivity (Qin et al. 2024), consistent with the trend shown in **Fig. 6-5** and **Fig. 6-6**. Moreover, it is noteworthy that the smouldering temperature is more sensitive to the oxygen supply rather than MC and bulk density, agreeing with previous studies (Huang and Rein 2017). For example, when the air flow rate was stabilized at 3 g/m^2·s, as the MC was reduced from 20% to 5%, the smouldering temperature was only decreased by 20 ºC. However, if the air flow rate was increased from 3 g/m^2·s to 5 g/m^2·s, the smouldering peak temperature was significantly increased by 100 ºC. Nevertheless, more fundamental studies are still needed to unravel the underlying mechanisms governing the smouldering propagation.

6.3 Conclusions

In this chapter, we employed numerical simulations to investigate the oxygen supply thresholds or smothering limits of smouldering combustion of pine needle beds. The model integrating heat-and-mass transfer and 5-step heterogeneous chemistry was established using open-source code Gpyro and was successfully validated through well-controlled experiments. Subsequently, the required oxidizer flow velocity or oxygen supply rate was predicted to increase as the oxygen concentration decreased. Notably, the predicted limiting oxygen concentration specially for smouldering combustion was about 3%, agreeing well with both the experimental observations and theoretical analysis.

Then, the sensitivity of the oxygen thresholds or smothering limits to fuel density, MC and environmental temperature was further explored. Computational results revealed

that the required airflow velocity for smouldering combustion increased as the fuel density or environmental temperature decreased. However, the required airflow velocity was predicted to increase as the MC increased, and the predicted maximum MC capable of supporting smouldering was about 110%.

Finally, the smouldering peak temperature was predicted to decrease as the MC increased or the bulk density decreased, while the predicted smouldering propagation rate was predicted to decrease as the MC and bulk density increase, consistent with the theoretical analysis. At the smothering limit, the minimum smouldering temperature and propagation rate were predicted to be around 300 ^{o}C and 0.5 cm/h.

CHAPTER 7 Prediction of emission factors of wildland fires using machine learning methods

7.1 Introduction

It is estimated that nearly half of the global population (3.5 billion people) reside in WUI areas (Schug et al. 2023). The accumulation of abundant fuels, including buildings, furniture, vehicles, and vegetation has resulted in significant fire risks. WUI fires can lead to severe direct losses of human life and habitat. More importantly, fire emissions from WUI fires may pose long-term adverse impacts on human health and the environment.

EFs are important characterization parameters to estimate total fire emissions (Akagi et al. 2011). However, most current studies on EFs are limited to very few experimental data, and estimations often rely on a rough average value. Accurate total emission estimation requires deeper insights into how factors such as fuel type and properties influence fire emission characteristics. But to date, no models have been developed to account for these factors in predicting EFs, which is a critical knowledge gap.

In recent years, machine learning (ML) has been widely applied across research fields and industries. These models have played an important role in fire research. For example, ANN methods has been used to predict the thermal decomposition properties (Chen et al. 2023c) and fire heat release rate (Wang et al. 2022b), demonstrating their ability to uncover complex and hidden correlations among fire-related variables. However, fire emission characteristics are also important and highly complex, and no existing physical models can fully explain or predict EFs. In this context, ML offers a possibility to predict EFs from fuel physical properties.

This paper aims to compile a dataset of WUI fire EFs from the literature, including information on fuel type, fuel density, combustion modes (flaming or smouldering), apparatus, and test scale. Based on this database, an ANN model is established to correlate physicochemical parameters with EFs and predict CO_2, CO, and TPM emissions from common WUI fuels. This study enhances the understanding of WUI fire emissions, their atmospheric impacts, and the public health effects associated with PM exposure.

7.2 Preliminary results and discussions

7.2.1 Data collection

Firstly, this study compiles the EFs of typical WUI fuels in the literature. At the very first stage, only EFs of CO_2, CO, and TPM are focused on. The reasons are: (1) CO_2, CO, and TPM are among the most fundamental and important fire emissions, making them suitable targets for prediction and analysis; (2) There are limited number of studies providing CH_4 and $PM_{2.5}$ emission data, resulting in an insufficient dataset for training ML models. Other emissions, such as NO, NO_x and total hydrocarbon (THC), are also collected for further investigation, but are not used for current model. The number of valid EF data collected for each species is shown in **Table 7-1**.

Table 7-1 Number of valid EF data points collected for each species from literature.

Emission	**CO_2**	**CO**	**TPM**	NO	NO_2	NO_x	HCN	HCl	SO_2	THC
Amounts	**357**	**393**	**186**	48	43	171	175	132	69	72

The input parameters for the model include fuel type, density, combustion mode, test scale, thermal conditions, and oxygen conditions (**Fig. 3-6**). These factors were selected because they represent the key physical and environmental variables influencing fire emissions. Fuel properties, such as type and density, determine combustion efficiency and pyrolysis behaviour, directly affecting emissions. Combustion mode and test scale influence heat transfer, flame behaviour, and the completeness of combustion, which are critical in EF variations. Additionally, thermal conditions and oxygen supply play fundamental roles in controlling reaction kinetics, oxidation efficiency, and pollutant formation. By incorporating these parameters, the model aims to establish a robust correlation between fire conditions and emission characteristics, enabling a more accurate prediction of EFs across different fire scenarios. The detailed ANN structure and training procedure can be found in **Section 3.3**.

7.3.2 MSE loss curves for ML model

Fig. 7-1 presents the loss curves of the ML models for predicting CO, CO_2, and TPM

emissions. The loss decreases consistently across all models, indicating effective learning and convergence. The CO model exhibits a steady decline with minor fluctuations, suggesting some sensitivity to data variability. The CO_2 model starts with a significantly high loss, which drops sharply within the first 50 iterations before gradually stabilizing, reflecting the large numerical variations in CO_2 emission factors. The TPM model demonstrates the fastest convergence, with a smooth decline in loss, suggesting that the underlying relationships in the data are more readily captured. Overall, these trends confirm the models' ability to learn the complex correlations between input features and emission factors. However, the final MSE for three species are still relatively large. The reasons will be discussed in **Section 7.3.4**.

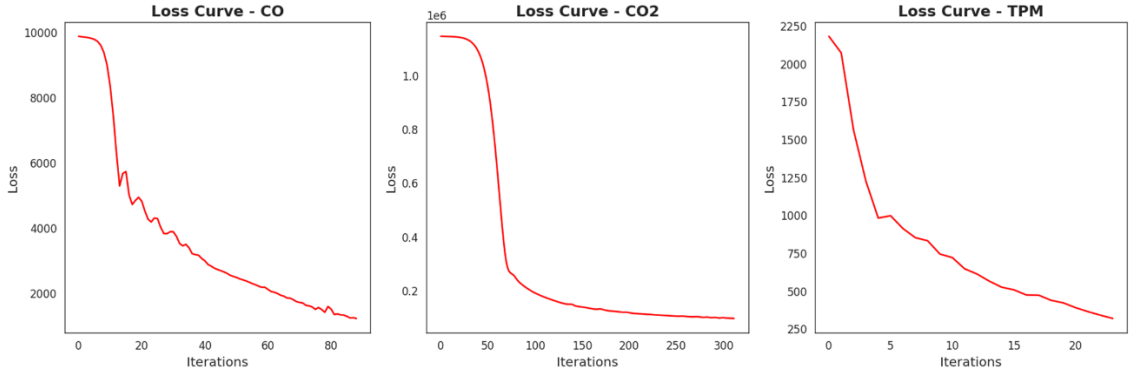

Fig. 7-1 MSE losses for ANN model training and validation.

7.3.3 R^2 *for ANN* model predictions

Fig. 7-2 further compares the predicted value against the true value in the test set of the three emission species. The R^2 values for CO, CO_2, and TPM are 0.56, 0.62, and 0.61, respectively, indicating a reasonable predictive performance. The results suggest that the model effectively captures the underlying relationships between input parameters and emission factors, despite some scatter around the 1:1 reference line (red dashed line). The R^2 values above 0.5 demonstrate that the model explains a substantial portion of the variance in emission factors, making it a useful tool for estimating fire emissions based on given fuel and combustion conditions.

Notably, the prediction errors are generally higher for extreme EF values, especially

under heavy-emission conditions. This is expected given that absolute error often scales with the magnitude of the predicted results, while the relative (percentage) error remains within an acceptable range. Additionally, these high-EF cases are more challenging due to limited training data and increased variability in the combustion environment. Future work will address this by incorporating more high-emission samples and testing uncertainty-aware models to improve predictions under extreme scenarios.

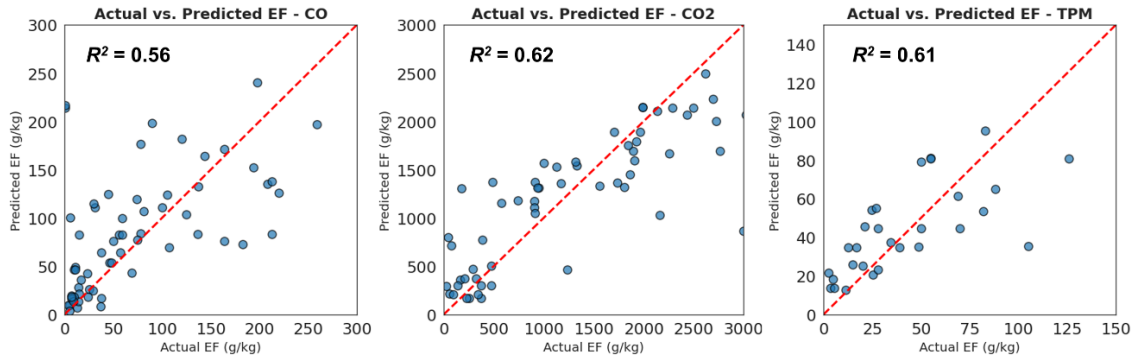

Fig. 7-2 Predicted vs. true values in the test set.

7.3.4 Limitations and future work

Despite the preliminary results demonstrate an acceptable prediction of emission factors, several limitations must be acknowledged:

(1) High variability and uncertainty in fire emission data. Fire emissions inherently exhibit significant variability due to differences in fuel composition, combustion conditions, and environmental factors. These uncertainties introduce challenges in model generalization and predictive accuracy, limiting the robustness of EF estimations.

(2) Limited data availability. The dataset used in this study is constrained by the availability of emission factor data in the literature. Many studies report emissions under specific conditions, leading to data gaps and an uneven distribution of samples across different fire scenarios. Additionally, variations in measurement techniques and the absence of reported error bars further contribute to uncertainties. Improving the dataset size and quality by incorporating more comprehensive and standardized measurements would enhance model reliability.

(3) Potentials for using more ML algorithms. While the ANN model provides reasonable predictions, alternative ML approaches such as random forests, support vector machines, and ensemble learning techniques could be explored to improve performance. A systematic comparison of different models would help identify the most effective approach for capturing complex relationships in fire emission data.

To further enhance the applicability and impact of this research, two key directions are proposed. First, an interactive online tool will be developed, allowing users to input relevant combustion parameters and obtain predicted emission factors using the trained model. This tool would make the model accessible to researchers and policymakers who are working on fire emissions and atmospheric impact assessments. Second, a framework and database submission interface will be established to standardize experimental procedures and facilitate data sharing. By enabling researchers to contribute their experimentally measured emission factors under consistent testing conditions, this initiative would improve dataset quality, ultimately leading to a more robust and accurate predictive model.

7.3 Conclusions

This on-going study developed an ML-based approach to predict EFs of WUI fires, addressing a critical gap in emission estimation methods. A dataset of WUI fire EFs was compiled from the literature, incorporating key influencing factors such as fuel type, density, combustion mode, test scale, thermal conditions, and oxygen supply conditions. An ANN model was trained to establish correlations between these parameters and the EFs of CO_2, CO, and TPM.

The model evaluation demonstrated reasonable predictive performance, with R^2 values of 0.56, 0.62, and 0.61 for CO, CO_2, and TPM, respectively. These results indicate that the model effectively captures underlying relationships between fire conditions and emissions, providing a useful tool for estimating fire emissions when direct measurements are unavailable. However, the study also highlights several limitations, including the inherent variability and uncertainty in fire emission data, limited data availability, and the need for further exploration of alternative ML models to improve prediction accuracy.

CHAPTER 8 Estimating public health impact from 2014-2015 South-east Asia smouldering wildfires

8.1 Introduction

Peat is a carbon-rich organic soil that accumulates substantial amounts of partially decomposed vegetation under anaerobic conditions (Hugron et al. 2013). Peatlands serve as critical terrestrial carbon reservoirs and store approximately one-third of the world's soil carbon (500–600 Gt C), which is comparable to that in global surface vegetation and approaches the size of the atmospheric carbon pool (~850 Gt C) (Ballhorn et al. 2009; Turetsky et al. 2015). In addition to their carbon storage capacity, peatlands contain porous, charring natural fuel that is highly vulnerable to smouldering fires, especially when lowered water tables during extended dry spells, such as those driven by El Niño conditions, expose the peat to drier environments. El Niño events have repeatedly coincided with widespread peat fires in Indonesia, Malaysia, and other parts of South-east Asia, leading to elevated fire activity and recurrent degradation of extensive peatland areas.

Smouldering peat fires in South-east Asia are marked by their exceptional persistence, often burning for weeks or even months within deep peat layers (Rein 2016; Qin et al. 2022a). Unlike flaming combustion, which spreads rapidly at higher temperatures, smouldering occurs at lower temperatures (ranging from approximately 450–700 °C) and propagates slowly through the porous peat matrix. This low-temperature oxidation process is especially difficult to detect and suppress because it often continues underground, away from direct observation, thereby posing significant challenges to effective land management and fire control (Lin et al. 2020b).

Smouldering smoke from peatland fires are chemically distinct and often more hazardous than those from flaming fires (Stockwell et al. 2016; Hu et al. 2018). Due to incomplete oxidation at relatively low temperatures, smouldering releases higher proportions of toxic and health-relevant pollutants, including PM (especially $PM_{2.5}$), CO, VOCs, etc. These emissions are not only detrimental to local air quality but also contribute significantly to regional and global carbon budgets. For instance, the 1997 El Niño-induced peatland mega-fire in Indonesia triggered the transboundary 1997–1998 Southeast Asia haze, affecting 100 million people across five countries and causing an estimated US$4.5 billion in damages (Heil and Goldammer 2001; Page et al. 2002).

More importantly, haze poses severe threats to public health. Elevated concentrations

of $PM_{2.5}$ and other pollutants have been linked to respiratory and cardiovascular morbidity, with hospital admissions rising sharply during prolonged haze periods (Emmanuel 2000; Wu et al. 2021; Lou et al. 2023). Epidemiological evidence indicates that the 1997 Southeast Asian transboundary haze posed acute health risks to 105 million people, mainly in Indonesia, Singapore, Malaysia, Brunei, and Thailand. In South Sumatra, acute respiratory infections increased 3.8-fold from 1996 to 1997 (Hinwood and Rodriguez 2005). Haze pollution was also associated with 16,400 infant and foetal deaths in Indonesia. (Jayachandran 2009).

In this ongoing work, we aim to quantify the public health impact of extensive smouldering peat fires in Southeast Asia. The most recent mega peat fire during the 2014–2015 El Niño event is selected as a case study. We employ two widely used satellite-derived fire emission inventories, GFED4 and GFAS, to represent the magnitude and spatial distribution of peat fire emissions. Compared to earlier studies, which often relied on older or less regionally representative datasets, these inventories offer improved coverage and resolution for Southeast Asian peatlands. The emissions are then integrated into the GEOS-Chem chemical transport model to simulate atmospheric concentrations of $PM_{2.5}$ and other key pollutants across the region. Finally, we apply the updated GEMM-5COD, which has shown improved performance over traditional CRFs, particularly under lower-to-moderate pollution levels, to estimate the excess mortality attributable to peat fire smoke during this period. Although the ANN-based EF model developed in Chapter 7 is not yet incorporated, the current framework already reflects several methodological advancements over previous regional assessments.

8.2 Preliminary results and discussions

8.2.1 Fire-sourced $PM_{2.5}$ concentrations

Fig. 8-1 describes annual averaged fire sourced $PM_{2.5}$ concentrations in EQAS region. First, comparison of **Fig. 8-1 a-c** and **d-f** indicates that the $PM_{2.5}$ distributions derived from GFAS and GFED4 are generally consistent. Both datasets capture similar spatial patterns and magnitudes of haze pollution, suggesting that their underlying emission estimates for the 2014-2016 period are broadly comparable.

Furthermore, during the 2014-2015 El Niño event, severe haze events are evident over large parts of Sumatra, Kalimantan, and the surrounding regions in Indonesia, with notable spillover effects across peninsular Malaysia and Singapore. Elevated $PM_{2.5}$ levels are also observed to a lesser extent over parts of southern Thailand and the southern Philippines, underscoring the extensive transboundary impact of these smouldering peat fires.

However, in contrast to the El Niño period, **Fig. 8-1 e** and **f** show considerably lower $PM_{2.5}$ concentrations in 2016 under La Niña conditions. The cooler and wetter climate, coupled with higher water tables, likely suppressed peat fire activity, resulting in fewer and less intense fires and consequently reduced $PM_{2.5}$ emissions across the region.

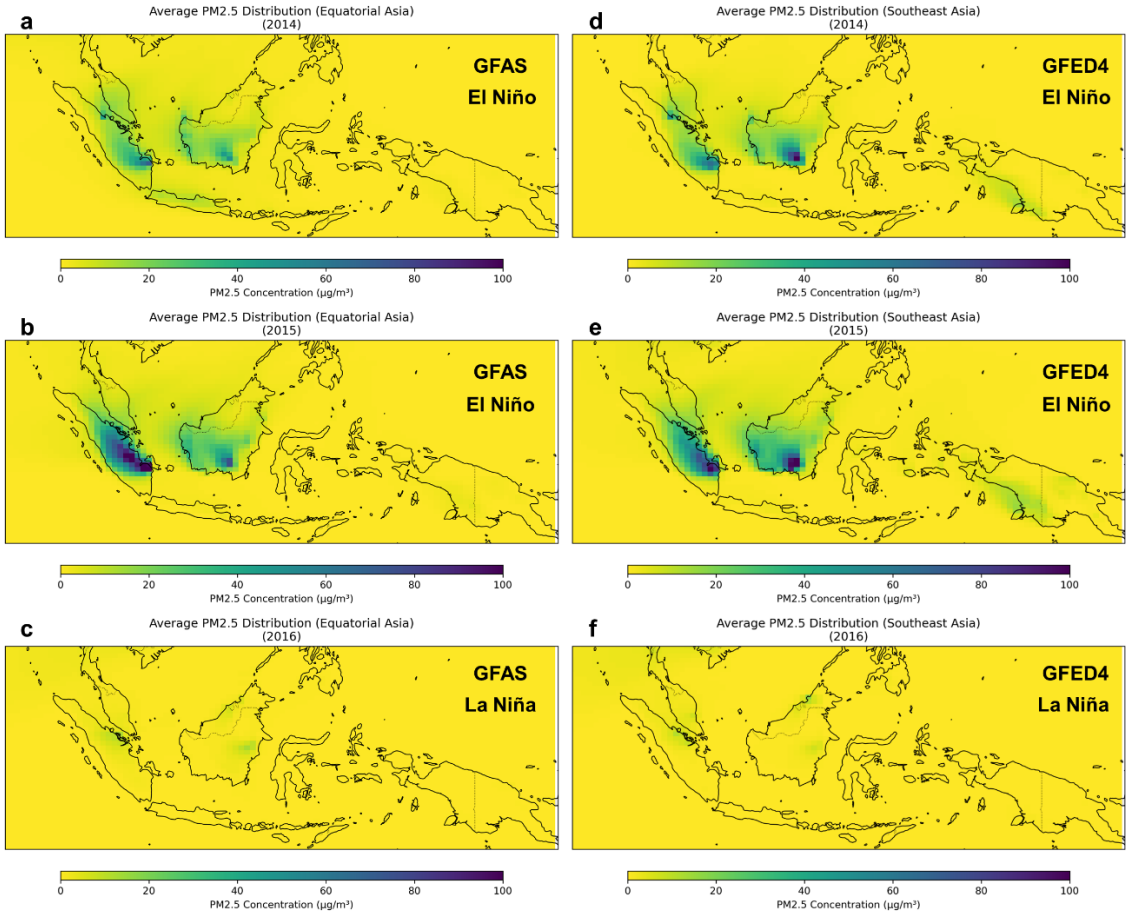

Fig. 8-1 Annual averaged fire sourced $PM_{2.5}$ concentrations in EQAS. The calculation is based on GFAS (**a-c**) and GFED4 (**d-f**) emission inventories and GEOS-Chem global chemical transport model.

Fig. 8-2 compares the annual averaged fire sourced $PM_{2.5}$ concentrations in major EQAS countries (i.e., Indonesia and Malaysia) with the total EQAS area. Overall, both datasets show a substantial increase in $PM_{2.5}$ during the 2014-2015 El Niño conditions compared to 2016, highlighting the strong influence of climate anomalies on fire activity. As shown in **Fig. 8-1**, the majority of peat fire emissions are concentrated in Indonesia's Sumatra Island, leading to relatively high local $PM_{2.5}$ levels in that region. However, when averaged over the entire country, Indonesia's overall $PM_{2.5}$ concentration appears lower because of its extensive land area, which includes regions with comparatively minimal fire activity. It should be noted that Malaysia exhibits the highest annual averages, with $PM_{2.5}$ concentrations exceeding 20 $\mu g/m^3$ in 2015 when using both datasets. This demonstrates the significant transboundary impact of Indonesian peat fires. By contrast, during the 2016 La Niña phase, all regions record considerably lower $PM_{2.5}$ levels (below 10 $\mu g/m^3$), reflecting the effect of climate on peat fire emissions. Despite some quantitative differences between GFAS and GFED4, both datasets display broadly similar trends, indicating a consistent representation of annual variability in peat associated haze.

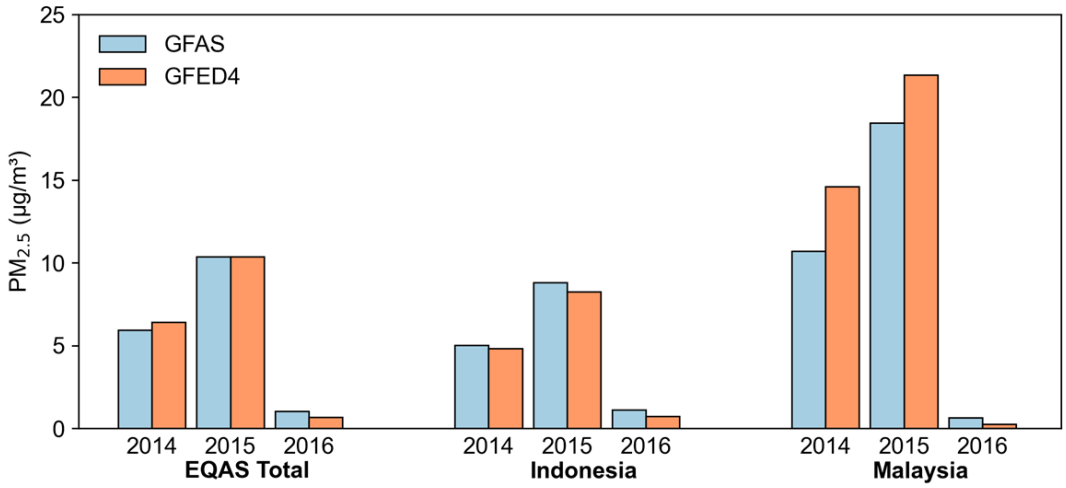

Fig. 8-2 Annual averaged fire sourced $PM_{2.5}$ concentrations in Indonesia, Malasia, and total EQAS area.

8.2.2 Fire-associated premature deaths

Fig. 8-3 compares the estimated premature deaths attributable to fire-sourced $PM_{2.5}$ exposure for the EQAS region (blue bars), Indonesia (green bars), and Malaysia (red bars) in 2014 and 2015, as calculated using GFAS (left column) and GFED4 (right column).

Overall, both datasets indicate a substantial increase in $PM_{2.5}$ -related mortality from 2014 to 2015. According to both datasets, the total deaths across the EQAS region reached 70,000-80,000 in 2014 and exceed 130,000 in 2015. Indonesia consistently accounts for the largest portion of these deaths, due to large population. In Malaysia, the corresponding estimates range from approximately 10,000-20,000 in 2014 and 20,000-30,000 in 2015.

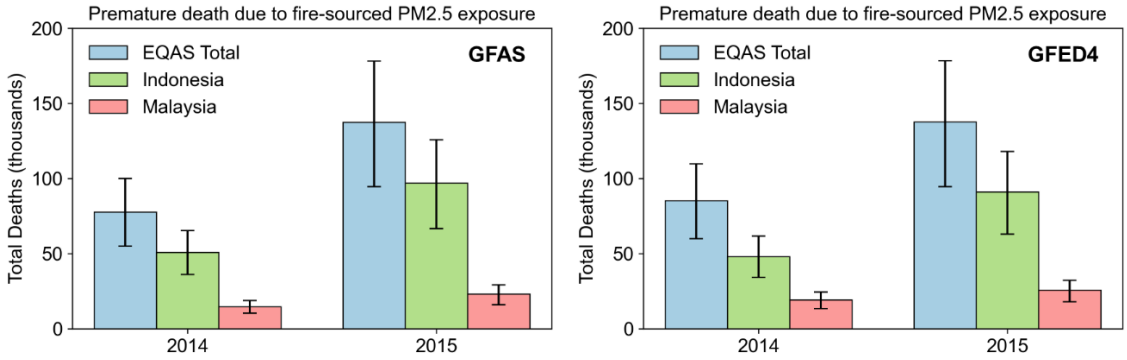

Fig. 8-3 Premature deaths due to fire-sourced $PM_{2.5}$ exposure based on GFAS and GFED4.

Fig. 8-4 shows annual premature deaths attributed to fire-sourced $PM_{2.5}$ for the EQAS region, Indonesia, and Malaysia in 2014 **(a-b)** and 2015 **(c-d)**, separated by five causes of death: Lower Respiratory Infections (LRI), Ischemic Heart Disease (IHD), Stroke, Chronic Obstructive Pulmonary Disease (COPD), and Lung Cancer. **Fig. 8-4 a** and **c** are based on GFAS data, while **Fig. 8-4 b** and **d** use GFED4. Although there are minor differences in magnitude between GFAS and GFED4, both exhibit similar distributions across the five CODs.

In general, IHD and Stroke contribute the largest share of estimated mortality, with LRI, COPD, and Lung Cancer accounting for lower but still significant portions. By 2015, all CODs show a marked increase in deaths, consistent with the intensified peat fire activity during El Niño. Indonesia suffers the highest premature death burden in both years, while Malaysia experiences a smaller yet notable rise in each COD from 2014 to 2015. Overall, the figures highlight how smouldering peat fire emissions can pose substantial health impacts across multiple diseases, particularly during severe fire seasons.

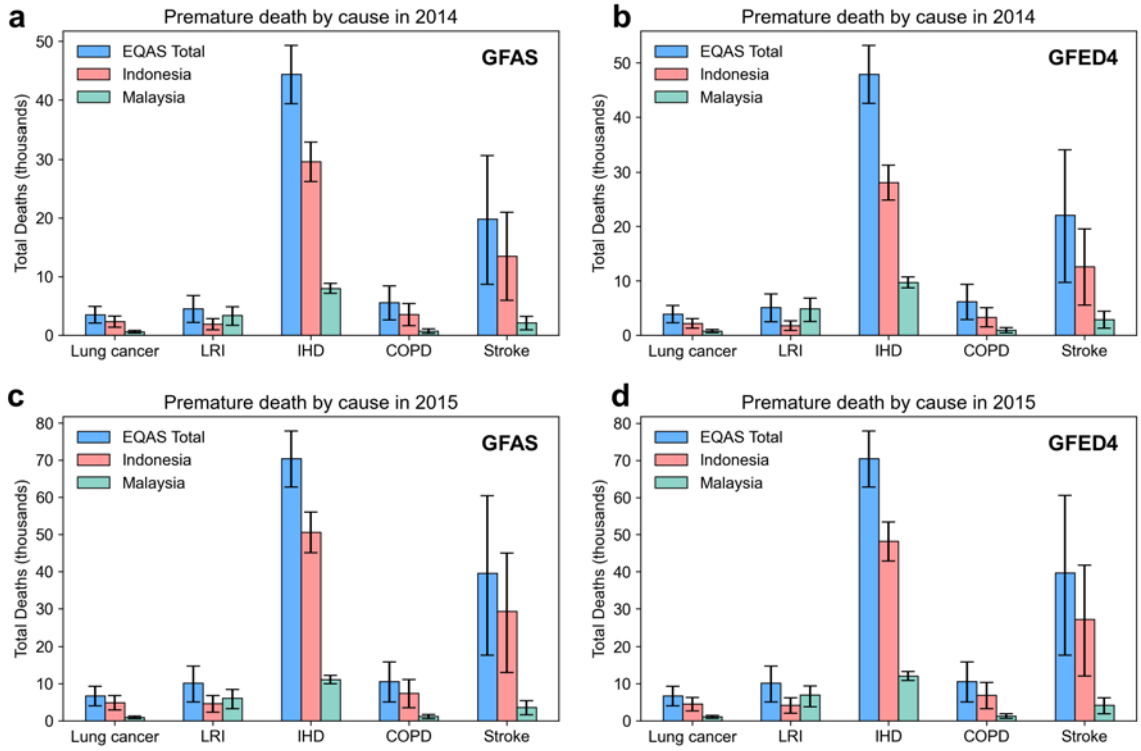

Fig. 8-4 Premature deaths caused by 5 Cause of Death (COD): including Ischaemic Heart Disease (IHD), Lung Cancer, Stroke, Chronic Obstructive Pulmonary Disease (COPD), and Lower Respiratory Infections (LRI).

8.2.3 Limitations and future work

First, this study only focuses on a relatively short time span (2014–2016) and uses South-east Asia as a case study, which may limit the generalizability of our findings. A more extensive analysis covering a temporal range and broader spatial regions would offer deeper insights into the global impacts of smouldering peat fires.

Second, the reliance on country-averaged $PM_{2.5}$ concentrations may underestimate exposure in large countries, e.g., Indonesia, where fire activity and population distributions can vary considerably. Future research should incorporate population-weighted models to improve the accuracy of health impact assessments.

Finally, although peat fires are the dominate form in the EQAS region, the current work employs GFED4 and GFAS, which do not explicitly distinguish peat fires from general wildfires. More precise estimates could be obtained by integrating specialized

peat fire datasets. In addition, future work will use our established ML models to improve the peat fire emission inventories.

8.3 Conclusions

This study demonstrates that smouldering peat fires in South-east Asia, particularly during the 2014–2015 El Niño event, substantially elevated regional $PM_{2.5}$ levels and associated health risks. Our analysis using GFAS and GFED4 fire emission inventories, coupled with GEOS-Chem simulations and GEMM epidemiological model, reveals that fire-sourced $PM_{2.5}$ concentrations were markedly higher during El Niño conditions compared to the subsequent La Niña period. Specifically, the total deaths across the EQAS region reached 70,000-80,000 in 2014, and exceed 130,000 in 2015. Indonesia consistently accounts for the largest portion of these deaths. Among the five causes of death considered, Ischaemic Heart Disease and Stroke are the primary contributors to fire-associated premature deaths.

However, our analysis is limited by its short temporal span and regional focus, and the use of country-averaged $PM_{2.5}$ may underestimate exposure in large, heterogeneous countries. Future work should extend the temporal and spatial scope, incorporate population-weighted exposure models, and utilize specialized peat fire datasets and our proposed EF prediction models by ML to improve emission estimates and health impact assessments.

CHAPTER 9 Conclusions and outlook

9.1 Conclusions

This thesis conducts a comprehensive study on smouldering wildfires, including the combustion thresholds, emissions predictions, and public health impacts. Guided by the objectives, this thesis 1) investigated the combustion dynamics of underground smouldering fires, 2) explored the oxygen thresholds for sustaining combustion using a novel forced internal oxygen supply reactor, 3) developed and validated a numerical model to capture the critical oxygen supply characteristics, 4) built an ML model to predict emission factors from various WUI fuels, 5) re-assessed the public health impacts of smouldering peat fires in South-east Asia during 2014-2015 by integrating fire BA data, fire radiative power data, chemical transport models, and epidemiological models. The key findings of each result chapter are summarized as follows:

Chapter 4 experimentally demonstrated that smouldering underground fires could sustain in deep soil layers for more than 10 days, regardless of the initial burning position. As the initial burning position becomes deeper, four smouldering burning modes can be observed: (I) downward propagation, (II) upward-and-downward propagation, (III) in-depth propagation, and (IV) no propagation (local burning). For the in-depth fire propagation and localised burning, no visual smoke, noticeable collapse, or regression was observed, indicating the difficulty of detecting deep peat fires. In addition, the CO concentration near the surface varies on the order of 10 to 10^2 ppm, which can be used to detect underground fires and monitor its intensity. High peat MC can slow down in-depth fire propagation and reduce the burning duration.

Considering persistent nature of smouldering peat fire under oxygen-limited conditions, ***Chapter 5*** designed a novel combustion reactor to experimentally quantify the limiting oxygen supply to sustain different smouldering propagation modes. Following ignition at the middle of the fuel bed, increasing the flow velocity causes the smouldering to transition from unidirectional (opposed) to bidirectional (opposed and forward) propagation. The minimum oxidizer flow velocities to sustain both modes of propagation decrease as the oxygen concentration increases. The minimum oxygen supply rate for stable smouldering propagation decreases with the oxygen concentration and approaches a critical value of 0.08 $g/m^2 \cdot s$ at ambient oxygen level. Moreover, smouldering is found to

survive at an extremely low oxygen concentration of 2%, so the value of minimum oxygen concentration (if exists) is even smaller.

Building on the findings of Chapter 5 and to extrapolate the experimental results, ***Chapter 6*** employed numerical simulations to investigate the oxygen supply thresholds or smothering limits of pine needle beds. The model integrating heat-and-mass transfer and 5-step heterogeneous chemistry was established using an open-source code Gpyro and was successfully validated through well-controlled experiments. Subsequently, the required oxidizer flow velocity or oxygen supply rate was predicted to increase as the oxygen concentration decreased. Notably, the predicted limiting oxygen concentration specially for smouldering combustion was about 3%, agreeing well with both the experimental observations and theoretical analysis.

To better evaluate the impact of smouldering fires, ***Chapter 7*** developed an ML-based approach to predict fire EFs in WUI fires, addressing a critical gap in emission estimation methods. A dataset of WUI fire EFs was compiled from the literature, incorporating key influencing factors such as fuel type, density, combustion mode, test scale, thermal conditions, and oxygen supply conditions. An ANN model was trained to establish correlations between these parameters and the EFs of CO_2, CO, and TPM. The results showed R^2 values of 0.56, 0.62, and 0.61 for CO, CO_2, and TPM, respectively, demonstrating a robust predictive performance. However, the model can be further improved by increasing the dataset size, enhancing data quality, and exploring additional ML algorithms, among other approaches.

Integrating fire emission inventories, GEOS-Chem simulations and GEMM epidemiological model, ***Chapter 8*** demonstrates that smouldering peat fires in South-east Asia substantially elevated regional $PM_{2.5}$ levels and associated health risks, particularly during the 2014-2015 El Niño event. Specifically, the total deaths across the EQAS region reached 70,000-80,000 in 2014 and exceed 130,000 in 2015. Indonesia accounts for more than half of these deaths. Among the five causes of death considered, Ischaemic Heart Disease and Stroke are the primary contributors to fire-associated premature mortality.

9.2 Outlook

The findings of this thesis provide valuable insights into the fundamental dynamics and impacts of smouldering fires, while also highlighting several areas that require further exploration and improvement in the following aspects:

- Current experiments and numerical model on smouldering oxygen thresholds are simplified into one-dimension. Future work should extend beyond the current one-dimensional framework to investigate the influence of boundary heat loss on smouldering combustion dynamics, which remains a critical yet underexplored factor in realistic fire scenarios.

- The largest-scale experiments conducted in this study were limited to a 1-meter-deep fuel bed. Therefore, laboratory and field experiments in larger scales are necessary to validate the persistence and propagation characteristics of deep peat fires under natural conditions.

- The emission factor prediction model, currently achieving an R^2 value of only 0.5-0.6 due to limitations in dataset size and quality, would benefit from an expanded and improved database, as well as the exploration of alternative algorithms to enhance prediction accuracy.

- Current public health impact analysis focused on the 2014-2016 period in South-east Asia. Future studies should adopt broader temporal and spatial scales to systematically assess the global premature mortality and broader public health implications associated with smouldering fires. Meanwhile, the newly established ML model will help characterize EFs, enabling more precise predictions of public health impacts.

References

Aguilera R, Corringham T, Gershunov A, Benmarhnia T (2021) Wildfire smoke impacts respiratory health more than fine particles from other sources: observational evidence from Southern California. *Nature Communications* **12**,.

Akagi SK, Yokelson RJ, Wiedinmyer C, Alvarado MJ, Reid JS, Karl T, Crounse JD, Wennberg PO (2011) Emission factors for open and domestic biomass burning for use in atmospheric models. *Atmospheric Chemistry and Physics* **11**, 4039–4072.

Alves CA, Gonçalves C, Pio CA, Mirante F, Caseiro A, Tarelho L, Freitas MC, Viegas DX (2010) Smoke emissions from biomass burning in a Mediterranean shrubland. *Atmospheric Environment* **44**, 3024–3033.

Anca-Couce A, Zobel N, Berger A, Behrendt F (2012) Smouldering of pine wood: Kinetics and reaction heats. *Combustion and Flame* **159**, 1708–1719.

Anderson K (2002) A model to predict lightning-caused fire occurrences. *International Journal of Wildland Fire* **11**, 163–172.

Anderson K, Chen J, Englefield P, Griffin D, Makar PA, Thompson D (2024) The Global Forest Fire Emissions Prediction System version 1.0. *Geoscientific Model Development* **1**,.

Andreae MO (2001) Emission of trace gases and aerosols from biomass burning. *Global Biogeochemical Cycles* **15**, 955–966.

Aouizerats B, Van Der Werf GR, Balasubramanian R, Betha R (2015) Importance of transboundary transport of biomass burning emissions to regional air quality in Southeast Asia during a high fire event. *Atmospheric Chemistry and Physics* **15**, 363–373.

Arden Pope C, Burnett RT, Turner MC, Cohen A, Krewski D, Jerrett M, Gapstur SM, Thun MJ (2011) Lung cancer and cardiovascular disease mortality associated with ambient air pollution and cigarette smoke: Shape of the exposure-response relationships. *Environmental Health Perspectives* **119**, 1616–1621.

Aurell J, Gullett B, Holder A, Kiros F, Mitchell W, Watts A, Ottmar R (2021) Wildland fire emission sampling at Fishlake National Forest, Utah using an unmanned aircraft system. *Atmospheric Environment* **247**, 5259–5273.

Ballhorn U, Siegert F, Mason M, Limin S (2009) Derivation of burn scar depths and estimation of carbon emissions with LIDAR in Indonesian peatlands. *Proceedings of the National Academy of Sciences of the United States of America* **106**, 21213–21218.

Bar-Ilan A, Rein G, C.walther D, Fernandez-Pello AC, Torero JL, Urban DL (2004) The effect of buoyancy on opposed smoldering. *Combustion Science and Technology* **176**, 2027–2055.

Belcher CM, Yearsley JM, Hadden RM, McElwain JC, Rein G (2010) Baseline intrinsic flammability of Earth's ecosystems estimated from paleoatmospheric oxygen over the past 350 million years. *Proceedings of the National Academy of Sciences of the United States of America* **107**, 22448–22453.

Benkorichi S, Fateh T, Richard F, Consalvi JL, Nadjai A (2017) Investigation of thermal degradation of pine needles using multi-step reaction mechanisms. *Fire Safety Journal* **91**, 811–819.

Benscoter BW, Thompson DK, Waddington JM, Flannigan MD, Wotton BM, De Groot WJ, Turetsky MR (2011) Interactive effects of vegetation, soil moisture and bulk density on depth of burning of thick organic soils. *International Journal of Wildland Fire* **20**, 418–429.

Black RR, Aurell J, Holder A, George IJ, Gullett BK, Hays MD, Geron CD, Tabor D (2016) Characterization of gas and particle emissions from laboratory burns of peat. *Atmospheric Environment* **132**, 49–57.

Brauer M, Roth GA, Aravkin AY, Zheng P, Abate KH, Abate YH, Abbafati C, Abbasgholizadeh R, Abbasi MA, Abbasian M, et al. (2024) Global burden and strength of evidence for 88 risk factors in 204 countries and 811 subnational locations, 1990–2021: a systematic analysis for the Global Burden of Disease Study 2021. *The Lancet* **403**, 2162–2203.

Burling IR, Yokelson RJ, Griffith DWT, Johnson TJ, Veres P, Roberts JM, Warneke C, Urbanski SP, Reardon J, Weise DR, et al. (2010) Laboratory measurements of trace gas emissions from biomass burning of fuel types from the southeastern and southwestern United States. *Atmospheric Chemistry and Physics* **10**, 11115–11130.

Burling IR, Yokelson RJ, Akagi SK, Urbanski SP, Wold CE, Griffith DWT, Johnson TJ, Reardon J, Weise DR (2011) Airborne and ground-based measurements of the trace gases and particles emitted by prescribed fires in the United States. *Atmospheric Chemistry and Physics* **11**, 12197–12216.

Burnett RT, Arden Pope C, Ezzati M, Olives C, Lim SS, Mehta S, Shin HH, Singh G, Hubbell B, Brauer M, et al. (2014) An integrated risk function for estimating the global burden of disease attributable to ambient fine particulate matter exposure. *Environmental Health Perspectives* **122**, 397–403.

Burnett R, Chen H, Szyszkowicz M, Fann N, Hubbell B, Pope CA, Apte JS, Brauer M, Cohen A, Weichenthal S, et al. (2018) Global estimates of mortality associated with longterm exposure to outdoor fine particulate matter. *Proceedings of the National Academy of Sciences of the United States of America* **115**, 9592–9597.

Cairncross EK, John J, Zunckel M (2007) A novel air pollution index based on the relative risk of daily mortality associated with short-term exposure to common air pollutants. *Atmospheric Environment* **41**, 8442–8454.

Cancellieri D, Leroy-Cancellieri V, Leoni E, Simeoni A, Kuzin AY, Filkov AI, Rein G (2012) Kinetic investigation on the smouldering combustion of boreal peat. *Fuel* **93**, 479–485.

Carreras-Sospedra M, Zhu S, MacKinnon M, Lassman W, Mirocha JD, Barbato M, Dabdub D (2024) Air quality and health impacts of the 2020 wildfires in California. *Fire Ecology* **20**,.

Carvalho ER, Gurgel Veras CA, Carvalho JA (2002) Experimental investigation of smouldering in biomass. *Biomass and Bioenergy* **22**, 283–294.

Chakrabarty RK, Gyawali M, Yatavelli RLN, Pandey A, Watts AC, Knue J, Chen LWA, Pattison RR, Tsibart A, Samburova V, et al. (2016) Brown carbon aerosols from burning of boreal peatlands: Microphysical properties, emission factors, and implications for direct radiative forcing. *Atmospheric Chemistry and Physics* **16**, 3033–3040.

Chen LWA, Moosmüller H, Arnott WP, Chow JC, Watson JG, Susott RA, Babbitt RE, Wold CE, Lincoln EN, Wei MH (2007) Emissions from laboratory combustion of

wildland fuels: Emission factors and source profiles. *Environmental Science and Technology* **41**, 4317–4325.

Chen Y, Liang Z, Lin S, Huang X (2022) Limits of sustaining a flame above smoldering woody biomass. *Combustion Science and Technology* **195**, 2801–2819.

Chen Y, Lin S, Qin Y, Surawski NC, Huang X (2023a) Carbon distribution and multi-criteria decision analysis of flexible waste biomass smouldering processing technologies. *Waste Management* **167**, 183–193.

Chen Y, Hall J, van Wees D, Andela N, Hantson S, Giglio L, Van der Werf GR, Morton DC, Randerson JT (2023b) Multi-decadal trends and variability in burned area from the 5th version of the Global Fire Emissions Database (GFED5). *Earth System Science Data* **2023**, 1–52. https://essd.copernicus.org/preprints/essd-2023-182/.

Chen Y, Wang Z, Lin S, Qin Y, Huang X (2023c) A review on biomass thermal-oxidative decomposition data and machine learning prediction of thermal analysis. *Cleaner Materials* **9**, 100206.

Chen G, Guo Y, Yue X, Xu R, Yu W, Ye T, Tong S, Gasparrini A, Bell ML, Armstrong B, et al. (2024) All-cause, cardiovascular, and respiratory mortality and wildfire-related ozone: a multicountry two-stage time series analysis. *The Lancet Planetary Health* **8**, e452–e462.

Christensen E, Y. H, Restuccia F, Santoso MAMA, Huang X, Rein G, Hu Y, Restuccia F, Santoso MAMA, Huang X, et al. (2019) Experimental methods and scales in smouldering wildfires. 'Fire Eff. Soil Prop.' (Ed P Pereira) pp. 267–280. (CSIRO)

Christian TJ, Kleiss B, Yokelson RJ, Holzinger R, Crutzen PJ, Hao WM, Saharjo BH, Ward DE (2003) Comprehensive laboratory measurements of biomass-burning emissions: 1. Emissions from Indonesian, African, and other fuels. *Journal of Geophysical Research: Atmospheres* **108**,.

Christian TJ, Yokelson RJ, Carvalho JA, Griffith DWT, Alvarado EC, Santos JC, Neto TGS, Veras CAG, Hao WM (2007) The tropical forest and fire emissions experiment: Trace gases emitted by smoldering logs and dung from deforestation and pasture fires in Brazil. *Journal of Geophysical Research Atmospheres* **112**, 1–14.

Cohen AJ, Ross Anderson H, Ostro B, Pandey KD, Krzyzanowski M, Künzli N,

Gutschmidt K, Pope A, Romieu I, Samet JM (2005) The global burden of disease due to outdoor air pollution. *Journal of Toxicology and Environmental Health, Part A* **68**, 1301–1307.

Cohen AJ, Brauer M, Burnett R, Anderson HR, Frostad J, Estep K, Balakrishnan K, Brunekreef B, Dandona L, Dandona R, et al. (2017) Estimates and 25-year trends of the global burden of disease attributable to ambient air pollution: an analysis of data from the Global Burden of Diseases Study 2015. *The Lancet* **389**, 1907–1918.

Cui W, Dossi S, Rein G (2023) Laboratory benchmark of low-cost portable gas and particle analysers at the source of smouldering wildfires. *International Journal of Wildland Fire* **32**, 1542–1557.

Dadap NC, Cobb AR, Hoyt AM, Harvey CF, Konings AG (2019) Satellite soil moisture observations predict burned area in Southeast Asian peatlands. *Environmental Research Letters* **14**,.

Darmenov AS, Silva A (2015) The Quick Fire Emissions Dataset (QFED): Documentation of versions 2.1, 2.2 and 2.4. *Technical Report Series on Global Modeling and Data Assimilation* **38**,.

Decker MA, Schult DA (2004) Dynamics of smoulder waves near extinction. *Combustion Theory and Modelling* **8**, 491–512.

Depci T, Karta M (2018) Peat and lignite leaching process with tetralin in autoclave to produce oil. *Physicochemical Problems of Mineral Processing* **54**, 334–342.

Desservettaz M, Paton-Walsh C, Griffith DWT, Kettlewell G, Keywood MD, Vanderschoot M V., Ward J, Mallet MD, Milic A, Miljevic B, et al. (2017) Emission factors of trace gases and particles from tropical savanna fires in Australia. *Journal of Geophysical Research* **122**, 6059–6074.

Dhammapala R, Claiborn C, Simpson C, Jimenez J (2007) Emission factors from wheat and Kentucky bluegrass stubble burning: Comparison of field and simulated burn experiments. *Atmospheric Environment* **41**, 1512–1520.

Dickinson MB, Ryan KC (2010) Introduction: Strengthening the foundation of wildland fire effects prediction for research and management. *Fire Ecology* **6**, 1–12.

Du R, Mino A, Wang J, Zheng S (2024) Transboundary vegetation fire smoke and expressed sentiment: Evidence from Twitter. *Journal of Environmental Economics and Management* **124**, 102928.

Dupuy JL (1995) Slope and fuel load effects on fire behaviour :Laboratory experiments in pine needles fuel beds. *International Journal of Wildland Fire* **5**, 153–164.

Emmanuel SC (2000) Impact to lung health of haze from forest fires: The Singapore experience. *Respirology* **5**, 175–182.

Ernst A, Zibrak JD (1998) Carbon monoxide poisoning. *New England journal of medicine* **339**, 1603–1608.

Ezzati M, Lopez A, Rodgers A, Hoorn S, Murray C (2002) Comparative Risk Assessment Collaborating Group. Selected major risk factors and global and regional burden of disease. *Lancet (London, England)* **360**, 1347–1360.

Feng X, Lin H, Fu TM, Sulprizio MP, Zhuang J, Jacob DJ, Tian H, Ma Y, Zhang L, Wang X, et al. (2021) WRF-GC (v2.0): Online two-way coupling of WRF (v3.9.1.1) and GEOS-Chem (v12.7.2) for modeling regional atmospheric chemistry-meteorology interactions. *Geoscientific Model Development* **14**, 3741–3768.

Ferek RJ, Reid JS, Hobbs P V., Blake DR, Liousse C (1998) Emission factors of hydrocarbons, halocarbons, trace gases and particles from biomass burning in Brazil. *Journal of Geophysical Research: Atmospheres* **103**, 32107–32118.

Fernandez-Anez N, Christensen K, Frette V, Rein G (2019) Simulation of fingering behavior in smoldering combustion using a cellular automaton. *Physical Review E* **99**, 1–13.

Frandsen WH (1987) The influence of moisture and mineral soil on the combustion limits of smouldering forest duff. *Canadian Journal of Forest Research* **16**, 1540–1544.

Frandsen WH (1997) Ignition probability of organic soils. *Canadian Journal of Forest Research* **27**, 1471–1477.

Fujita O (2015) Solid combustion research in microgravity as a basis of fire safety in space. *Proceedings of the Combustion Institute* **35**, 2487–2502.

Garg P, Wang S, Oakes JM, Bellini C, Gollner MJ (2024) Variations in gaseous and

particulate emissions from flaming and smoldering combustion of Douglas fir and lodgepole pine under different fuel moisture conditions. *Combustion and Flame* **263**, 113386.

Geron C, Hays M (2013) Air emissions from organic soil burning on the coastal plain of North Carolina. *Atmospheric Environment* **64**, 192–199.

Giglio L, Randerson JT, Van Der Werf GR (2013) Analysis of daily, monthly, and annual burned area using the fourth-generation global fire emissions database (GFED4). *Journal of Geophysical Research: Biogeosciences* **118**, 317–328.

Goldstein JE, Graham L, Ansori S, Vetrita Y, Thomas A, Applegate G, Vayda AP, Saharjo BH, Cochrane MA (2020) Beyond slash-and-burn: The roles of human activities, altered hydrology and fuels in peat fires in Central Kalimantan, Indonesia. *Singapore Journal of Tropical Geography* 1–19.

Gong W, Cuevas J, Reszka P, Simeoni A (2024) The role of smoldering in the ignition of Pinus palustris needles. *Fire Safety Journal* **143**, 104053.

Goode JG, Yokelson RJ, Ward DE, Susott RA, Babbitt RE, Davies MA (2000) Measurements of excess 03, CO2, CO, CH4, C2H4, C2H2, HCN, NO, NH3, HCOOH, CH3COOH, HCHO, and CH3OH in 1997 Alaskan biomass burning plumes by airborne Fourier transform infrared spectroscopy (AFTIR). *Journal of Geophysical Research* **105**,.

Guérette EA, Paton-Walsh C, Desservettaz M, Smith TEL, Volkova L, Weston CJ, Meyer CP (2018) Emissions of trace gases from Australian temperate forest fires: Emission factors and dependence on modified combustion efficiency. *Atmospheric Chemistry and Physics* **18**, 3717–3735.

Gumbricht T, Mccarthy T, McCarth J, Roy D, Frost PE, Wessels K (2002) Remote sensing to detect sub-surface peat fires and peat fire scars in the Okavango Delta, Botswana. *South African Journal of Science* **98**, 851–858.

Hadden RM, Rein G, Belcher CM (2013) Study of the competing chemical reactions in the initiation and spread of smouldering combustion in peat. *Proceedings of the Combustion Institute* **34**, 2547–2553.

Hadden R, Rein G (2011) Chapter 18 - Burning and Water Suppression of Smoldering

Coal Fires in Small-Scale Laboratory Experiments. (Eds GB Stracher, A Prakash, EVBT-C and PFAGP Sokol) pp. 317–326. (Elsevier: Amsterdam)

Heil A, Goldammer JG (2001) Smoke-haze pollution: a review of the 1997 episode in Southeast Asia. *Regional Environmental Change* **2**, 24–37.

Henderson SB, Brauer M, MacNab YC, Kennedy SM (2011) Three measures of forest fire smoke exposure and their associations with respiratory and cardiovascular health outcomes in a population-based cohort. *Environmental Health Perspectives* **119**, 1266–1271.

Hermesdorf L, Elberling B, D'Imperio L, Xu W, Lambæk A, Ambus PL (2022) Effects of fire on CO2, CH4, and N2O exchange in a well-drained Arctic heath ecosystem. *Global Change Biology* **28**, 4882–4899.

Hinds WC, Zhu Y (2022) 'Aerosol technology: properties, behavior, and measurement of airborne particles.' (John Wiley & Sons)

Hinwood AL, Rodriguez CM (2005) Potential health impacts associated with peat smoke: A review. *Journal of the Royal Society of Western Australia* **88**, 133–138.

Hu J, Ying Q, Wang Y, Zhang H (2015) Characterizing multi-pollutant air pollution in China: Comparison of three air quality indices. *Environment International* **84**, 17–25.

Hu Y, Fernandez-Anez N, Smith TELL, Rein G (2018) Review of emissions from smouldering peat fires and their contribution to regional haze episodes. *International Journal of Wildland Fire* **27**, 293–312.

Hu Y, Christensen EG, Amin HMF, Smith TEL, Rein G (2019a) Experimental study of moisture content effects on the transient gas and particle emissions from peat fire. *Combustion and Flame* **209**, 408–417.

Hu Y, Christensen E, Restuccia F, Rein G (2019b) Transient gas and particle emissions from smouldering combustion of peat. *Proceedings of the Combustion Institute* **37**, 4035–4042.

Huang X, Rein G, Chen H (2015) Computational smoldering combustion: Predicting the roles of moisture and inert contents in peat wildfires. *Proceedings of the Combustion*

Institute **35**, 2673–2681.

Huang X, Restuccia F, Gramola M, Rein G (2016) Experimental study of the formation and collapse of an overhang in the lateral spread of smouldering peat fires. *Combustion and Flame* **168**, 393–402.

Huang X, Rein G (2014) Smouldering combustion of peat in wildfires: Inverse modelling of the drying and the thermal and oxidative decomposition kinetics. *Combustion and Flame* **161**, 1633–1644.

Huang X, Rein G (2015) Computational study of critical moisture and depth of burn in peat fires. *International Journal of Wildland Fire* **24**, 798–808.

Huang X, Rein G (2016a) Interactions of Earth's atmospheric oxygen and fuel moisture in smouldering wildfires. *Science of the Total Environment* **572**, 1440–1446.

Huang X, Rein G (2016b) Thermochemical conversion of biomass in smouldering combustion across scales: The roles of heterogeneous kinetics, oxygen and transport phenomena. *Bioresource Technology* **207**, 409–421.

Huang X, Rein G (2017) Downward spread of smouldering peat fire: The role of moisture, density and oxygen supply. *International Journal of Wildland Fire* **26**, 907–918.

Huang X, Rein G (2019) Upward-and-downward spread of smoldering peat fire. *Proceedings of the Combustion Institute* **37**, 4025–4033.

Hugron S, Bussières J, Rochefort L (2013) 'Tree plantations within the context of ecological restoration of peatlands: practical guide.' (Peatland Ecology Research Group, Université Laval, Québec) http://www.gret-perg.ulaval.ca/uploads/tx_centrerecherche/Tree_Plantation_guide.pdf.

Ichoku C, Ellison L (2014) Global top-down smoke-aerosol emissions estimation using satellite fire radiative power measurements. *Atmospheric Chemistry and Physics* **14**, 6643–6667.

Iinuma Y, Brüggemann E, Gnauk T, Müller K, Andreae MO, Helas G, Parmar R, Herrmann H (2007) Source characterization of biomass burning particles: The combustion of selected European conifers, African hardwood, savanna grass, and German and Indonesian peat. *Journal of Geophysical Research Atmospheres* **112**,.

Incropera FP (2007) ‘Principles of heat and mass transfer.’ (Hoboken, NJ : Wiley. U.S.)

Janẖall S, Andreae MO, Pöschl U (2010) Biomass burning aerosol emissions from vegetation fires: Particle number and mass emission factors and size distributions. *Atmospheric Chemistry and Physics* **10**, 1427–1439.

Jayachandran S (2009) Air quality and early-life mortality evidence from Indonesia’s wildfires. *Journal of Human resources* **44**, 916–954.

Jayarathne T, Stockwell CE, Gilbert AA, Daugherty K, Cochrane MA, Ryan KC, Putra EI, Saharjo BH, Nurhayati AD, Albar I, et al. (2018) Chemical characterization of fine particulate matter emitted by peat fires in Central Kalimantan, Indonesia, during the 2015 El Niño. *Atmospheric Chemistry and Physics* **18**, 2585–2600.

Johnston FH, Henderson SB, Chen Y, Randerson JT, Marlier M, DeFries RS, Kinney P, Bowman DMJS, Brauer M (2012) Estimated global mortality attributable to smoke from landscape fires. *Environmental Health Perspectives* **120**, 695–701.

Johnston MC, T’ien JS (2017) Gravimetric measurement of solid and liquid fuel burning rate near and at the low oxygen extinction limit. *Fire Safety Journal* **91**, 140–146.

Jolly WM, Cochrane MA, Freeborn PH, Holden ZA, Brown TJ, Williamson GJ, Bowman DMJS (2015) Climate-induced variations in global wildfire danger from 1979 to 2013. *Nature Communications* **6**, 1–11.

Kadowaki O, Suzuki M, Kuwana K, Nakamura Y, Kushida G (2021) Limit conditions of smoldering spread in counterflow configuration: Extinction and smoldering-to-flaming transition. *Proceedings of the Combustion Institute* **38**, 5005–5013.

Kaiser JW, Heil A, Andreae MO, Benedetti A, Chubarova N, Jones L, Morcrette JJ, Razinger M, Schultz MG, Suttie M, et al. (2012) Biomass burning emissions estimated with a global fire assimilation system based on observed fire radiative power. *Biogeosciences* **9**, 527–554.

Karl TG, Christian TJ, Yokelson RJ, Artaxo P, Hao WM, Guenther A (2007) The tropical forest and fire emissions experiment: Method evaluation of volatile organic compound emissions measured by PTR-MS, FTIR, and GC from tropical biomass burning. *Atmospheric Chemistry and Physics* **7**, 5883–5897.

Kiely L, Spracklen D V., Wiedinmyer C, Conibear L, Reddington CL, Arnold SR, Knote C, Khan MF, Latif MT, Syaufina L, et al. (2020) Air quality and health impacts of vegetation and peat fires in Equatorial Asia during 2004-2015. *Environmental Research Letters* **15**,.

Koplitz SN, Mickley LJ, Marlier ME, Buonocore JJ, Kim PS, Liu T, Sulprizio MP, DeFries RS, Jacob DJ, Schwartz J, et al. (2016) Public health impacts of the severe haze in Equatorial Asia in September-October 2015: Demonstration of a new framework for informing fire management strategies to reduce downwind smoke exposure. *Environmental Research Letters* **11**,.

Kumar A, T'Ien J (2012) Numerical modeling of limiting oxygen index apparatus for film type fuels. *International Journal of Spray and Combustion Dynamics* **4**, 299–322.

Lautenberger C (2014) Gpyro-A Generalized Pyrolysis Model for Combustible Solids:Technical Reference. (Berkeley)

Lautenberger C, Fernandez-Pello C (2009) Generalized pyrolysis model for combustible solids. *Fire Safety Journal* **44**, 819–839.

Lestari P, Muthmainnah F, Permadi DA (2020) Characterization of carbonaceous compounds emitted from Indonesian surface and sub surface peat burning. *Atmospheric Pollution Research* **11**, 1465–1472.

Lestari P, Tasrifani AR, Suri WI, Wooster MJ, Grosvenor MJ, Fujii Y, Ardiyani V, Carboni E, Thomas G (2024) Gaseous, particulate matter, carbonaceous compound, water-soluble ion, and trace metal emissions measured from 2019 peatland fires in Palangka Raya, Central Kalimantan. *Atmospheric Environment* **316**, 120171.

Li F, Val Martin M, Andreae MO, Arneth A, Hantson S, Kaiser JW, Lasslop G, Yue C, Bachelet D, Forrest M, et al. (2019) Historical (1700-2012) global multi-model estimates of the fire emissions from the Fire Modeling Intercomparison Project (FireMIP). *Atmospheric Chemistry and Physics* **19**, 12545–12567.

Li R, Chen W, Zhao H, Wu X, Zhang M, Tong DQ, Xiu A (2020) Inventory of Atmospheric Pollutant Emissions from Burning of Crop Residues in China Based on Satellite-retrieved Farmland Data. *Chinese Geographical Science* **30**, 266–278.

Li J, Zhao Q, Si M, Dong Z, Huang J, Li Y, Hu X, Tian S (2023) Removal of cadmium in contaminated soils by self-sustaining smoldering. *Journal of Environmental Chemical Engineering* **11**, 109869.

Lin S, Sun P, Huang X (2019) Can peat soil support a flaming wildfire? *International Journal of Wildland Fire* **28**, 601–613.

Lin H, Feng X, Fu T, Tian H, Ma Y, Zhang L, Jacob DJ, Yantosca RM, Sulprizio MP, Lundgren EW, et al. (2020a) WRF-GC (v1.0): online coupling of WRF (v3.9.1.1) and GEOS-Chem (v12.2.1) for regional atmospheric chemistry modeling – Part 1: Description of the one-way model. *Geoscientific Model Development* **13**, 3241–3265.

Lin S, Cheung YK, Xiao Y, Huang X (2020b) Can rain suppress smoldering peat fire? *Science of the Total Environment* **727**, 138468.

Lin S, Liu Y, Huang X (2021a) Climate-induced Arctic-boreal peatland fire and carbon loss in the 21st century. *Science of the Total Environment* **796**, 148924.

Lin S, Liu Y, Huang X (2021b) How to build a firebreak to stop smouldering peat fire: Insights from a laboratory-scale study. *International Journal of Wildland Fire* **30**, 454–461.

Lin S, Chow TH, Huang X (2021c) Smoldering propagation and blow-off on consolidated fuel under external airflow. *Combustion and Flame* **234**, 111685.

Lin S, Yuan H, Huang X (2022a) A computational study on the quenching and near-limit propagation of smoldering combustion. *Combustion and Flame* **238**, 111937.

Lin S, Wang S, Huang X (2022b) Modeling smoldering ignition by an irradiation spot. *Fire Safety Journal* **134**, 103708.

Lin S, Huang X (2020) An experimental method to investigate the water-based suppression of smoldering peat fire. *MethodsX* **7**,.

Lin S, Huang X (2021) Quenching of smoldering: Effect of wall cooling on extinction. *Proceedings of the Combustion Institute* **38**, 5015–5022.

Liu M, Popescu S (2022) Estimation of biomass burning emissions by integrating ICESat-2, Landsat 8, and Sentinel-1 data. *Remote Sensing of Environment* **280**, 113172.

Liu M, Yang L (2023) A global fire emission dataset using the three-corner hat method (FiTCH). *Earth System Science Data Discussions* **2023**, 1–20.

Lopez AD (2006) 'Global burden of disease and risk factors.' (World Bank Publications)

Lou S, Liu Y, Bai Y, Li F, Lin G, Xu L, Liu Z, Chen Y, Dong X, Zhao M, et al. (2023) Projections of mortality risk attributable to short-term exposure to landscape fire smoke in China, 2021–2100: a health impact assessment study. *The Lancet Planetary Health* **7**, e841–e849.

Mack MC, Bret-Harte MS, Hollingsworth TN, Jandt RR, Schuur EAG, Shaver GR, Verbyla DL (2011) Carbon loss from an unprecedented Arctic tundra wildfire. *Nature* **475**, 489–492.

Malow M, Krause U (2008) Smouldering combustion of solid bulk materials at different volume fractions of oxygen in the surrounding gas. *Fire Safety Science* 303–314.

Marlier ME, Defries RS, Voulgarakis A, Kinney PL, Randerson JT, Shindell DT, Chen Y, Faluvegi G, Miriam E. Marlier, Ruth S. DeFries, et al. (2013) El Niño and health risks from landscape fire emissions in southeast Asia. *Nature Climate Change* **3**, 131–136.

Martin R V., Eastham SD, Bindle L, Lundgren EW, Clune TL, Keller CA, Downs W, Zhang D, Lucchesi RA, Sulprizio MP, et al. (2022) Improved advection, resolution, performance, and community access in the new generation (version 13) of the high-performance GEOS-Chem global atmospheric chemistry model (GCHP). *Geoscientific Model Development* **15**, 8731–8748.

May AA, McMeeking GR, Lee T, Taylor JW, Craven JS, Burling I, Sullivan AP, Akagi S, Collett Jr JL, Flynn M (2014) Aerosol emissions from prescribed fires in the United States: A synthesis of laboratory and aircraft measurements. *Journal of Geophysical Research: Atmospheres* **119**, 11–826.

McAllister S, Grenfell I, Hadlow a., Jolly WM, Finney M, Cohen J (2012) Piloted ignition of live forest fuels. *Fire Safety Journal* **51**, 133–142.

McCarty JL, Smith TEL, Turetsky MR (2020) Arctic fires re-emerging. *Nature Geoscience* **13**, 658–660.

McClure CD, Jaffe DA (2018) US particulate matter air quality improves except in wildfire-prone areas. *Proceedings of the National Academy of Sciences of the United States of America* **115**, 7901–7906.

McMeeking GR, Kreidenweis SM, Baker S, Carrico CM, Chow JC, Collett JL, Hao WM, Holden AS, Kirchstetter TW, Malm WC, et al. (2009) Emissions of trace gases and aerosols during the open combustion of biomass in the laboratory. *Journal of Geophysical Research: Atmospheres* **114**, 1–20.

Mitchell H, Amin R, Heidari M, Kotsovinos P, Rein G (2023) Structural hazards of smouldering fires in timber buildings. *Fire Safety Journal* **140**, 103861.

Morvan D, Larini M (2001) Modeling of one dimensional fire spread in pine needles with opposing air flow. *Combustion Science and Technology* **164**, 37–64.

Moussa N a., Toong TY, Garris C a. (1977) Mechanism of smoldering of cellulosic materials. *Symposium (International) on Combustion* **16**, 1447–1457.

Mulyasih H, Akbar LA, Ramadhan ML, Cesnanda AF, Putra RA, Irwansyah R, Nugroho YS (2022) Experimental study on peat fire suppression through water injection in laboratory scale. *Alexandria Engineering Journal* **61**, 12525–12537.

Nara H, Tanimoto H, Tohjima Y, Mukai H, Nojiri Y, Machida T (2017) Emission factors of CO2, CO and CH4 from Sumatran peatland fires in 2013 based on shipboard measurements. *Tellus, Series B: Chemical and Physical Meteorology* **69**, 1–14.

Nawaz MO, Henze DK (2020) Premature Deaths in Brazil Associated With Long-Term Exposure to PM2.5 From Amazon Fires Between 2016 and 2019. *GeoHealth* **4**,.

Nim N, Morris J, Tekasakul P, Dejchanchaiwong R (2023) Fine and ultrafine particle emission factors and new diagnostic ratios of PAHs for peat swamp forest fires. *Environmental Pollution* **335**, 122237.

Normile D (2019) Indonesia's fires are bad, but new measures prevented them from becoming worse. *Science*.

Norris JC, Moore SJ, Hume AS (1986) Synergistic lethality induced by the combination of carbon monoxide and cyanide. *Toxicology* **40**, 121–129.

Ohlemiller TJ (1985) Modeling of smoldering combustion propagation. *Progress in*

Energy and Combustion Science **11**, 277–310.

Page SE, Siegert F, Rieley JO, Boehm HD V., Jayak A, Limink S, Jaya A, Limin S (2002) The amount of carbon released from peat and forest fires in Indonesia during 1997. *Nature* **420**, 61–65.

Palmer KN (1957) Smouldering combustion in dusts and fibrous materials. *Combustion and Flame* **1**, 129–154.

Paton-Walsh C, Smith TEL, Young EL, Griffith DWT, Guérette A (2014) New emission factors for Australian vegetation fires measured using open-path Fourier transform infrared spectroscopy - Part 1: Methods and Australian temperate forest fires. *Atmospheric Chemistry and Physics* **14**, 11313–11333.

Prat-Guitart N, Rein G, Hadden RM, Belcher CM, Yearsley JM (2016a) Propagation probability and spread rates of self-sustained smouldering fires under controlled moisture content and bulk density conditions. *International Journal of Wildland Fire* **25**, 456–465.

Prat-Guitart N, Rein G, Hadden RM, Belcher CM, Yearsley JM (2016b) Effects of spatial heterogeneity in moisture content on the horizontal spread of peat fires. *Science of the Total Environment* **572**, 1422–1430.

Prestemon J, Butry D (2005) Time to Burn: Modeling Wildland Arson as an Autoregressive Crime Function. *American journal of agricultural economics* **87**, 756–770.

Purnomo DMJ, Bonner M, Moafi S, Rein G (2021) Using cellular automata to simulate field-scale flaming and smouldering wildfires in tropical peatlands. *Proceedings of the Combustion Institute* **38**, 5119–5127.

Purnomo DMJ, Apers S, Bechtold M, Sofan P, Rein G (2023) KAPAS II: Simulation of peatland wildfires with daily variations of peat moisture content. *International Journal of Wildland Fire* **32**, 823–835.

Purnomo DMJ, Christensen EG, Fernandez-Anez N, Rein G (2024) BARA: cellular automata simulation of multidimensional smouldering in peat with horizontally varying moisture contents. *International Journal of Wildland Fire* **33**, 1–11.

Qiao Y, Zhang H, Yang J, Chen H, Liu N (2024) Transition from smouldering to flaming combustion of pine needle fuel beds under natural convection. *Proceedings of the Combustion Institute* **40**, 105343.

Qin Y, Musa DNS, Lin S, Huang X (2022a) Deep peat fire persistently smouldering for weeks : a laboratory demonstration. *International Journal of Wildland Fire* **32**, 86–98.

Qin Y, Chen Y, Lin S, Huang X (2022b) Limiting oxygen concentration and supply rate of smoldering propagation. *Combustion and Flame* **245**, 112380.

Qin Y, Zhang Y, Chen Y, Lin S, Huang X (2024) Minimum oxygen supply rate for smouldering propagation : Effect of fuel bulk density and particle size. *Combustion and Flame* **261**, 113292.

Quah E (2002) Transboundary pollution in Southeast Asia: The Indonesian fires. *World Development* **30**, 429–441.

Quintiere J (1997) 'Principles of Fire Behaviour.' (Alar Elken: New York)

Quintiere JG (2016) 'Principles of fire behavior, Second Edition.'

Ramadhan ML, Palamba P, Imran FA, Kosasih EA, Nugroho YS (2017) Experimental study of the effect of water spray on the spread of smoldering in Indonesian peat fires. *Fire Safety Journal* **91**, 671–679.

Rana AK, Guleria S, Gupta VK, Thakur VK (2023) Cellulosic pine needles-based biorefinery for a circular bioeconomy. *Bioresource Technology* **367**, 128255.

Rappold AG, Stone SL, Cascio WE, Neas LM, Kilaru VJ, Carraway MS, Szykman JJ, Ising A, Cleve WE, Meredith JT, et al. (2011) Peat bog wildfire smoke exposure in rural North Carolina is associated with cardiopulmonary emergency department visits assessed through syndromic surveillance. *Environmental Health Perspectives* **119**, 1415–1420.

Rappold AG, Reyes J, Pouliot G, Cascio WE, Diaz-Sanchez D (2017) Community Vulnerability to Health Impacts of Wildland Fire Smoke Exposure. *Environmental Science and Technology* **51**, 6674–6682.

Rashwan TL, Torero JL, Gerhard JI (2021a) Heat losses in a smouldering system: The

key role of non-uniform air flux. *Combustion and Flame* **227**, 309–321.

Rashwan TL, Torero JL, Gerhard JI (2021b) Heat losses in applied smouldering systems: Sensitivity analysis via analytical modelling. *International Journal of Heat and Mass Transfer* **172**, 121150.

Rein G, Cleaver N, Ashton C, Pironi P, Torero JL (2008) The severity of smouldering peat fires and damage to the forest soil. *Catena* **74**, 304–309.

Rein G (2009) Smouldering Combustion Phenomena in Science and Technology. *International Review of Chemical Engineering* **1**, 3–18.

Rein G, Cohen S, Simeoni A (2009) Carbon emissions from smouldering peat in shallow and strong fronts. *Proceedings of the Combustion Institute* **32 II**, 2489–2496.

Rein G (2013) Smouldering Fires and Natural Fuels. 'Fire Phenom. Earth Syst. An Interdiscip. Guid. to Fire Sci.' (Ed Claire M. Belcher) pp. 15–33. (Wiley–Blackwell: London)

Rein G (2016) Smoldering Combustion. 'SFPE Handb. Fire Prot. Eng.' pp. 581–603. (Springer: New York)

Rein G, Cleaver N, Ashton C, Pironi P, Torero JL (2016) Smoldering combustion. 'SFPE Handb. Fire Prot. Eng. Fifth Ed.' pp. 581–603. (Elsevier: New York, NY)

Rein G, Huang X (2021) Smouldering wildfires in peatlands, forests and the arctic: Challenges and perspectives. *Current Opinion in Environmental Science and Health* **24**, 100296.

Reisen F, Brown S, Cheng M (2006) Air toxics in bushfire smoke—Firefighters exposure during prescribed burns. *Forest Ecology and Management* **234**, S144.

Restuccia F, Huang X, Rein G (2017) Self-ignition of natural fuels: Can wildfires of carbon-rich soil start by self-heating? *Fire Safety Journal* **91**, 828–834.

Richter F, Jervis FX, Huang X, Rein G (2021) Effect of oxygen on the burning rate of wood. *Combustion and Flame* **234**, 111591.

Roberts G, Wooster MJ (2021) Global impact of landscape fire emissions on surface level PM2.5 concentrations, air quality exposure and population mortality. *Atmospheric Environment* **252**,.

Robertson KM, Hsieh YP, Bugna GC (2014) Fire environment effects on particulate matter emission factors in southeastern U.S. pine-grasslands. *Atmospheric Environment* **99**, 104–111.

Roulston C, Paton-Walsh C, Smith TEL, Guérette A, Evers S, Yule CM, Rein G, Van der Werf GR (2018) Fine Particle Emissions From Tropical Peat Fires Decrease Rapidly With Time Since Ignition. *Journal of Geophysical Research: Atmospheres* **123**, 5607–5617.

Sahai S, Sharma C, Singh DP, Dixit CK, Singh N, Sharma P, Singh K, Bhatt S, Ghude S, Gupta V, et al. (2007) A study for development of emission factors for trace gases and carbonaceous particulate species from in situ burning of wheat straw in agricultural fields in india. *Atmospheric Environment* **41**, 9173–9186.

Santiago-De La Rosa N, González-Cardoso G, Figueroa-Lara J de J, Gutiérrez-Arzaluz M, Octaviano-Villasana C, Ramírez-Hernández IF, Mugica-Álvarez V (2018) Emission factors of atmospheric and climatic pollutants from crop residues burning. *Journal of the Air and Waste Management Association* **68**, 849–865.

Santoni PA, Bartoli P, Simeoni A, Torero JL (2014) Bulk and particle properties of pine needle fuel beds-influence on combustion. *International Journal of Wildland Fire* **23**, 1076–1086.

Santoso MA, Christensen EG, Yang J, Rein G (2019) Review of the Transition From Smouldering to Flaming Combustion in Wildfires. *Frontiers in Mechanical Engineering* **5**,.

Santoso MA, Cui W, Amin HMF, Christensen EG, Nugroho YS, Rein G (2021) Laboratory study on the suppression of smouldering peat wildfires: effects of flow rate and wetting agent. *International Journal of Wildland Fire* **30**, 378–390.

Santoso MA, Christensen EG, Amin HMF, Palamba P, Hu Y, Purnomo DMJMJ, Cui W, Pamitran AS, Richter F, Smith TEL, et al. (2022) GAMBUT field experiment of peatland wildfires in Sumatra: from ignition to spread and suppression. *International Journal of Wildland Fire* 949–966.

Schmidt M, Lohrer C, Krause U (2003) Self-ignition of dust at reduced volume fractions of ambient oxygen. *Journal of Loss Prevention in the Process Industries* **16**, 141–

147.

Scholten RC, Jandt R, Miller EA, Rogers BM, Veraverbeke S (2021) Overwintering fires in boreal forests. *Nature* **593**, 399–404.

Schug F, Bar-Massada A, Carlson AR, Cox H, Hawbaker TJ, Helmers D, Hostert P, Kaim D, Kasraee NK, Martinuzzi S, et al. (2023) The global wildland–urban interface. *Nature* **621**,.

Shukla K, Aggarwal SG (2022) Particulate Matter Measurement Techniques. 'Handb. Metrol. Appl.' pp. 1–29

Silva CA, Santilli G, Sano EE, Laneve G (2021) Fire occurrences and greenhouse gas emissions from deforestation in the Brazilian Amazon. *Remote Sensing* **13**, 1–18.

Silver B, Arnold SR, Reddington CL, Emmons LK (2024) Large transboundary health impact of Arctic wild fire smoke. *Communications Earth and Environment* **5**,.

Sinclair AL, Graham LLB, Putra EI, Saharjo BH, Applegate G, Grover SP, Cochrane MA (2020) Effects of distance from canal and degradation history on peat bulk density in a degraded tropical peatland. *Science of the Total Environment* **699**,.

Song Z (2022) Modelling oxygen-limited and self-sustained smoldering propagation: Underground coal fires driven by thermal buoyancy. *Combustion and Flame* **245**,.

Song Z, Dang B, Zhang H, Zhao C, Xiao Y, Ren S (2024) Gas-solid oxygen and thermal nonequilibria of reverse smoldering combustion wave. *Proceedings of the Combustion Institute* **40**, 105422.

Song Z, Kuenzer C (2014) Coal fires in China over the last decade: A comprehensive review. *International Journal of Coal Geology* **133**, 72–99.

Stockwell CE, Yokelson RJ, Kreidenweis SM, Robinson AL, Demott PJ, Sullivan RC, Reardon J, Ryan KC, Griffith DWT, Stevens L (2014) Trace gas emissions from combustion of peat, crop residue, domestic biofuels, grasses, and other fuels: Configuration and Fourier transform infrared (FTIR) component of the fourth Fire Lab at Missoula Experiment (FLAME-4). *Atmospheric Chemistry and Physics* **14**, 9727–9754.

Stockwell CE, Jayarathne T, Cochrane MA, Ryan KC, Putra EI, Saharjo BH, Nurhayati

AD, Albar I, Blake DR, Simpson IJ, et al. (2016) Field measurements of trace gases and aerosols emitted by peat fires in Central Kalimantan, Indonesia, during the 2015 El Niño. *Atmospheric Chemistry and Physics* **16**, 11711–11732.

Svensen H, Dysthe DK, Bandlien EH, Sacko S, Coulibaly H, Planke S (2003) Subsurface combustion in Mali: Refutation of the active volcanism hypothesis in West Africa. *Geology* **31**, 581.

Thomas JC, Simeoni A, Gallagher M, Skowronski N (2014) An experimental study evaluating the burning dynamics of pitch pine needle beds using the FPA. *Fire Safety Science* **11**, 1406–1419.

Toledo M, Arriagada A, Ripoll N, Salgansky EA, Mujeebu MA (2023) Hydrogen and syngas production by hybrid filtration combustion: Progress and challenges. *Renewable and Sustainable Energy Reviews* **177**,.

Tomsche L, Piel F, Mikoviny T, Nielsen CJ, Guo H, Campuzano-Jost P, Nault BA, Schueneman MK, Jimenez JL, Halliday H, et al. (2023) Measurement report: Emission factors of NH3 and NHx for wildfires and agricultural fires in the United States. *Atmospheric Chemistry and Physics* **23**, 2331–2343.

Torero JL, Gerhard JI, Martins MF, Zanoni MAB, Rashwan TL, Brown JK (2020) Processes defining smouldering combustion: Integrated review and synthesis. *Progress in Energy and Combustion Science* **81**, 100869.

Turetsky MR, Benscoter B, Page S, Rein G, Van Der Werf GR, Watts A (2015) Global vulnerability of peatlands to fire and carbon loss. *Nature Geoscience* **8**, 11–14.

Urbanski SP (2013) Combustion efficiency and emission factors for wildfire-season fires in mixed conifer forests of the northern Rocky Mountains, US. *Atmospheric Chemistry and Physics* **13**, 7241–7262.

Urbanski SP, Long RW, Halliday H, Lincoln EN, Habel A, Landis MS (2022) Fuel layer specific pollutant emission factors for fire prone forest ecosystems of the western U.S. and Canada. *Atmospheric Environment: X* **16**, 100188.

Valdivieso JP, Rivera J de D (2014) Effect of Wind on Smoldering Combustion Limits of Moist Pine Needle Beds. *Fire Technology* **50**, 1589–1605.

Vicente A, Alves C, Calvo AI, Fernandes AP, Nunes T, Monteiro C, Almeida SM, Pio C (2013) Emission factors and detailed chemical composition of smoke particles from the 2010 wildfire season. *Atmospheric Environment* **71**, 295–303.

Walther DC, Carlos Fernandez-Pello A, Urban DL (1996) Small-scale smoldering combustion experiments in microgravity. *Proceedings of the Combustion Institute* **26**, 1361–1368.

Wang H, van Eyk PJ, Medwell PR, Birzer CH, Tian ZF, Possell M (2017a) Effects of Oxygen Concentration on Radiation-Aided and Self-sustained Smoldering Combustion of Radiata Pine. *ENERGY & FUELS* **31**, 8619–8630.

Wang H, van Eyk PJ, Medwell PR, Birzer CH, Tian ZF, Possell M (2017b) Effects of Oxygen Concentration on Radiation-Aided and Self-sustained Smoldering Combustion of Radiata Pine. *Energy and Fuels* **31**, 8619–8630.

Wang S, Ding P, Lin S, Gong J, Huang X (2021) Smoldering and Flaming of Disc Wood Particles Under External Radiation: Autoignition and Size Effect. *Frontiers in Mechanical Engineering* **7**, 1–11.

Wang S, Lin S, Liu Y, Huang X, Gollner MJ (2022a) Smoldering ignition using a concentrated solar irradiation spot. *Fire Safety Journal* **129**,.

Wang Z, Zhang T, Huang X (2022b) Predicting real-time fire heat release rate by flame images and deep learning. *Proceedings of the Combustion Institute* **000**, 1–9.

Ward DE, Radke LF (1993) Emissions measurements from vegetation fires: A comparative evaluation of methods and results. *Fire in the Environment: The Ecological, Atmospheric, and Climatic Importance of Vegetation Fires* 53–65.

Watson JG, Cao J, Chen LWA, Wang Q, Tian J, Wang X, Gronstal S, Sai Hang Ho S, Watts AC, Chow JC (2019) Gaseous, PM2.5 mass, and speciated emission factors from laboratory chamber peat combustion. *Atmospheric Chemistry and Physics* **19**, 14173–14193.

Watson AJ, Lovelock JE (2013) The dependence of flame spread and probability of ignition on atmospheric oxygen: an experimental investigation. *Fire phenomena and the Earth system: an interdisciplinary guide to fire science* 273–287.

Webb EE, Loranty MM, Lichstein JW (2021) Surface water, vegetation, and fire as drivers of the terrestrial Arctic-boreal albedo feedback. *Environmental Research Letters* **16**,.

WHO (2021) WHO global air quality guidelines.

Wiedinmyer C, Kimura Y, Mcdonald-Buller EC, Emmons LK, Buchholz RR, Tang W, Seto K, Joseph MB, Barsanti KC, Carlton AG, et al. (2023) The Fire Inventory from NCAR version 2.5: an updated global fire emissions model for climate and chemistry applications. *Geoscientific Model Development* **16**, 3873–3891.

Witze A (2020) The Arctic is burning like never before — and that's bad news for climate change. *Nature* **585**, 336–337.

Wolfram S (1983) Statistical mechanics of cellular automata. *Reviews of modern physics* **55**, 601.

Wooster MJ, Roberts G, Perry GLW, Kaufman YJ (2005) Retrieval of biomass combustion rates and totals from fire radiative power observations: FRP derivation and calibration relationships between biomass consumption and fire radiative energy release. *Journal of Geophysical Research Atmospheres* **110**, 1–24.

Wu C, Huang X, Wang S, Zhu F, Yin Y (2020) Opposed Flame Spread over Cylindrical PMMA Under Oxygen-Enriched Microgravity Environment. *Fire Technology* **56**, 71–89.

Wu W, Yao M, Yang X, Hopke PK, Choi H, Qiao X, Zhao X, Zhang J (2021) Mortality burden attributable to long-term ambient PM2.5 exposure in China: using novel exposure-response functions with multiple exposure windows. *Atmospheric Environment* **246**, 118098.

Wu M, Luo J, Huang T, Lian L, Chen T, Song S, Wang Z, Ma S, Xie C, Zhao Y, et al. (2022) Effects of African BaP emission from wildfire biomass burning on regional and global environment and human health. *Environment International* **162**, 107162.

Xu L, Saatchi SS, Yang Y, Yu Y, Pongratz J, Anthony Bloom A, Bowman K, Worden J, Liu J, Yin Y, et al. (2021) Changes in global terrestrial live biomass over the 21st century. *Science Advances* **7**,.

Xu W, Scholten RC, Hessilt TD, Liu Y, Veraverbeke S (2022) Overwintering fires rising in eastern Siberia. *Environmental Research Letters* **17**,.

Xu R, Ye T, Yue X, Yang Z, Yu W, Zhang Y, Bell ML, Morawska L, Yu P, Zhang Y, et al. (2023) Global population exposure to landscape fire air pollution from 2000 to 2019. *Nature* **621**, 521–529.

Yamazaki T, Matsuoka T, Nakamura Y (2019) Near-extinction behavior of smoldering combustion under highly vacuumed environment. *Proceedings of the Combustion Institute* **37**, 4083–4090.

Yamazaki T, Matsuoka T, Li Y, Nakamura Y (2020) Applicability of a Low-Pressure Environment to Investigate Smoldering Behavior Under Microgravity. *Fire Technology*.

Yan H, Fujita O (2019) Experimental investigation on the smoldering limit of scraps of paper initiated by a cylindrical rod heater. *Proceedings of the Combustion Institute* **37**, 4099–4106.

Yang J, Liu N, Chen H, Gao W, Tu R (2019) Effects of atmospheric oxygen on horizontal peat smoldering fires: Experimental and numerical study. *Proceedings of the Combustion Institute* **37**, 4063–4071.

Yang J, Rein G, Chen H, Zammarano M (2020) Smoldering propensity in upholstered furniture: Effects of mock-up configuration and foam thickness. *Applied Thermal Engineering* **181**, 115873.

Yang J, Wang H, Wang R, Fu Z, Hu Y (2024a) Experimental study of smouldering combustion and transient emissions from forest duff with dual layers. *Proceedings of the Combustion Institute* **40**, 105354.

Yang J, Wang H, Wang R, Xu J, Huang W, Hu Y (2024b) Experimental and theoretical study on the smoldering combustion of size-fractioned forest duff particles. *International Journal of Heat and Mass Transfer* **231**, 125883.

Yang J, Chen H (2018) Natural Downward Smouldering of Peat : Effects of Inorganic Content and Piled Bed. *Fire Technology*.

Yermán L, Wall H, Torero J, Gerhard JI, Cheng YL (2016) Smoldering Combustion as a

Treatment Technology for Feces: Sensitivity to Key Parameters. *Combustion Science and Technology* **188**, 968–981.

Yermán L, Wall H, Torero JL (2017) Experimental investigation on the destruction rates of organic waste with high moisture content by means of self-sustained smoldering combustion. *Proceedings of the Combustion Institute* **36**, 4419–4426.

Yokelson RJ (1999) Emissions of formaldehyde, acetic acid, methanol, and other trace gases from biomass fires in North Carolina measured by airborne Fourier transform infrared spectroscopy. *Journal of Geophysical Research Atmospheres* **104**, 30109–30125.

Yokelson RJ, Bertschi IT, Christian TJ, Hobbs P V., Ward DE, Hao WM (2003) Trace gas measurements in nascent, aged, and cloud-processed smoke from African savanna fires by airborne Fourier transform infrared spectroscopy (AFTIR). *Journal of Geophysical Research: Atmospheres* **108**,.

Yokelson RJ, Karl T, Artaxo P, Blake DR, Christian TJ, Griffith DWT, Guenther A, Hao WM (2007) The tropical forest and fire emissions experiment: Overview and airborne fire emission factor measurements. *Atmospheric Chemistry and Physics* **7**, 5175–5196.

Yokelson RJ, Burling IR, Urbanski SP, Atlas EL, Adachi K, Buseck PR, Wiedinmyer C, Akagi SK, Toohey DW, Wold CE (2011) Trace gas and particle emissions from open biomass burning in Mexico. *Atmospheric Chemistry and Physics* **11**, 6787–6808.

Yokelson RJ, Burling IR, Gilman JB, Warneke C, Stockwell CE, De Gouw J, Akagi SK, Urbanski SP, Veres P, Roberts JM, et al. (2013) Coupling field and laboratory measurements to estimate the emission factors of identified and unidentified trace gases for prescribed fires. *Atmospheric Chemistry and Physics* **13**, 89–116.

Yuan H, Restuccia F, Richter F, Rein G (2019) A computational model to simulate self-heating ignition across scales, configurations, and coal origins. *Fuel* **236**, 1100–1109.

Zhang T, Wooster MJ, Green DC, Main B (2014) New field-based agricultural biomass burning trace gas, PM2.5, and black carbon emission ratios and factors measured in situ at crop residue fires in Eastern China. *Atmospheric Environment* **121**, 22–34.

Zhang H, Qiao Y, Chen H, Liu N, Zhang L, Xie X (2020) Experimental study on flaming ignition of pine needles by simulated lightning discharge. *Fire Safety Journal* 103029.

Zhang W, Song Q, Wang X, Wang X, Li H, Yang Z (2023) Experimental study and modeling analysis of sewage sludge smoldering combustion at different airflow rates. *Waste Management* **168**, 126–136.

Zhang Y, Shu Y, Qin Y, Chen Y, Huang X, Zhou M (2024) Resurfacing of Underground Peat Fire: Smoldering Transition to Flaming Wildfire on Litter Surface. *International Journal of Wildland Fire* **33**, 1–10.

Zheng GJ, Duan FK, Su H, Ma YL, Cheng Y, Zheng B, Zhang Q, Huang T, Kimoto T, Chang D, et al. (2015) Exploring the severe winter haze in Beijing: The impact of synoptic weather, regional transport and heterogeneous reactions. *Atmospheric Chemistry and Physics* **15**, 2969–2983.

Zhou B, Yang S, Jiang X, Cai J, Xu Q, Song W, Zhou Q (2021) The reaction of free radicals and functional groups during coal oxidation at low temperature under different oxygen concentrations. *Process Safety and Environmental Protection* **150**, 148–156.

Zou J, Han Y, So S-S (2009) Overview of artificial neural networks. *Artificial neural networks: methods and applications* 14–22.